# Formation and stability of lithium protective layer for corrosion protection of AA2024-T3 and AA2198-T8 aluminum alloys


**DELFT UNIVERSITY OF TECHNOLOGY**


MASTER THESIS REPORT

(MS53000)


*Author: Chongchong Chen (student number: 4749294)*

*Supervisor: Dr. Y. (Yaiza) Gonzalez Garcia*

*Co-Supervisor: Dr. Emmanouela Michailidou*

Faculty of Mechanical, Maritime and Materials Engineering

Materials Science and Engineering


March 30, 2020

# Abstract

As a possible replacement for chromate-based coatings in the aerospace industry, lithium leaching coatings have been widely studied in recent years. The formation mechanism of protective layer on AA2024-T3 aluminum alloys has been investigated intensively. In order to explore more possibilities for its application in aerospace industry, AA2198-T8 aluminum alloys is also be considered in research for its unique chemical composition which contains lithium.

In this thesis, three kinds of different polymer coatings which are non-inhibiting coating, coating containing $Li_2CO_3$ and proprietary industrial $Li_2CO_3$-loaded coating XP420 are used. These three polymer coatings were applied on the AA2024-T3 and AA2198-T8 aluminum alloys samples. A defect was artificially made on the these samples. Then the samples were divided into two groups, one group is used directly for the experiment to investigate the formation of protective layer, one week neutral salt spray test were applied to another group in order to form the protective layer in advance and later used for the experiment. The second group is mainly focus on investigating the stability of protective layer. What is more, low volume of electrolyte was used during experiment considering the real environment of coating's application.

The research results showed that: (1) Under low volume electrolyte of 5ml aqueous 0.1M NaCl solution, the protective layer is successfully formed; (2) $Li_2CO_3$-loaded coating shows better corrosion inhibition performance compared to the non-inhibiting coating; (3) AA2198-T8 aluminum alloy containing lithium in its element composition further contributes to the formation of protective layer; (4) In general, proprietary industrial $Li_2CO_3$-loaded coating XP420 are more stable when exposed to the corrosion condition.

# Contents

# List of Figures

# List of Tables

# 1 Introduction

Aluminium is widely used in various industries. By adding different alloys to alter their microstructure and composition, desired properties can be obtained for specific applications. The combination of acceptable cost, light weight, appropriate mechanical, chemical, and physical properties, structural integrity, and manufacturability improves the development of applications from commodity fabrication to aircraft manufacturing [1]. Many aluminium alloys can be used satisfactorily in their conventional form under environmental/atmospheric conditions, thus enabling the corrosion protection industry to focus on more demanding area that requires better coating systems to resist corrosion, such as in aerospace industry [2].

## 1.1 Corrosion of aluminium and its alloys in aqueous environment

It is acknowledgeable aluminium and its alloys are resistant to moderately corrosive aqueous environments. The protective oxide layer represents the thermodynamic stability of the aluminium alloy in a corrosive environment. It is both a physical barrier when damaged in oxidizing environment. Due to the complexity of the process, the mechanism of chloride ion damage to the passivation layer is still under debate [3, 4]. The general consensus is that local attacks begin with the adsorption of aggressive anions and form soluble transition complexes with cations on the oxide surface [5]. The corresponding Pourbaix diagram summarizes the thermodynamic principles that predict the corrosion behaviour of aluminium as shown in Figure 1. This has led to a potential and pH value based on the electrochemical reaction of the species involved [6].

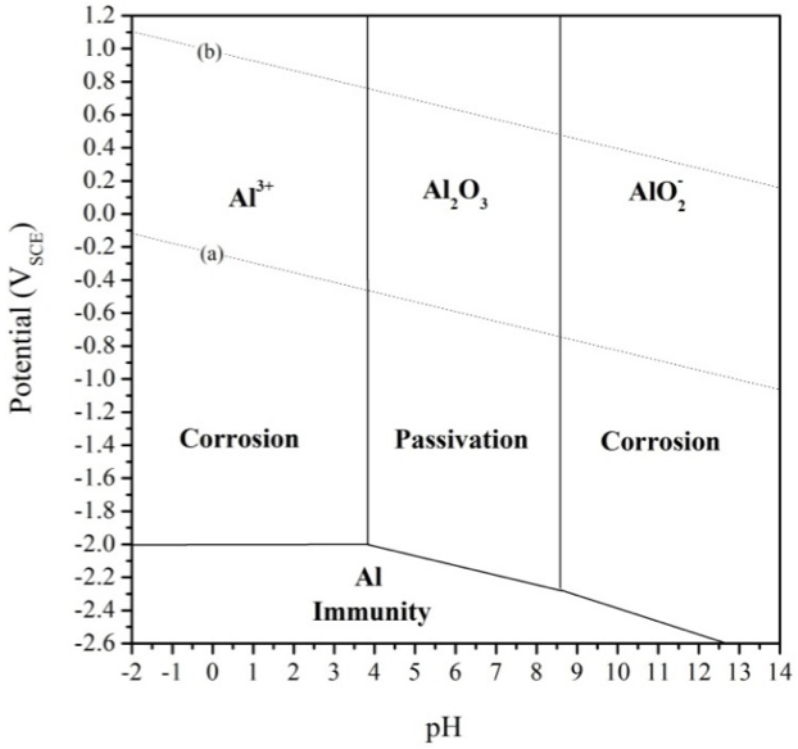


Figure 1: E-pH diagram for pure Al at 25 °C in aqueous solution. The lines (a) and (b) correspond to water stability and its decomposed product [6]

## 1.2 Corrosion and coatings in aerospace industry

Corrosion is a complex process starting from the nano scale , and its manifestation can be clearly shown at the macroscopic level, which is one of the main cause of material failure under severe environmental conditions. Corrosion compromises the performance of aircraft structures carrying passengers and cargo [7]. Failure due to corrosion will cause catastrophic consequences such as aircraft unavailability, safety and economic cost of aircraft maintenance. The understanding of aerospace corrosion should take into account the various confounding variables that can lead to corrosion initiation and propagation [8].

In the initial design of the aircraft, requirements such as weight, aerodynamics, fuel efficiency, and other specifications were determined [8]. Unfortunately, not all requirements are achievable and can affect aircraft design and production. Historically, the anti-corrosion design of aircraft experienced many discussions, overturns and revisions [9]. Different alloying elements, dissimilar metals, lack of drainage channels etc. may lead to various types of corrosion, such as pitting corrosion, intracrystalline corrosion, galvanic corrosion, filiform corrosion, crevice corrosion, environment-assisted corrosion, fretting fatigue, etc [10].

As it mentioned before, corrosion can compromise the design safety factor built into the ultimate bearing capacity of the structure. However, changes in material physical properties, aircraft manufacturing, flight conditions, and emergencies need to reserve a safety factor for the aircraft. Nevertheless, corrosion can affect the load-bearing capacity of a structure in a number of ways [8]. First, it reduces the cross-sectional area of the structure, thereby creating a scene in which less material must bear more load per area. Second, corrosion, especially pitting corrosion, can become a place where cracks occur. This is particularly disturbing if multiple small corrosion-induced cracks are connected to create a long crack. Finally, the repair of corroded structures usually requires the removal of corroded materials and some surrounding structures. If the corrosion is mild or moderate, sufficient structure can still safely carry its load. Eventually, the continuous repair and removal of corrosive materials will exceed the allowable repair limit and the structure will need to be replaced. Therefore, a complete corrosion control program is required, which makes efficient and environmentally sustainable operation of coatings and surface treatments one of the key factors to ensure the long-term protection of aircraft structures [11].

### 1.2.1 Corrosion control scheme in aerospace industry

The aerospace industry has high requirements on the coatings used for painting or repainting existing aircraft fleets. Several layers of coating are necessary for every vehicle which can provide better adhesion and protection against a corrosive environment, visual aesthetic and structural integrity. A typical coating system consists of three separate coating layers. The main function of this corrosion protection scheme is to act as a barrier (passive protection) between the alloy and the aggressive environment. The first layer is a conversion coating, which is the product of substrate pre-treatment. The conversion layer is usually a very thin inorganic layer (< 10-60 nm) that provides corrosion protection and improves adhesion between the substrate and the primer, the second coat of the coating system. The primer has a similar function to the conversion paint but is composed of a tinted organic resin matrix. The application's primer thickness is also from 5 to 200 $\mu$m although the thickness of 25 $\mu$m is usually due to the aircraft weight limit. Primers are the main anticorrosive material [12]. Typical formulations include chromate and non-chromate pigments embedded in epoxy. Finally, a topcoat acts as a primary barrier against environmental impacts such as extreme weather and ultraviolet light, and provides decoration and camouflage for the aircraft [13]. A typical topcoat is made from polyurethane resin and the film thickness varies from 50 to 200 pm. The complete coating system, as shown in Figure 2, consists of the pre-treatment/primer/topcoat.

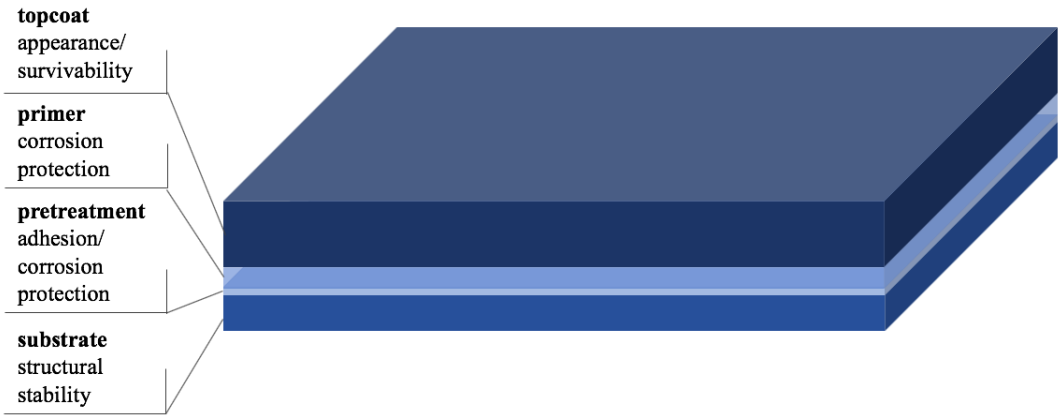


Figure 2: Schematic of components that make up an aircraft coating system

### 1.2.2 Active corrosion protection and the use of chromate in coating

Nowadays, corrosion protection scheme also requires the ability to provide active corrosion protection by releasing inhibitors (leaching mechanisms) in case the barrier is destroyed [14]. Today, this leaching mechanism has become a key element of the active corrosion protection mechanism of the "state of the art" corrosion protection scheme. This means that when the corrosion protection scheme is damaged and the substrate is exposed to the environment, the inhibitor leaches from the coating as moisture enters (Figure 3) and is transported to exposed or damaged areas, forming a new barrier layer and protecting the alloy from impact of environment and corrosion [11].

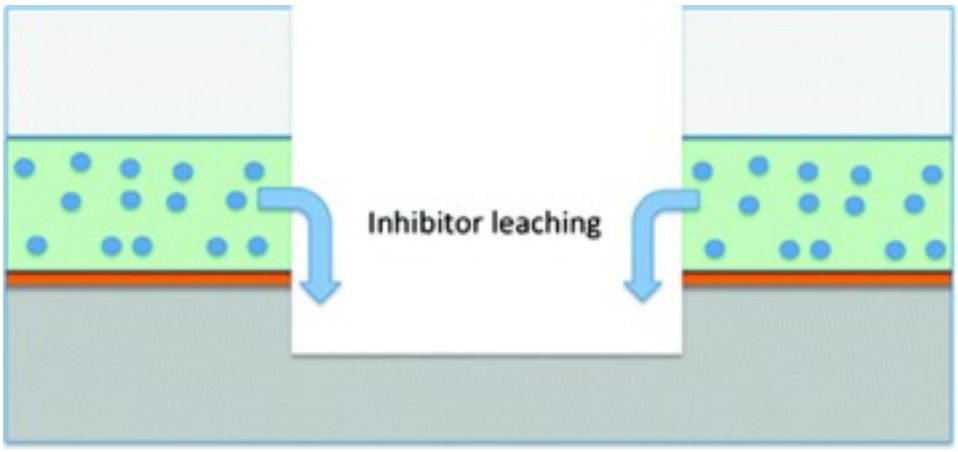


Figure 3: Inhibitor leaching from the coating as active corrosion inhibition mechanism [11]

Current aerospace coating systems are mainly based on a pre-treatment (e.g. chemical conversion coating or anodising) on the aluminium alloy [11]. Hexavalent chromium-based

coatings have excellent versatility, as well as excellent corrosion resistance and cost effectiveness. The excellent corrosion resistance of chromate can be continuously used in a very large range of pH value and electrolyte concentration range. So far, no other inhibitory compound can match this feature, most of them have limited working pH and minimum concentration requirements [15, 16, 17]. Although the corrosion inhibition mechanism of chromate was known for decades, it was not really understood until modern times. Unlike most inhibitors, chromates are both anodic and cathodic inhibitors, which means that they can limit the rate of metal dissolution while reducing the rate of reduction reactions (including oxygen reduction and water reduction) in many environments(Figure 4). The figure 4 shows the cathodic and anodic inhibition of chromates on different materials under three types of environments. All of them in both anodic and cathodic branches were significantly inhibited and the dominant effect on the electrochemical kinetics can clearly be seen by a well defined passive region [18, 19, 20, 21].

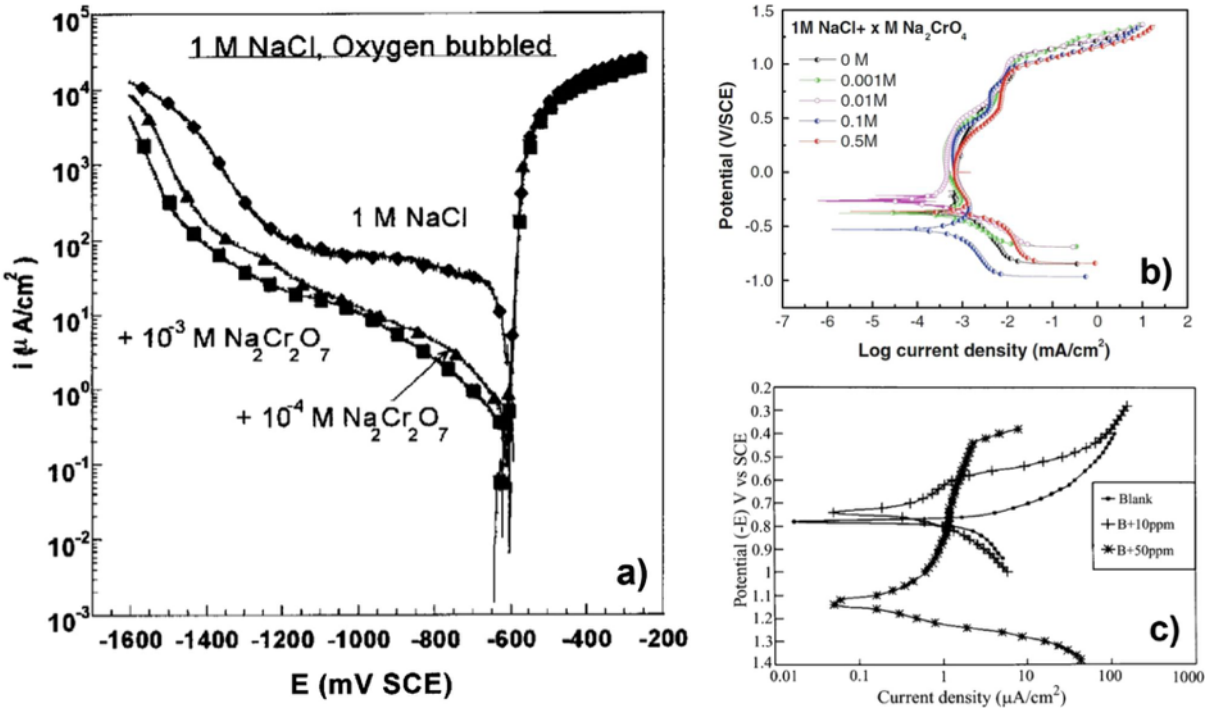


Figure 4: Compilation of several polarisation tests illustrating the cathodic and anodic inhibition of chromates on: (a) AA2024-T3 in 1M NaCl exposed to $10^{-3}$M and $10^{-4}$ M $Na_2Cr_2O_7$ [18] (b) 2205 duplex stainless steel in 1M NaCl and $Na_2CrO_4$ varying from 0 to 0.5M and finally [22] (c) Zinc in acid rain solution exposed to 0,10,and 50ppm of $SrCrO_4$ [23]

At various pH conditions, chromate can act as an effective corrosion inhibitor, which also means that chromate has been widely and successfully used in anticorrosive primers and coatings. Figure 5 shows how Cr(VI) compounds behave under different inhibition scenarios. chromate ions ($CrO_4^{2-}$) penetrate into the electrolyte (and reach the so-called "active site") and undergo cathodic reduction (in combination with dissolution of the anode metal),

then a protective chromium oxide ($Cr_2O_3$) film is formed (Figure 5). Due to its relative insolubility in water environments across the ambient pH spectrum and its adherence to the underlying metal, $Cr_2O_3$ film can act as a barrier to corrosion [24, 25]. When a leaching mechanism is introduced as shown in Figure 5b and c, the leaching inhibitor $CrO_4^{2-}$ is released, and migrates through condensed moisture on the surface and reacting with actively corroding sites, thereby healing defects in the coating [26].

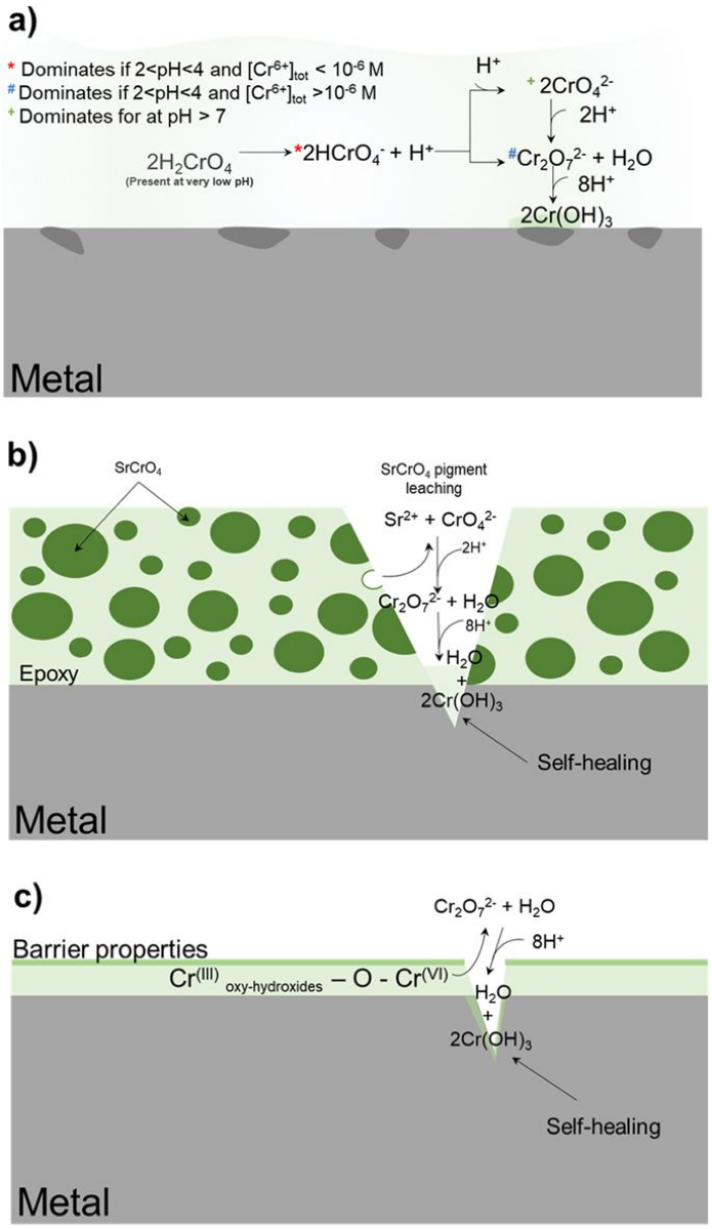


Figure 5: Schematic illustrations of the different inhibition scenarios associated with Cr(VI) compounds in: (a) aqueous solution, or when a morphological defect occurs; (b) in the presence of a Sr-Cr-based primer, or (c) a Cr(VI) conversion coating, with a particular emphasis on the self-healing and barrier properties [24, 25]

### 1.2.3 Development towards chromate-free corrosion protection

Though the performance of hexavalent chromium is promising, the harmful effects of hexavalent chromium on the environment and human health motivate the need to reconsider most current industrial corrosion protection measures [27]. Hexavalent chromium is now known to cause irreversible health damage. In addition, due to poor waste management and disposal maintenance, chromate can also cause genotoxicity to aquatic plants through soil and water pollution. Consequently, chromium compound usage is now restricted unless granted exclusive authorization from the European Chemical Agency (ECHA) [28]. However, most evaluated alternatives often do not perform as well as hexavalent chromium, or they require chromated chemical conversion coatings, wash primers, or anodising to support [11]. The problem has not yet been solved completely, but gratifying progress has already been made during the development of chromate free coatings, and chromate free coating systems are being introduced to the market such as the technologies shown in Table 1. With this achievement, the industry will be able to focus on eliminating hexavalent chromium from aircraft structures.

| **Coating system** | **Substrate** | **Characteristics** | **Viability** |
|---|---|---|---|
| **Rare-earth-based coatings** | AA2024-T3 | Mainly works as cathodic inhibitors, precipitation of Ce oxide on cathodic sites, induced by the local pH increase | Vulnerability of RE market as mainly dominated by Chinese production |
| | Galvanized steel | | Only minor improvement in pitting potential and corrosion current was noted |
| **Organic (including epoxy, sol–gel, polyurethane, silane and nanocomposites)** | Al alloys galvanized steel | Good barrier properties provided by both systems | Organic: effective inhibitor is still needed to achieve good corrosion resistance |
| | | Nanocomposites: higher density of inhibitor can be,loaded into the system | Nanocomposites: cost towards implementation could be too important |
| **Phosphate-based** | Steel carbon steel Al alloys zinc | Good barrier properties provided by the precipitation of metal-phosphate compounds | pH stability of phosphate-based coatings inferior to chromium oxide |
| | | | No self-healing properties |
| **Mg-rich primers** | AA2024-T3 | Act as sacrificial anode and maintain the substrate below its pitting potential | Additional topcoat is needed to ensure durability of the coating |
| | | | Cannot be used on Mg alloys or galvanized steel |

Table 1: The most promising technologies and their associated corrosion protection mechanisms [27]

## 1.3 Introduction of Lithium containing coating technology

Except alternatives mentioned in the last section, recently, lithium containing coating has been studied extensively due to its potential as an ideal replacement for chromate in organic coating. Originally, lithium was introduced on the purpose of weight reduction in the context of Al alloys [29]. However, more and more studies have reported the inhibition effect of lithium when exposed to aluminium, especially in alkaline environments. The results show that lithium can be intercalated into the aluminium hydroxide matrix, thereby stabilizing the passive film in a corrosive environment. On the other hand, Buchheit et al, reported that Al-Li layered double hydroxide (LDH) is formed during the anodic dissolution of Al-Cu-Li-containing alloys [30]. The composition of these natural mixed metal oxides is as follows: MII(1−x)MIII(x)(OH)2[An-]x/n, and consist of a positively charged brucite layer and water-anion layers which electrostatically bound to each other [31]. Based on this observation, the lithium based conversion coatings for aluminium alloys was emerged and further discussed by scientists.

### 1.3.1 The discovery of a protective layer

It was found that lithium salts can be used as leaching inhibitor for coatings to protect aluminium alloys. Organic coating containing lithium salts demonstrates the corrosion protection in an artificial damage when exposed to neutral salt spray conditions (ASTM B-117). lithium ions leach from the coating matrix and generate a protective layer in the scribed area [32]. The scanning electron microscope (SEM) images shown in Figure 6 illustrate the details of this protective layer. It can be seen that the protective layer consists of barrier, porous and columnar morphologies, and the main element in this layer are aluminium, oxygen and lithium as shown in Figure 7 [33]. In addition, the outer columnar region can be correlated with the surface as observed with a planar view SEM image (Figure 8). Fine textures were observed on the overall surface at increased magnification (Figure 8c and d).

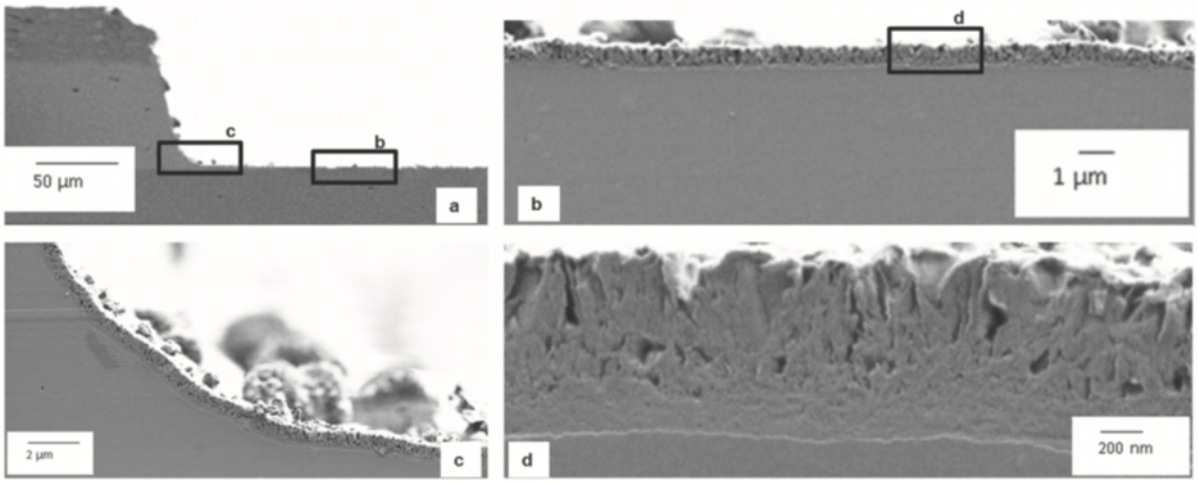


Figure 6: SEM cross-cut images of protective layers generated from a Li-carbonate loaded coating after 168 h ASTM B-117 exposure (a) scribed area, (b) middle section of the scribe, (c) curved area of bottom of the scribe, (d) detailed morphology of layer (middle section of the scribe) [33]

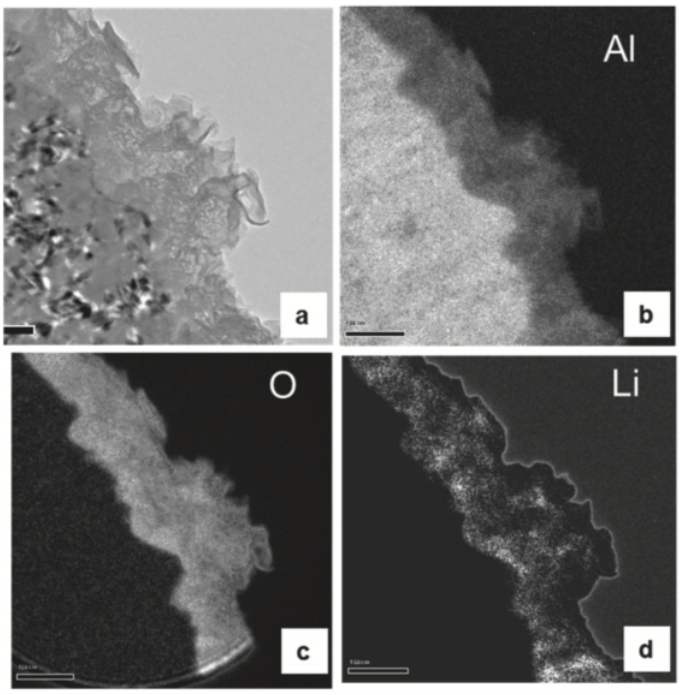


Figure 7: TEM image and TEM-EELS elemental mapping of the layer generated from the Li-carbonate loaded coating (a) TEM image, (b) aluminium, (c) oxygen, and (d) lithium distribution [33]

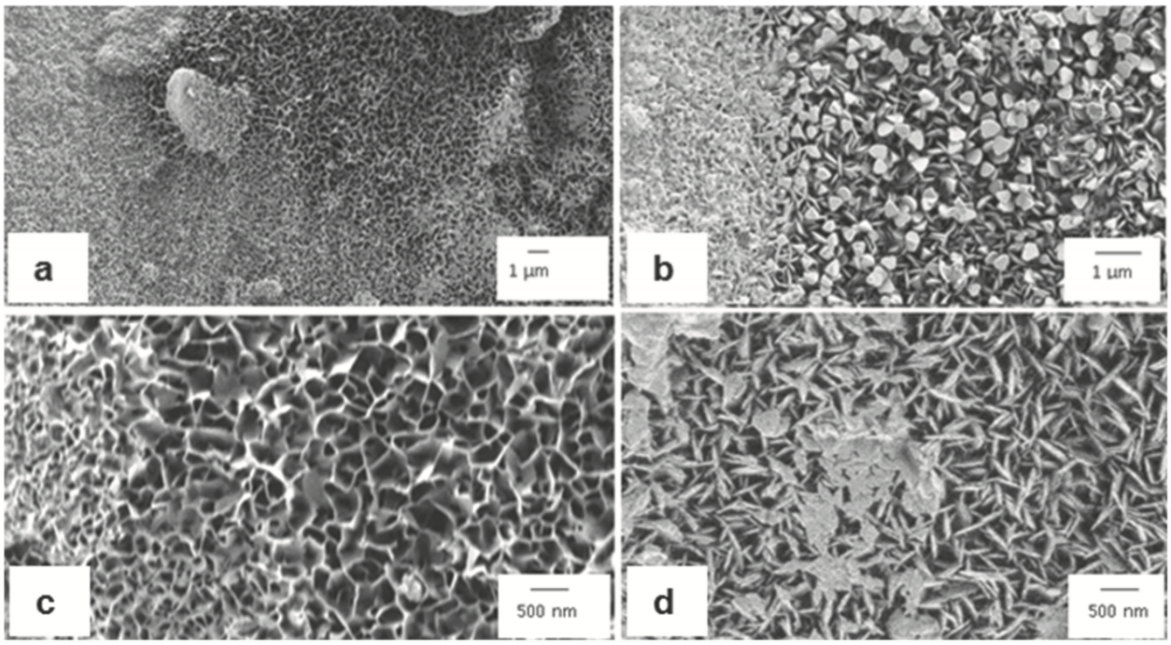


Figure 8: Top view appearance of protective layer with increasing magnification after 168 h ASTM B-117 exposure. (a), (c) Li-carbonate and (b), (d) Li-oxalate [33]

Both Li-carbonate and Li-oxalate pigmented primers exhibit this special structure. The texture is not uniform as shown in Figure 8. In some areas the texture is more pronounced, while in other areas the surface is still relatively flat. The texture consists of fine flakes, some of which are oriented almost perpendicular to the surface (Figure 8d), while others are randomly oriented. It is not clear that this different topographical morphology or texture is due to negative ions or different lithium ion concentrations which is resulted from the higher solubility of Li-oxalate [33].

### 1.3.2 Mechanism of protective layer formation

The formation of a protective layer in a coating defect from lithium-leaching organic coating can be shown in Figure 9, which can be described in four stages. The first stage begins with exposure, leaching and oxide thinning (stage I). This is the stage where the damaged area is first exposed to a corrosive chloride environment. When the aqueous electrolyte is present in the damaged area, the lithium salt begins to leach from the coating matrix. As a result of this leaching phenomenon, the alkalinity is increased to a value of around pH 9 to 10 [34].

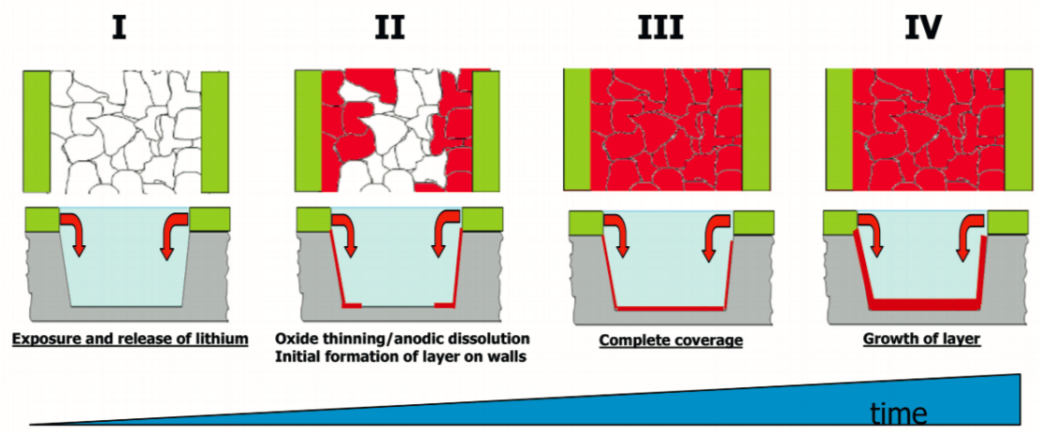


Figure 9: Schematic illustration of the four stages during the formation of the protective later in the damaged area as a function of time [34]

The natural oxide layer formed on the surface of aluminium becomes thinner due to the presence of chlorides and alkaline medium. The second stage is the initial formation stage of the protective layer (stage II). Then anodic dissolution will begin, leading to the formation of the aluminium hydroxide gel under moderately alkaline condition [35]. The initial growth of the aluminium hydroxide gel occurs at the walls and sides of scratched area and gradually progressing to the center of the base metal. Because of chemical and electrochemical differences between different grains(due to the energy stored by the grains), the anodic dissolution and formation of protective layers at some specific grains seems to grow faster [36, 37]. The third stage represents the lateral coverage of the damaged area (stage III), and lately the fourth stage can be identified to represent the increase in the direction of the thickness of the protective layer (stage IV). The stage II and III represent the growth and dissolution processes respectively [33]. It is generally observed that this growth and dissolution process continues during stage IV until the formation of a stable state layer is complete.

## 1.4 Objectives of this project

The formation mechanism of the protective layer has been extensively studied. Therefore, in addition to learning and understanding the theory behind it, it is important to prove whether the results of lithium-containing coatings applied on different types of aluminium alloys are consistent. Two coated aluminium alloys were studied: the conventional AA2024-T3 and the new generation Lithium-aluminium alloys AA2198-T8. The major difference between the materials used in this two systems are the existence of lithium. The addition of Lithium in aluminium alloys is an obvious contender in various means of transportation due to its advantages of reducing alloy density and high strength. The continuously research in

how alloy composition, microstructure, and thermomechanical processing influence the mechanical and corrosion properties has improved. This helps the industry to make appropriate choices of alloy chemistry, thermomechanical processing, and multistep ageing practices that have resulted in third-generation Al–Li alloys suitable for more extensive usage in the aerospace and space industries [38][39].

For this two systems of aluminium alloys, each type of them has two groups. One group is used as reference without any pre-treatment, the other group of samples would be immersed in the neutral salt spray test (NSS) for 168 hours to form the protective layer in advance. Three different coating layers were investigated in this thesis for each group: a clear model coating without lithium salts, a model coating containing lithium salts and a commercial coating XP420.

Electrochemical techniques, including open circuit potential (OCP), linear resistance polarisation (LPR) measurement and electrochemical impedance spectroscopy (EIS) analysis, are used to understand the mechanisms and effects of inhibition. Also, in order to compare the layer formation before and after the experiment more precisely, the scanning electron microscope (SEM) was used to obtain the surface and cross-section of protective layers in the defect of the different coating systems.

# 2 Experiments

In this research, it is important to control the volume and concentration of electrolyte to make it similar to the environmental condition which attribute to the atmospheric corrosion. The electrochemical response of protective layers formed in a defect from lithium-leaching organic coating under 5ml 0.1M NaCl electrolyte are evaluated. ALSO, techniques and materials used during the experiments are introduced, and process of experiments are summarised.

## 2.1 Experiment materials

Commercial AA2024-T3 and AA2198-T8 aluminum alloys were provided by AkzoNobel and their composition are shown respectively on Table 2 and Table 3. All the chmicals used were of analytical grade and provided by the Sigma-Aldrich Chemical Company.

As discussed in chapter of Introduction, lithium is very important during the layer formation. Therefore, it is significant to study whether the existence of lithium in aluminum alloys would affect the inhibition effect of coating. Therefore, the entire experiments are divided into two systems, which are AA2024-T3 and AA2198-T8 aluminium alloys. These two systems have two groups of samples respectively. Each group contains three types of organic coatings which are non-inhibiting model coating, $Li_2CO_3$-loaded model coating and proprietary industrial $Li_2CO_3$-loaded coating XP420. The list of samples performed in experiments were shown in Table 4. The neutral salt spray test (ASTM B-117) which provides the protective layer in advance were performed for 168h for samples in Group 2 and Group 4 for the aim of observing the performance during the acceleration test. The $Li_2CO_3$-loaded model coating contains the total pigment volume concentration (PVC) of 30% and 15% PVC of them are loaded with Lithium salts. The composition of the $Li_2CO_3$-loaded model coating is listed in the Table 5. The surface of different groups of samples were damaged by different tools but result in the same two intersecting scribes with a length of 2cm, width 1mm. The summary of parameters of these samples is given in Table 6.

| Chemical Composition (%) | | | | | | | | | |
|---|---|---|---|---|---|---|---|---|---|
| Si | Fe | Cu | Mn | Mg | Cr | Ti | Zn | Others | Al |
| 0.5 | 0.5 | 3.8-4.9 | 0.3-0.9 | 1.2-1.8 | 0.1 | 0.15 | 0.25 | 0.15 | rest |

Table 2: Chemical composition of commercial AA2024-T3 aluminum alloy [33]

| Chemical Composition (%) | | | | | | | | | | | | |
|---|---|---|---|---|---|---|---|---|---|---|---|---|
| Si | Fe | Cu | Mn | Mg | Cr | Ni | Zn | Ti | Zr | Ag | Li | Al |
| 0.02 | 0.04 | 3.4 | 83* | 0.32 | 10* | 30* | 86* | 0.03 | 0.11 | 0.26 | 1.0 | rest |
| Others: Each: 0.05% max. Total: 0.15% max, *ppm | | | | | | | | | | | | |

Table 3: Chemical composition of commercial AA2198-T8 aluminum alloy

| **System AA2024-T3** | | **System AA2198-T8** | | **Description** |
|---|---|---|---|---|
| **Group 1** | **Group 2** | **Group 3** | **Group 4** | |
| Model coating | Model coating_1-week NSS | Model coating | Model coating_1-week NSS | Non-inhibiting reference coating |
| Model coating containing $Li_2CO_3$ | Model coating containing $Li_2CO_3$_1-week NSS | Model coating containing $Li_2CO_3$ | Model coating containing $Li_2CO_3$_1-week NSS | $Li_2CO_3$-loaded coating |
| XP420 | XP420_1-week NSS | XP420 | XP420_1-week NSS | Proprietary industrial $Li_2CO_3$-loaded coating |

Table 4: Categories of Samples used for System AA2024-T3 & AA2198-T8

| **Leachable inhibitor** | | $Li_2CO_3$ |
|---|---|---|
| **Loading (PVC%)** | | 15% |
| **Component A** | | |
| N-Butylacetate | Sigma Aldrich | 85.0 g |
| Desmophen 650MPA | Covestro | 47.7 g |
| $Li_2CO_3$ | Sigma Aldrich | 23.6 g |
| Magnesium oxide | Sigma Aldrich | 16.4 g |
| Tioxide TR 92 | Huntsman | 5.2 g |
| Blanc Fixe N ($Ba(SO_4)$) | Sachtleben | 15.4 g |
| **Component B** | | |
| Tolonate HDB 75 MX | Vencorex | 28.5 g |
| Dynasilan Glymo | Evonik | 5.2 g |

Table 5: Composition of $Li_2CO_3$-loaded organic model coating [34]

| | AA2024-T3 | | AA2198-T8 | |
|---|---|---|---|---|
| | Group 1 | Group 2 | Group 3 | Group 4 |
| Length × Width (cm) | 5x5 | 10x10 | 5x5 | 10x10 |
| Thickness (mm) | 1 | 2 | 1 | 2 |
| Artificial defect caused by | Manually by a cutting tool | Mechanical milling device | Manually by a cutting tool | Mechanical milling device |
| Neutral Salt Spray test for 168h | No | Yes | No | Yes |

Table 6: Parameters of Samples applied for Systems AA2024-T3 and AA2198-T8

## 2.2 Experimental techniques

### 2.2.1 Electrochemical measurements

Electrochemical measurements are essential in corrosion engineering and corrosion science for its importance in predicting the service life of metallic compounds used in chemical and construction industries. The following electrochemical methods were used and their results were discussed in this project: Open Cicuit Potential (OCP) Linear polarization Resistance (LPR) and Electrochemical Impedance Spectroscopy (EIS).

#### 2.2.1.1 Open Cicuit Potential (OCP)

Open Cicuit Potential (OCP) consists in a period of time when no current flows, and no potential is applied to the working electrode. The cell is disconnected from the power amplifier. On the cell, potential measurements are available. Thus, the evolution of the residual potential can be recorded. This period is usually used as the pre-processing time or to achieve thermodynamic equilibrium of the system.

In corrosion, the changes in the OCP vs. time of the corroding metal is determined by monitoring the OCP as a function of time. Take the examples of some sacrificial and barrier coatings which is commonly used in corrosion protection (Figure 10) [40]. The stability of the coating is controlled by the severity of the corrosion solution, the thickness of the coating, and the potential difference between the underlying metal and the sacrificial or barrier coating.

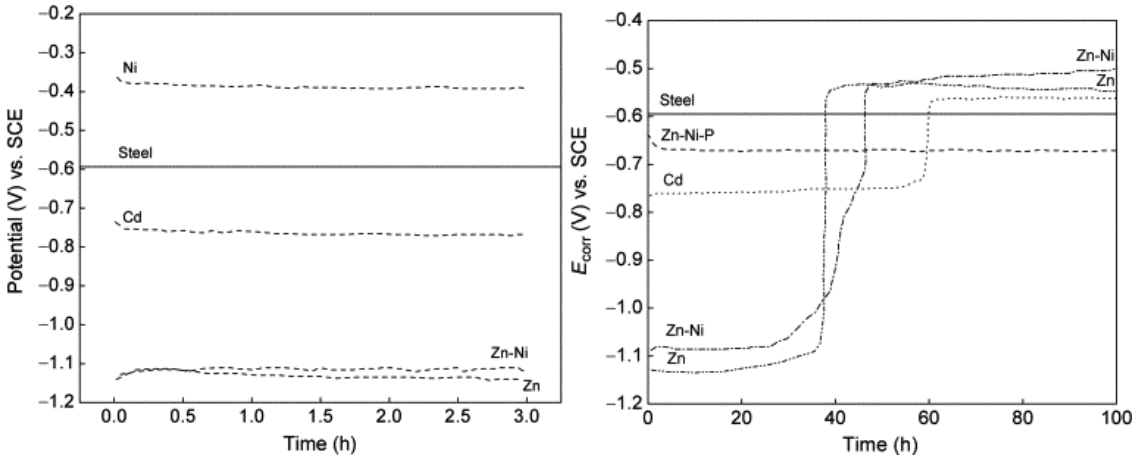


Figure 10: Open circuit potential vs. time of various coatings on a steel in 0.5M $Na_2SO_4$ + 0.5M boric acid solution at a pH of 7.0; (a) For 3.0 hours; (b) For 100 hours [40]

This OCP vs. time measurements reveals the sacrificial properties of coatings by using the scratch model approach. It can be seen that the coating with more negative values such as zinc coating results in a high level of sacrificial protection to underlying steel and inhibits hydrogen penetration into the bulk of the alloy. However, the short life due to the high rate of galvanic corrosion prohibits it to become the promising materials used in the coating. As shown in Figure 10b, the values of OCP for Zn-Ni and Zn-Ni-Cd, Zn-Ni-Cu, Ni-Zn, and electroless Ni-Zn-P are more positive than that of pure zinc (-1.1 V vs. SCE), which means that adding more noble elements is the deposit shift the potentials to anodic way, so to decrease the galvanic corrosion [41].

#### 2.2.1.2 Linear polarization Resistance (LPR)

Linear polarization Resistance (LPR) is one of the electrochemical polarization techniques. John Alfred Valentine Butler and Max Volmer established Butler-Volmer Model based on electrode kinetics and described the polarization by the current-potential equation:

$$i = i_0\{\frac{C_O(0,t)}{C_O(\infty,t)}exp[\frac{\alpha z F\eta}{RT}] - \frac{C_R(0,t)}{C_R(\infty,t)}exp[-\frac{(1-\alpha)zF\eta}{RT}]\} \tag{1}$$

In hydrodynamics, mass transfer by forced convection into the electrochemical cell containing static electrodes is an efficient method for achieving a homogeneous electrolyte solution. In this case, the metal ion concentration $C_O(x,t)$ is uniform, i.e. the current-potential equation defined by equation 1 becomes independent of mass transfer effects, thus, all $C_O(x,t)$ and $C_R(x,t)$ terms can be cancelled out, resulted in a simplified expression which is the Butler–Volmer classical equation [42]:

$$i = i_0\{exp[\frac{\alpha z F\eta}{RT}] - exp[-\frac{(1-\alpha)zF\eta}{RT}]\} \tag{2}$$

$i$ electrode current density, $A/m^2$ (defined as j = I/S)

$i_0$ exchange current density, $A/m^2$

$T$ absolute temperature, K

$z$ number of electrons involved in the electrode reaction

$F$ Faraday constant

$R$ universal gas constant

$C_O(0,t)$ the time-dependent concentration of the species to be oxidized at the distance zero from the surface

$C_R(0,t)$ the time-dependent concentration of the species to be reduced at the distance zero from the surface

$C_O(\infty,t)$ the bulk concentration of the species to be oxidized, $mol/cm^3$

$C_R(\infty,t)$ the bulk concentration of the species to be reduced, $mol/cm^3$

$\alpha$ so-called anodic charge transfer coefficient, dimensionless

$\eta$ activation overpotential (defined as $\eta = E - E_{eq}$)

Sometimes $\frac{zF}{RT}$ is replaced by the sign of $f$.

Linear polarization (LP), as schematically shown in Figure 11, covers both anodic and cathodic portions of the potential $E$ versus current density $i$ curve.

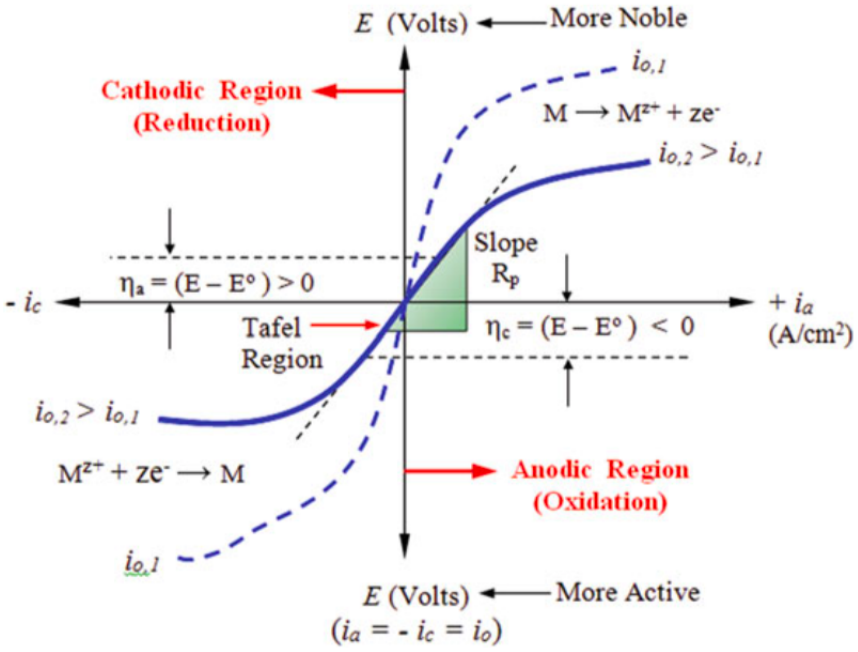


Figure 11: Schematic linear polarization curves for two different exchange current densities. The anodic and cathodic overpotentials and the slope are the polarization parameters [43]

When the potential is far from the corrosion potential, $E_{corr}$, both anodic and cathodic reactions are controlled by charge transfer can be expressed by anodic Tafel slope $\beta_a$ and cathodic Tafel slope $\beta_c$. They are defined by manipulating equation 2 to yield the anodic ($i_a$) and the cathodic ($i_c$) current densities as

$$i_a = i_0 \exp[\frac{\alpha z F \eta_a}{RT}] \quad (for\ i_a >> i_c, \eta_a >> \eta_c) \tag{3}$$

$$i_c = -i_0 \exp[-\frac{(1-\alpha) z F \eta_a}{RT}] \quad (for\ i_c >> i_a, \eta_c >> \eta_a) \tag{4}$$

Recall that $\alpha$ is the symmetry factor or charge-transfer coefficient. Solving Equation 3 and 4 for the over-potentials and Tafel slopes become

$$\beta_a = \frac{2.303RT}{\alpha z F} = \frac{(1-\alpha)\beta_c}{\alpha} \tag{5}$$

$$\beta_c = \frac{2.303RT}{(1-\alpha) z F} = \frac{\alpha \beta_a}{(1-\alpha)} \tag{6}$$

For activation polarization, the linear polarization is confined to a small magnitude of the over-potentials $\eta_a$ and $\eta_c$ , respectively, using linear coordinates. This technique allows the determination of $i_{corr}$ using a potential range of ˙10 mV from the corrosion potential $E_{corr}$. Prior to determining $i_{corr}$, the polarization resistance $R_p$ is estimated from the linear slope of the curve shown in Figure 11 based on Stern-Geary equation [44]:

$$R_p \approx \frac{1}{i_0} \frac{\beta_a \beta_c}{2.303(\beta_a + \beta_c)} = \frac{\Delta E}{\Delta i_{\Delta E \to 0}} \tag{7}$$

#### 2.2.1.3 Electrochemical Impedance Spectroscopy (EIS)

The polarization impedance of an electrode involves the determination of basic parameters, such as polarization resistance ($R_p$) and capacitance ($C_dl$). Subsequently, the impedance of the working electrode is determined as a useful kinetic reference.

Basically, when the electrode is immersed in the electrolyte, an ionic layer is formed by the combination of the metal and electrolyte ions, which generates a charge distribution in the interface region. It has unique characteristics which are related to the internal potential of the half-cell and the electric double-layer impedance. This means that the electrode-electrolyte interface is disturbed by a current flow.

In theory, the interface will be disturbed by the amount of current flowing through the interface and the type of ionic reactions that may occur within the interface thickness. The ionic behavior within the interface dimension can be modeled according to the conceptual electric double-layer. However, the polarization impedance experiment is also based on a conceptual circuit model that considers the mechanism of charge transfer or ionic diffusion to determine the polarization impedance, which is then used to estimate the corrosion rate of a specific electrode in the particular electrolyte [45].

Electrochemical Impedance Spectroscopy (EIS) is widely used for the characterization of electrode processes and complex interfaces. It examines the response of the corroding system to "ac" excitations at frequencies from 10mHz to 100kHz. This method is very useful to study the passivation of metals to determine corrosion rates and to study the inhibitor effects, sacrificial and barrier coating performance, and the disbondment of polymer-coated metals [41][46][47].

EIS can usually be measured by using a "single-sine" method where the frequencies are measured in sequence or by using a multisine implementation that can measure all frequencies at once, but later requires a Fourier transform [48]. The system response analysis contains

information about the interface. The data obtained after EIS are often analyzed by using equivalent circuit modelling which is an electronic circuit consisting of a specific combination of resistors and capacitors represents an electrode interface undergoing an electrochemical reaction.

Electrochemical impedance is normally measured using a small excitation signal to make the cell's response pseudo-linear. In a linear or pseudo-linear system, the current response to a sinusoidal potential will be a sinusoid at the same frequency but shifted in phase (see Figure 12) [49]. And corresponding mathematical expressions are listed below:

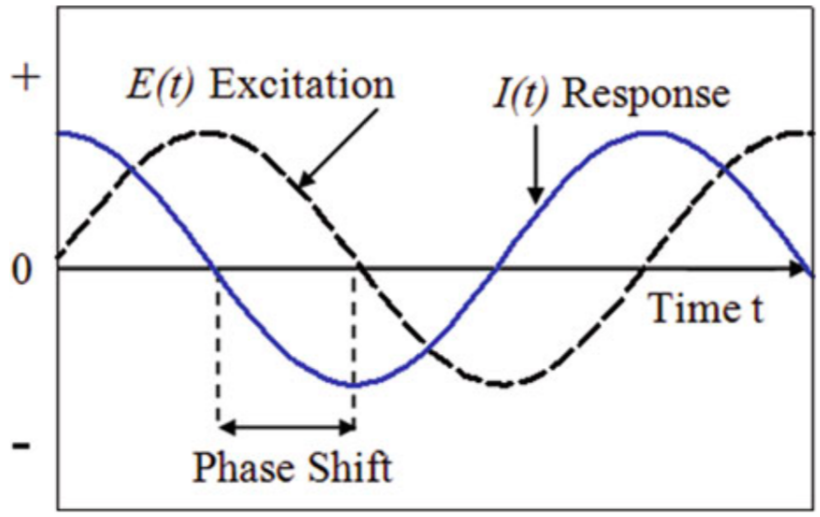


Figure 12: Schematic sinusoidal potential excitation for impedance measurements [45]

$$E_t = E_0 sin(\omega t) \tag{8}$$

$$I_t = I_0 sin(\omega t + \phi) \tag{9}$$

With Eulers relationship,

$$exp(j\phi) = cos(\phi) + jsin(\phi) \tag{10}$$

If the $E_t$ and $I_t$ are both described by natural exponent, the below equation form can be obtained,

$$Z_\omega = \frac{V}{I} = Zexp(j\phi) = Z_(cos(\phi) + jsin(\phi)) = Z^{'} + jZ^{"} \tag{11}$$

$E_t$ the input voltage, V

$E_0$ the voltage amplitude, V

$I_t$ the output measured current

$I_0$ the current amplitude, A

$\omega = 2\pi f$ angular frequency, rad/s

$\phi$ phase shift angle between $E_t$ and $I_t$, rad

$Z_\omega$ the impedance represented as a complex number

A graph of $Z = Z' + jZ"$ (where $Z'$ and $jZ''$ are the real part and imaginary part) measured at different frequencies is called a Nyquist diagram. Figure 13 shows an example of typical Nyquist diagram and its equivalent circuit. The diagram is a complex plane of Cartesian coordinates, where the real part is plotted on the X-axis and the imaginary part is plotted on the Y-axis of a chart. An alternative representation is a Bode plot in which log |Z| and $\phi$ are both plotted against log frequency [49].

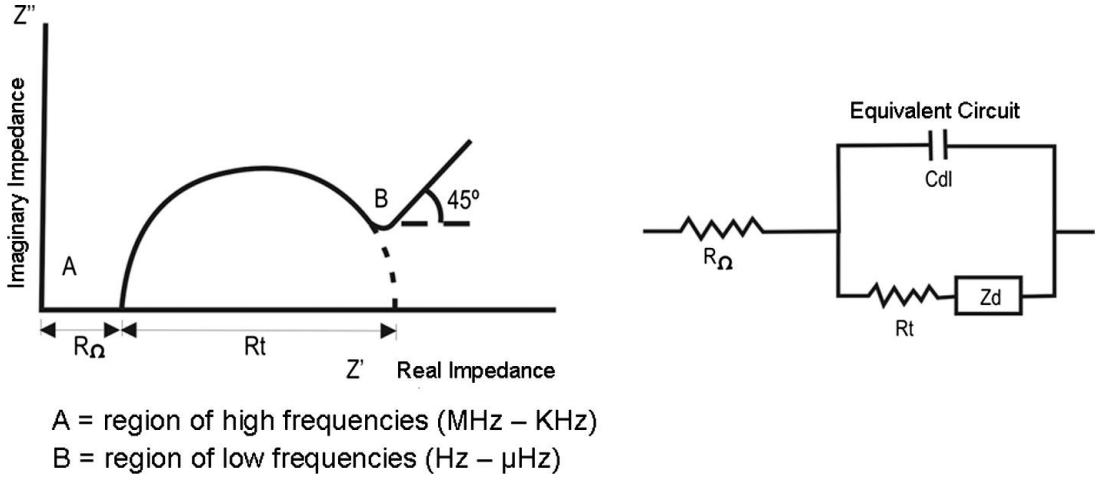


Figure 13: Nyquist diagram and its equivalent circuit, showing the effect of diffusional impedance [42]

An alternative representation is a Bode plot in which log|Z| and $\phi$ are both plotted against log frequency which is shown in Figure 14. The Bode diagram consists of a orthogonal axes plane in which two quantities on the ordinate axis can exist: the logarithm of the impedance (log|Z|) in ohms ($\phi$) or the phase angle ($\phi$) in degrees.

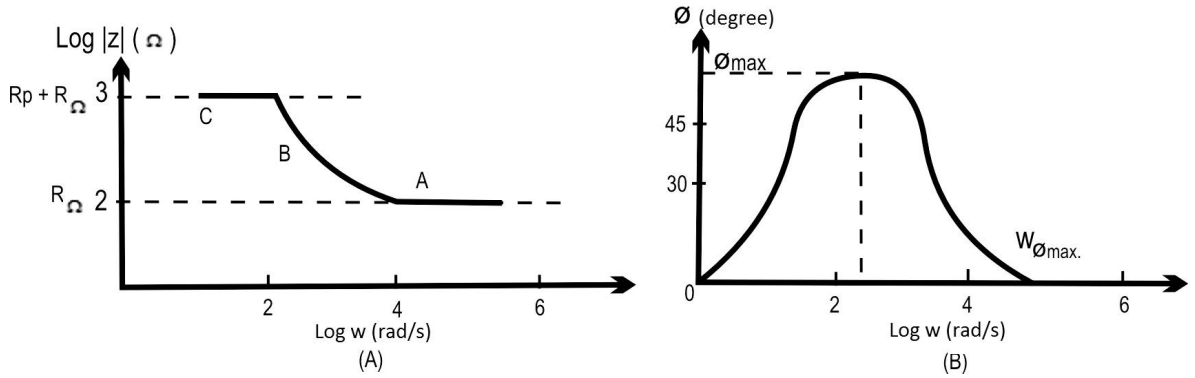


Figure 14: Bode diagram representing the impedance (modulus and phase angle) of an electrochemical corrosion system as a function of the angular frequency [42]

### 2.2.2 Surface analytical measurement

#### 2.2.2.1 Scanning electron microscopy (SEM)

A scanning electron microscopy (SEM) uses the high-energy beam of electrons to produce images. When the electron beam hits the sample as shown in Figure 15, it penetrates the sample and forms the tear-drop shape so called interaction volume. Its depth and diameters depends on the accelerating voltage and the density of the sample. The electrons bounce back out of the sample (backscattered electrons) is the result of elastic scattering and the electrons knock into atoms and displace electrons which in turn, come out of the sample (secondary electrons); alternatively X-rays, and light or heat can be the result of inelastic scattering [50]. In energy-dispersive spectroscopy (EDS), a detector is used to collect X-ray signals, it absorbed the excited photons as a function of their energy and the spectrum of energy-dependent, photon intensity is analysed to determine the chemical composition of the region of the sample excited under the electron beam [51].

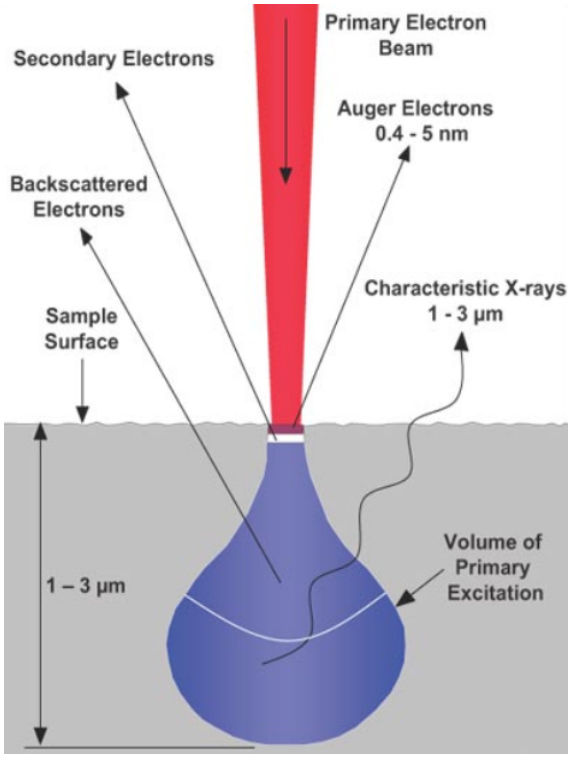


Figure 15: Schematic drawing of interaction Volume of electron beam with matter [50]

## 2.3 Experimental setup and parameters

All experiments performed on the samples were immersed in electrolyte of 5ml 0.1M aqueous NaCl. The electrolyte was poured into the electrochemical cell. A three-electrode setup was employed consisting of the aluminum sample as working electrode, silver chloride (AgCl) as reference electrode and platinum as counter electrode. The electrochemical workstation VSP-300 of Bio-Logic Science Instruments was used to perform the experiments. In this experiment, due to the limited volume of electrolyte, parafilm was used to cover the container to prevent liquid volatilisation. The schematic diagram of three-electrode setup is shown in Figure 16.

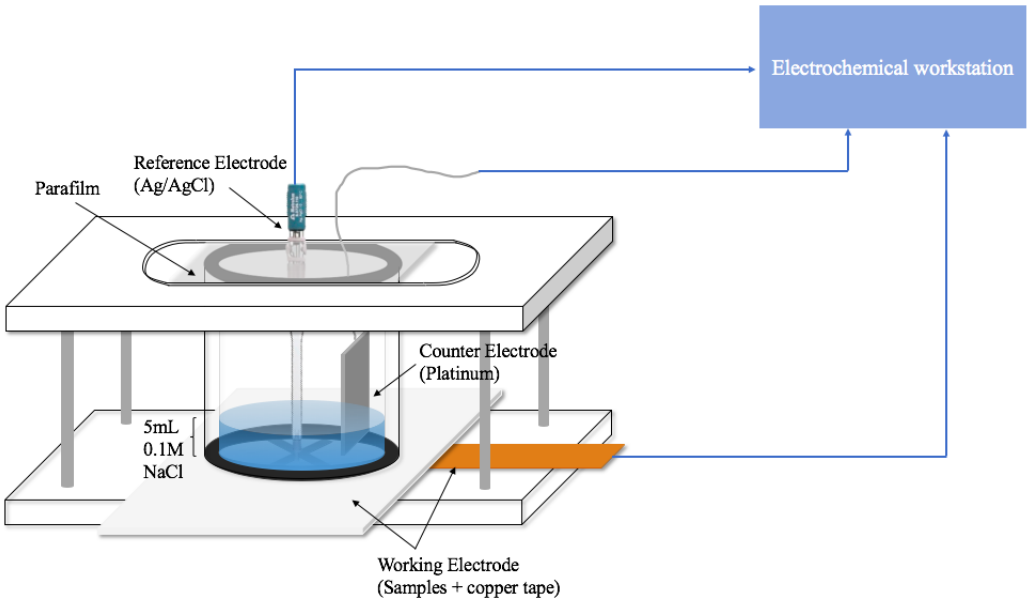


Figure 16: Schematic diagram of three-electrode setup

OCP, LPR and EIS measurements which were used for the investigation of layer formation were recorded at 2-hours intervals for 24 hours in total. After the first 24 hours, the measurements were recorded at 24-hours intervals for the following 6 days. The total time of the data collection is 168 hours. The LPR curves were measured at a linear potential sweep rate 0.167 mV/sec with a potential range of $\pm$10mV. The EIS measurements were performed over a frequency range between $10^{-2}$ and $10^{5}$ with 10 mV sinusoidal amplitude, 2 measurements per frequency and 10 steps per decade. The detailed setup is shown in Figure 17, Figure 18 and Figure 19.

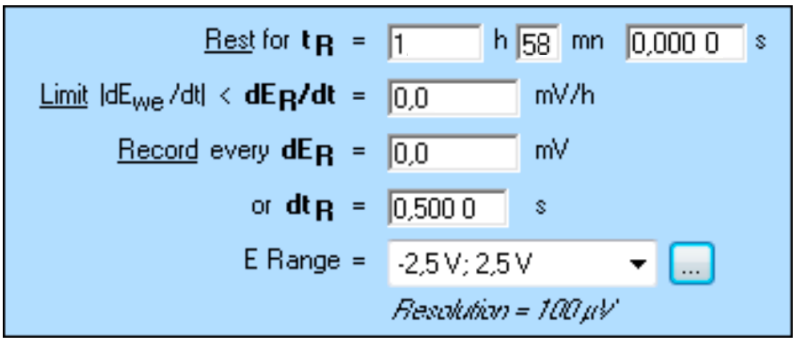


Figure 17: Software setup of OCP

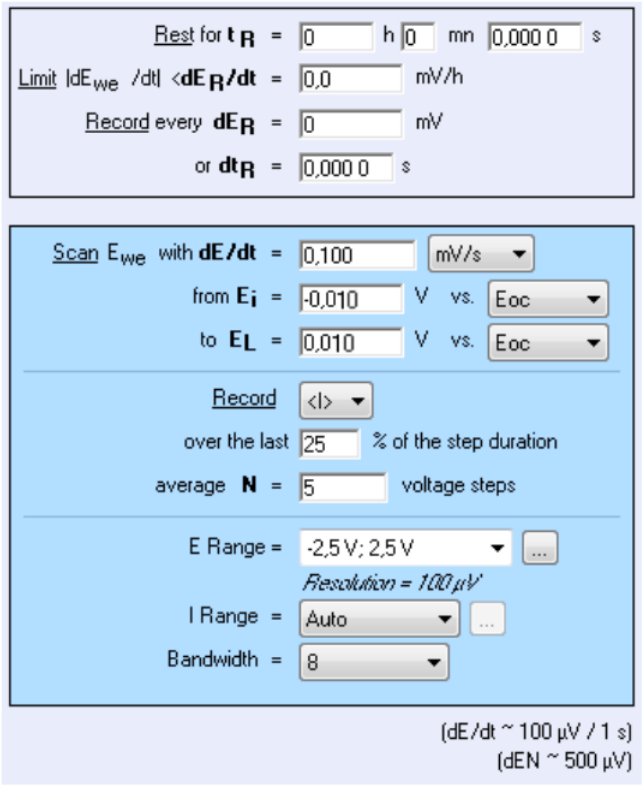


Figure 18: Software setup of LPR

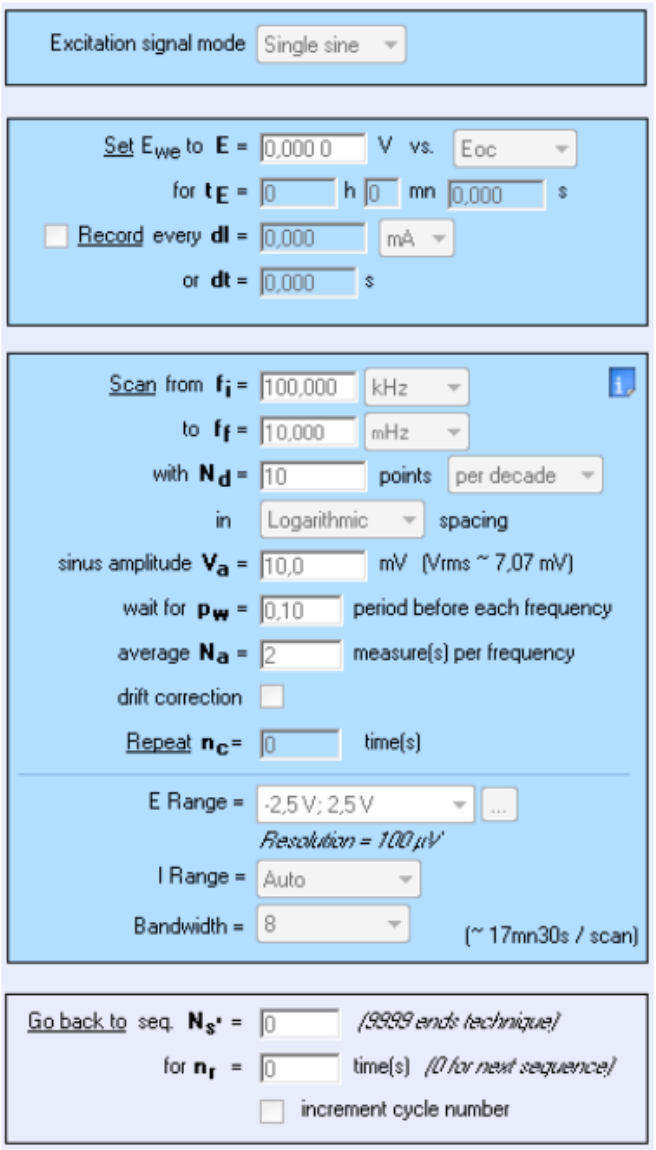


Figure 19: Software setup of EIS

After the experiment, the surface of morphology of protective layers were examined by using JOEL JSM IT100 scanning electron microscopy (SEM) using the secondary electron detector (SEI) or back-scattered electron detector (BSD) at the acceleration of 15kV. Then the samples were cut by the grinding wheel to show the cross section of samples and embedded in conductive resins by cold mounting, then experience grinding from 180-4000 grit silicon carbide abrasive papers with distilled water as lubricant. After the polishing by $3\mu$ and $1\mu$ diamond pasts, the samples were dried and degassed in the vacuum chamber until the pressure of 0.1mbar was reached. Finally, the samples were put into the SEM for the characterization of morphology of cross section with the same parameters used during the surface morphology characterization.

# 3 Results and discussion

In this chapter, two systems of AA2024-T3 and AA2198-T8 were evaluated through the electrochemical response of corrosion inhibiting layers formed in a defect from lithium-leaching organic coating under 5ml 0.1 M NaCl electrolyte. Initially, OCP measurement was used to identify the formation and evolution of protective layer. Then, LPR recordings were measured and calculated as a function of time. The values of LPR can provide the information of the protective layer in each step of formation and illustrate the corrosion protection of coatings. LPR measurements were analyzed to compare the inhibition performances of these two systems. The difference between the samples with and without the pre-treatment (NSS) were also analyzed. Repetitive OCP and LPR measurements of these samples were performed in order to calculate the average values of results so that the reliability can be guaranteed. In addition, EIS tests were conducted to investigate the details of the protective layer. Finally, the SEM images were investigated to correspond to the results obtained from the electrochemical experiments.

## 3.1 System AA2024-T3

### 3.1.1 Formation of protective layer (No NSS)

#### 3.1.1.1 Electrochemical Characterization

**OCP**

In this project, the OCP would be involved to discuss with respect to the layer formation. It has been demonstrated that the mechanism of the formation of protective layer involves multiple stages. As illustrated in Figure 20, In the first stage, it experiences the activation phase, also, the oxide is thinning due to the adsorption of chloride ions and the alkaline nature of the solution after lithium leaching out (Equation 12).

$$Al_2O_3 + 2\,OH^- + 3\,H_2O \rightleftarrows 2\,Al(OH)_4{}^- \tag{12}$$

When the oxide layer is thinned sufficiently, the OCP reaches its minimum value, and then stage II starts. Direct dissolution of aluminum results in the formation of Aluminum gel at the surface of metal (Equation 13 and 14). Figure 20 shows that at stage II OCP increases to

a plateau which is regarded as the second stage of the layer formation [52].

$$\mathrm{Al} + 3\,\mathrm{e}^- \rightleftharpoons \mathrm{Al}^{3+} \tag{13}$$

$$\mathrm{Al}^{3+} + 3\,\mathrm{OH}^- \rightleftharpoons \mathrm{Al(OH)_3} \tag{14}$$

Under the alkaline conditions, the aluminium hydroxide layer will be chemically dissolved at the aluminium hydroxide/solution interface (Equation 14).

$$\mathrm{Al(OH)_3} + \mathrm{OH}^- \rightleftharpoons \mathrm{Al(OH)_4}^- \tag{15}$$

The aluminum dissolution is also accompanied with hydrogen evolution as shown in Equation 16.

$$2\,\mathrm{H_2O} + 2\,\mathrm{e}^- \rightleftharpoons \mathrm{H_2} + 2\,\mathrm{OH}^- \tag{16}$$

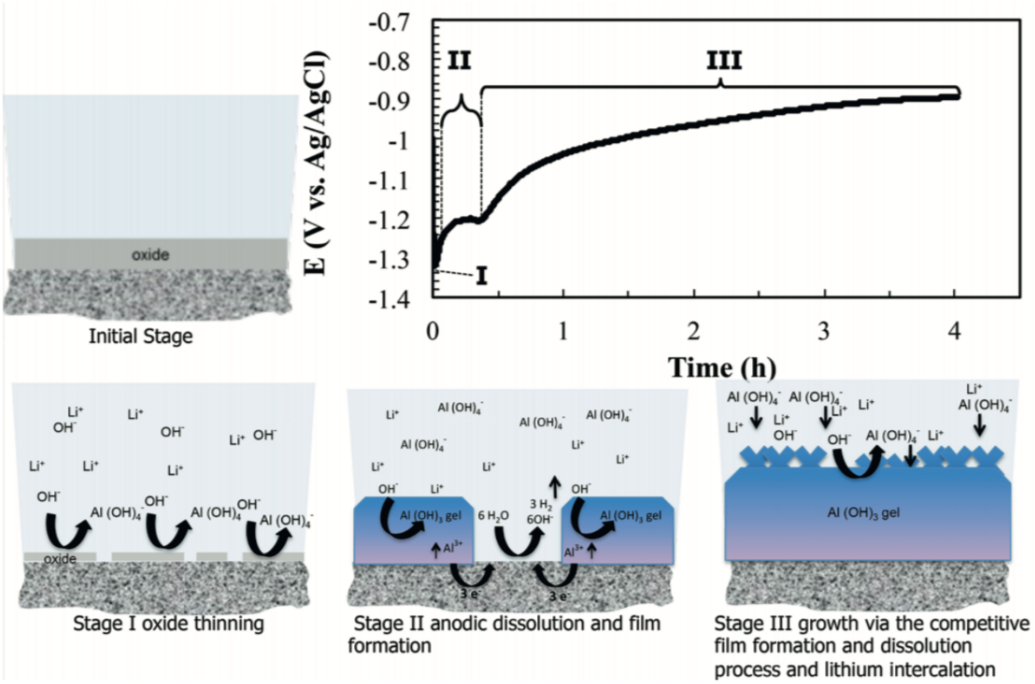


Figure 20: Schematic representation of the formation of the passive layer in relation to the development of the open circuit potential [52]

Finally, the OCP would have a second increase and reaches another plateau which can be associated with the competition between film formation and dissolution process. Figure 21 and Figure 26 show the open circuit potential evolution as function of time of different coatings applied on AA2024-T3 aluminum alloy with and without 1-week NSS in the presence of 5mL 0.1M NaCl.

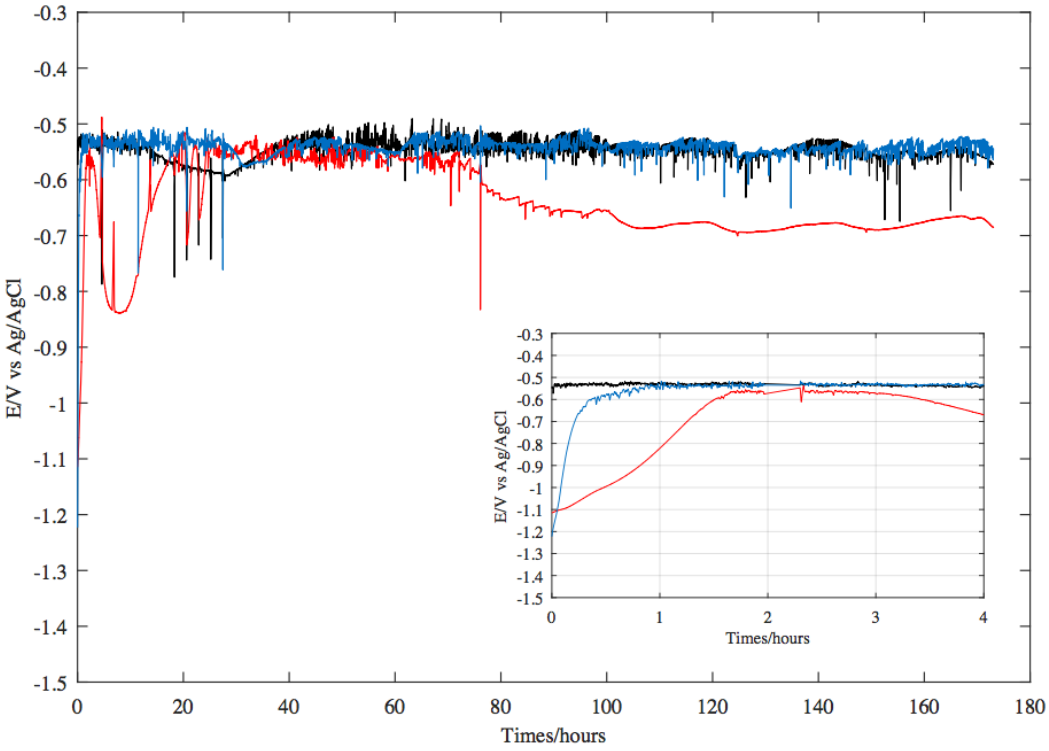


Figure 21: Open circuit potential response over time of AA2024-T3 exposed to 0.1M NaCl solution. Label key: (black) Model coating, (red) Model coating containing $Li_2CO_3$, (blue) XP420

In order to check whether the three types of coatings show the same behavior as shown in Figure 20, OCP is measured for the total 168 hours of experiment. It can be observed from Figure 21 that the coatings loaded with $Li_2CO_3$ have an initial rapid decrease to a minimum value of -1.2V vs Ag/AgCl at the first few seconds after exposure to the 5mL 0.1M NaCl solution. It can be related to the anodic activation of aluminum and the dissolution of the $Li_2CO_3$ into the electrolyte in the scribe. There is no initial reduction observed in model coating which is reasonable since only oxide layer is formed and no other measure of protection is applied on it.

By comparison between the Figure 20 and Figure 21 for the first 4 hours immersed in 0.1M NaCl, it is difficult to differentiate the stage II and III for model coating containing $Li_2CO_3$ and XP420. The potential of XP420 is rapidly increase and a plateau is observed after approximately one hours of immersion to the solution. It can be related to the faster formation of protective layer on the aluminum surface. The model coating containing $Li_2CO_3$ has longer

time about 20 hours to reach stable level which is much more than that of model coating and XP420. The trend of OCP of model coating containing $Li_2CO_3$ explains that the samples experience the oxide thinning and formation of protective layer. Then the OCP has a sharp decrease which has propensity to corrosion. After that, the protective layer continuous to form and reaches the plateau. OCP level keeps at the stable level for about 50 hours, and then followed by a decrease at slow rate and reaches another plateau around -0.7V vs Ag/AgCl.

Therefore, it can be observed that model coating containing $Li_2CO_3$ is less stable compared to other two types coating since it has the longest time before reaching the break down potential.

**LPR**

Figure 22 shows the resistance polarization of AA2024-T3 immersed in 0.1M 5ml for 24 hours and 168 hours without NSS in advance. As seen from Figure 22a and Figure 22b, after 2 hours of experiments, the resistance polarization for samples of $Li_2CO_3$-loaded coating is higher than that of model coating which implies the inhibition effect of coatings loaded with $Li_2CO_3$. It can be seen that for the first 24 hours, samples of model coating containing $Li_2CO_3$ has three phases observed during the resistance polarization evolution of 168 hours. After the initial rapid decrease about 54% from 81.38 $k\Omega.cm^2$ to 37.39 $k\Omega.cm^2$ in resistance polarization which indicates the initiation of the local corrosion, the resistance polarization is relatively linear increasing until the highest point around 600 $k\Omega.cm^2$. The resistance polarization then experiences the significant decrease to around 385 $k\Omega.cm^2$ and finally a relatively plateau around 350 $k\Omega.cm^2$ has reached. It is possible to state that the growth and dissolution process has reached a stable state and the formation of the protective layer is completed. Model coating has a relatively linear increase for all 168 hours which can related to the protection of oxide layer. XP420 also has a relatively linear increase and finally reaches the stable state at approximately 500 $k\Omega.cm^2$. It is important to note that after around 85 hours of electrochemical experiment, the resistance polarization of XP420 exceeds the resistance polarization of model coating containing $Li_2CO_3$. It reveals the stronger corrosion protection of XP420 in a long-term period. In addition, the reason for the continuously increase in model coating is mainly due to the corrosion products produced which cover the aluminum substrate and it provides the protection to against the corrosion media.

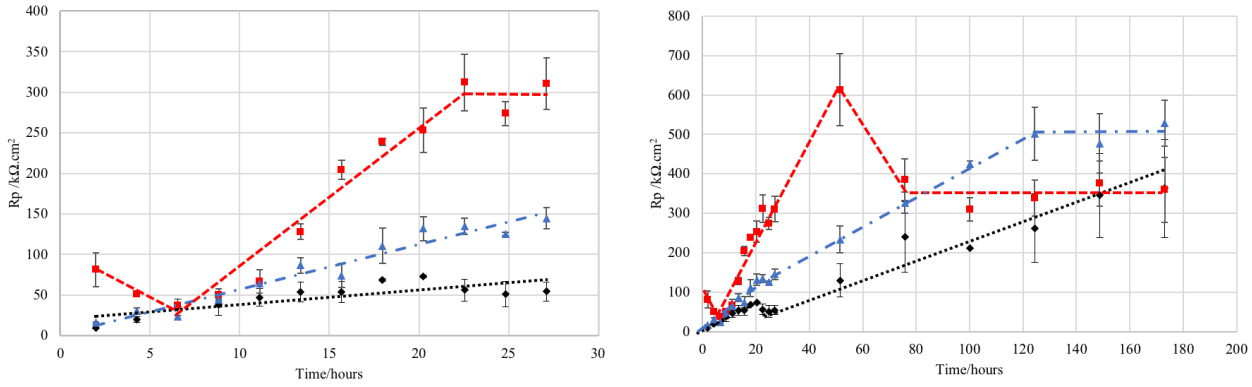


(a) First 24 hours of AA2024-T3 without NSS

(b) 168 hours of AA2024-T3 without NSS

Figure 22: Resistance polarization ($R_p$) evolution as a function of time of AA2024-T3 aluminium alloy immersed in 5ml 0.1M NaCl solution of (a)24 hours without NSS; (b) 168 hours without NSS; Label key: (black) model coating, (red) model coating containing $Li_2CO_3$, (blue) XP420

**EIS**

Electrochemical impedance spectra of samples without NSS were recorded after LPR as a function of frequency which are presented in Figure 23 and Figure 24. The Figure 23 measures EIS every 2 hours for the first 24 hours. The Figure 24 measures the EIS after first hours with 24 hours as the interval for the following 144 hours. The graphs of EIS indicate the changes in impedance modulus and phase angle over time by the fading of color. Overall, the impedance modulus of all three specimens increase with time for the first 24 hours. The increase is the most significant for the model coating containing $Li_2CO_3$ as shown in the impedance modulus plots in Figure 23b. The exposure to 0.1 M NaCl solution results in around an order of magnitude compared to the model coating (Figure 23a), which indicates the inhibitive properties of the organic corrosion inhibitors. It can be seen that the impedance modulus of model coating containing $Li_2CO_3$ begins to decrease after reaching the highest value of $10^5.38\ \Omega.cm^2$ at 48 hours of experiment, the value at this point is not exactly corresponds to the values obtained in LPR, but the trends are the same in the EIS and LPR graphs. Apart from that, the impedance modulus of XP420 increases continuously and exceed the highest value of model coating containing $Li_2CO_3$ after around 96 hours of experiment which validates the results of LPR discussed before as shown in Figure 22.

When considering the Bode phase angle plot of model coating (Figure 23a), two time-constants are observed. One is in relatively low frequency region ($10^{-2}$ Hz to $10^0$ Hz) and the other is in the middle frequency of $10^0$ Hz to $10^2$ Hz. The former one is corresponding to the polarization resistance of the corrosion reaction of the base metal. The latter one indicates the existence of oxide layer. As for model coating containing $Li_2CO_3$, the peak of phase angle at the relatively low frequency decreases initially which means that the oxide layer is thinning. As time goes by, with the broadened shape of phase angle plot and the increase in

impedance modulus in middle range of frequency, a layer is formed on the surface of the alloy.

The situation observed from XP420(Figure 23c) shows that the same time-constant is observed in the middle frequency of $10^0$ Hz to $10^2$ Hz. However, a shoulder which can be related to the other time-constant is observed gradually at the high frequency between $10^{2.5}$ Hz to $10^5$, and it can be associated with the double layer capacitance. After the first 24 hours, model coating and XP420 behave similar in phase plot for the following 6 days (Figure 24a and 24c). The third time-constant is not identified for XP420. Thus, further research is necessary to confirm the existence of lithium-leaching protective layer.

The totally different scenario of model coating containing $Li_2CO_3$ is observed from the phase angle plots as shown in Figure 23b and 24b. There are two time-constants observed from the phase angle plots of model coating containing $Li_2CO_3$ for the first 24 hours. Later, three time-constants are observed. They can be attributed to the generation of corrosion protective layer on the alloy sample. One is in the low frequency range of $10^{-2}$ Hz to $10^0$ Hz, the other two are located at higher frequency range of $10^0$ Hz to $10^{2.5}$ Hz and $10^{2.5}$ Hz to $10^5$ Hz which represent the dense and porous organic inhibitor layer.

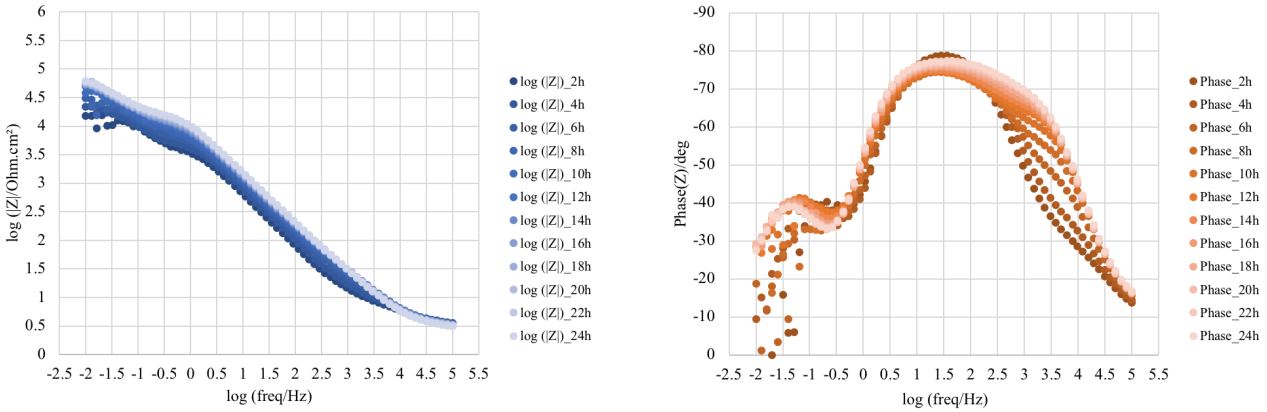


(a) Bode plot of model coating

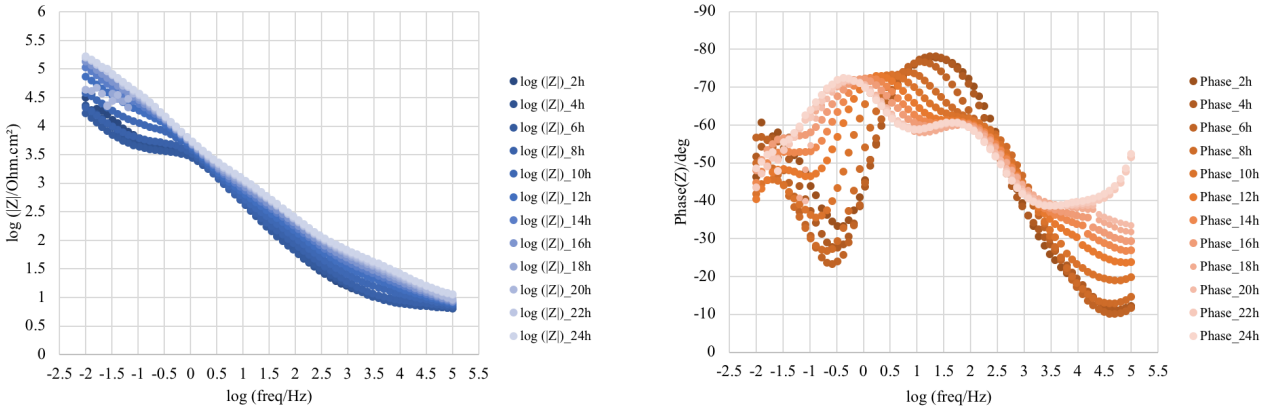


(b) Bode plot of model coating containing $Li_2CO_3$

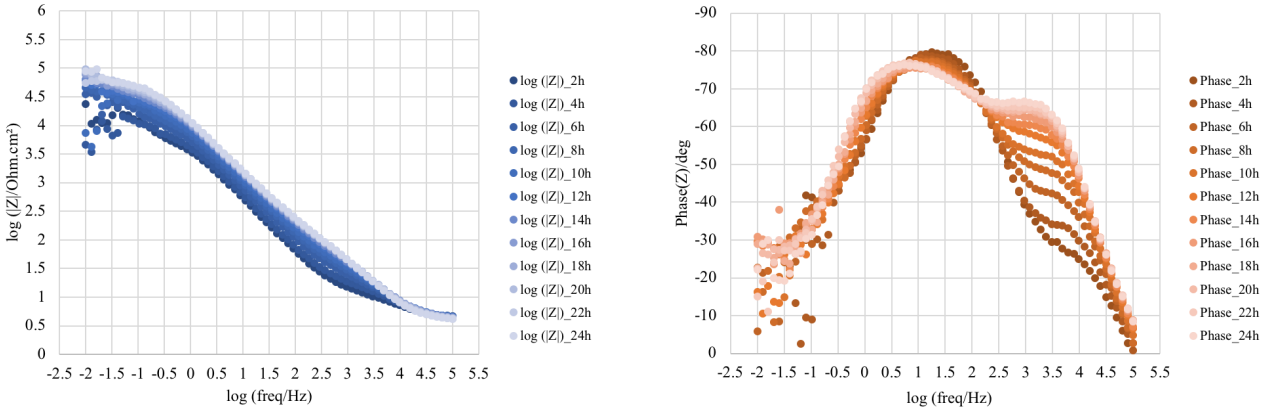


(c) Bode plot of XP420

Figure 23: Electrochemical impedance spectra of AA2024-T3 aluminum alloy of first 24 hours exposure to the 0.1 M NaCl solution without NSS before the electrochemical experiment. Impedance modulus and phase angle plot of (a) Model coating; (b) Model coating containing $Li_2CO_3$; (c) XP420; Label key: as time goes on, the color changes from dark to light

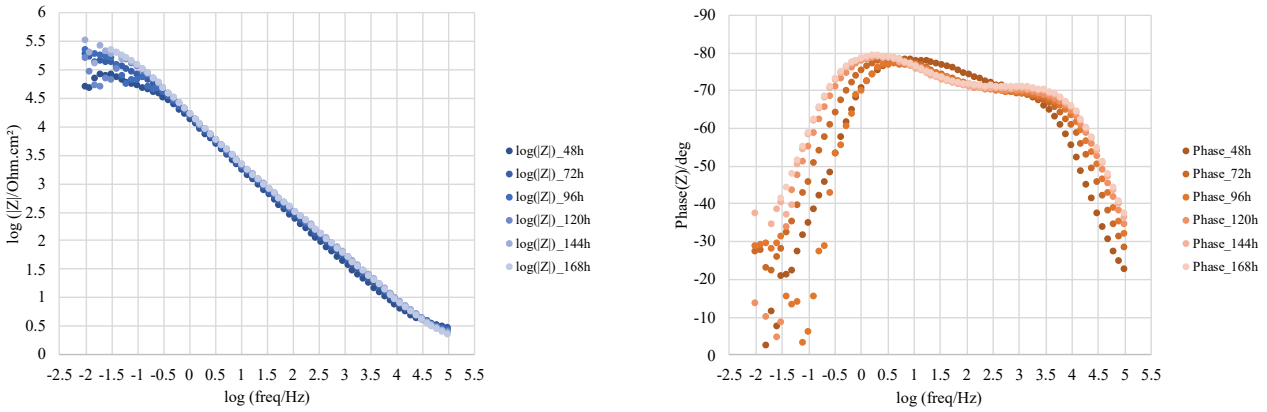


(a) Bode plot of model coating

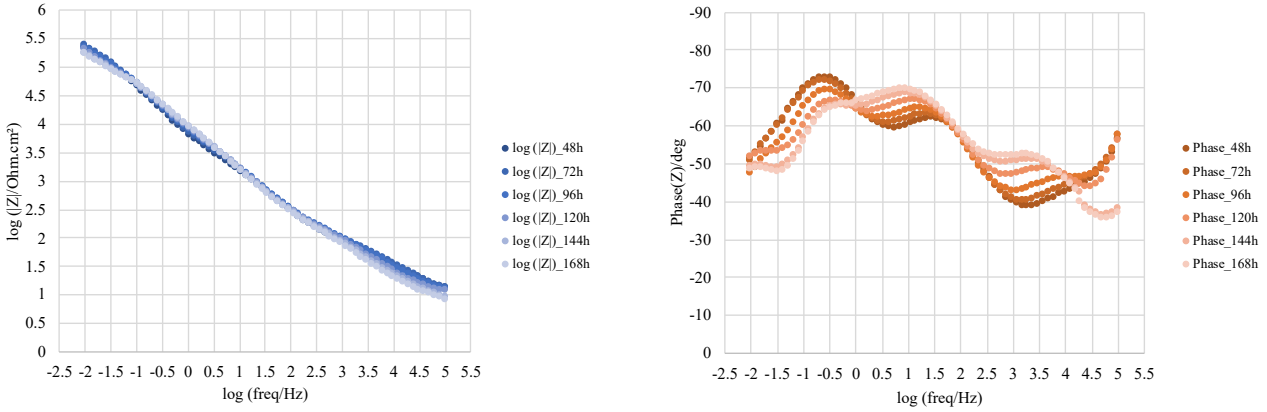


(b) Bode plot of model coating containing $Li_2CO_3$

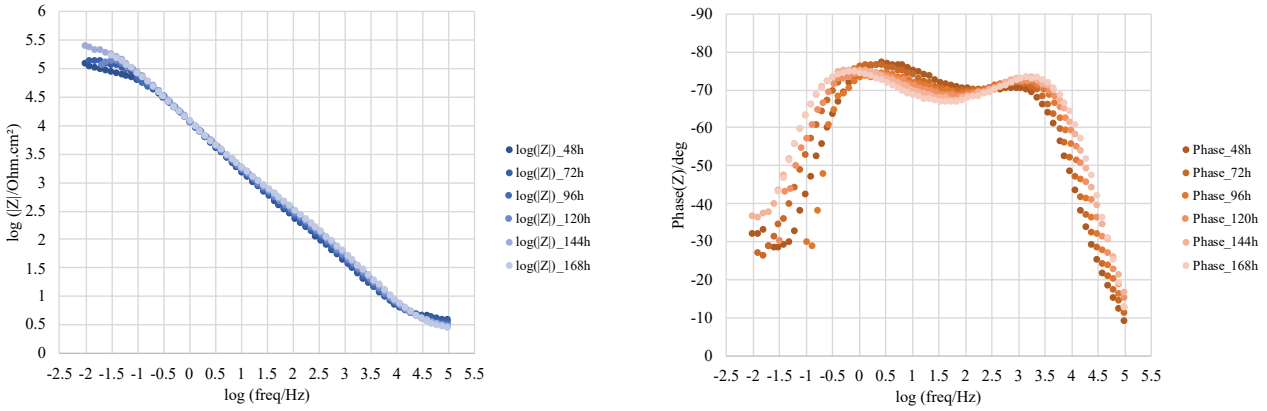


(c) Bode plot of XP420

Figure 24: Electrochemical impedance spectra of AA2024-T3 aluminum alloy of first 168 hours exposure to the 0.1 M NaCl solution without NSS before the electrochemical experiment. Impedance modulus and phase angle plot of (a) Model coating; (b) Model coating containing $Li_2CO_3$; (c) XP420; Label key: as time goes on, the color changes from dark to light

### 3.1.2 Morphological observations

#### 3.1.2.1 Morphology of cross section

In previous work, the morphology of cross section of protective layer on AA2024-T3 aluminum alloy illustrated that the protective layer consists of a dense barrier region at the metal/deposited layer interface, a porous region in the middle, and a columnar outer region [33].

In this work, the cross section of three types of coatings were observed after the immersion in 0.1M NaCl without NSS for 168 hours of experiments (Figure 25). By the comparison between non-inhibiting coating and $Li_2CO_3$-loaded coatings samples, it is obvious that there are much thicker layer formed on the interface of $Li_2CO_3$-loaded coating samples which can also be identified through the Table 7. In Figure 25d, model coating containing $Li_2CO_3$ shows the clear uniformity in same shade of grey which means only one layer is observed, but the thickness is varied. What is more, it is important to note that there are two layers observed in XP420 as shown in Figure 25f. The one close to the metal/deposited layer interface is denser than the outer region. Due to the limitations of the resolution of SEM, it is difficult to identify whether outer layer is porous or columnar. Therefore, the closer examination is necessary to further investigate the protective layer formed on XP420 sample.

| **Type of coating** | **Thickness of layer** | |
|---|---|---|
| | **Average ($\mu$ m)** | **Standard deviation** |
| Model coating | 0.59 | 0.20 |
| Model coating containing $Li_2CO_3$ | 1.61 | 0.20 |
| XP420 | 2.81 | 0.47 |

Table 7: Thickness of layer of AA2024-T3 without NSS after experiment

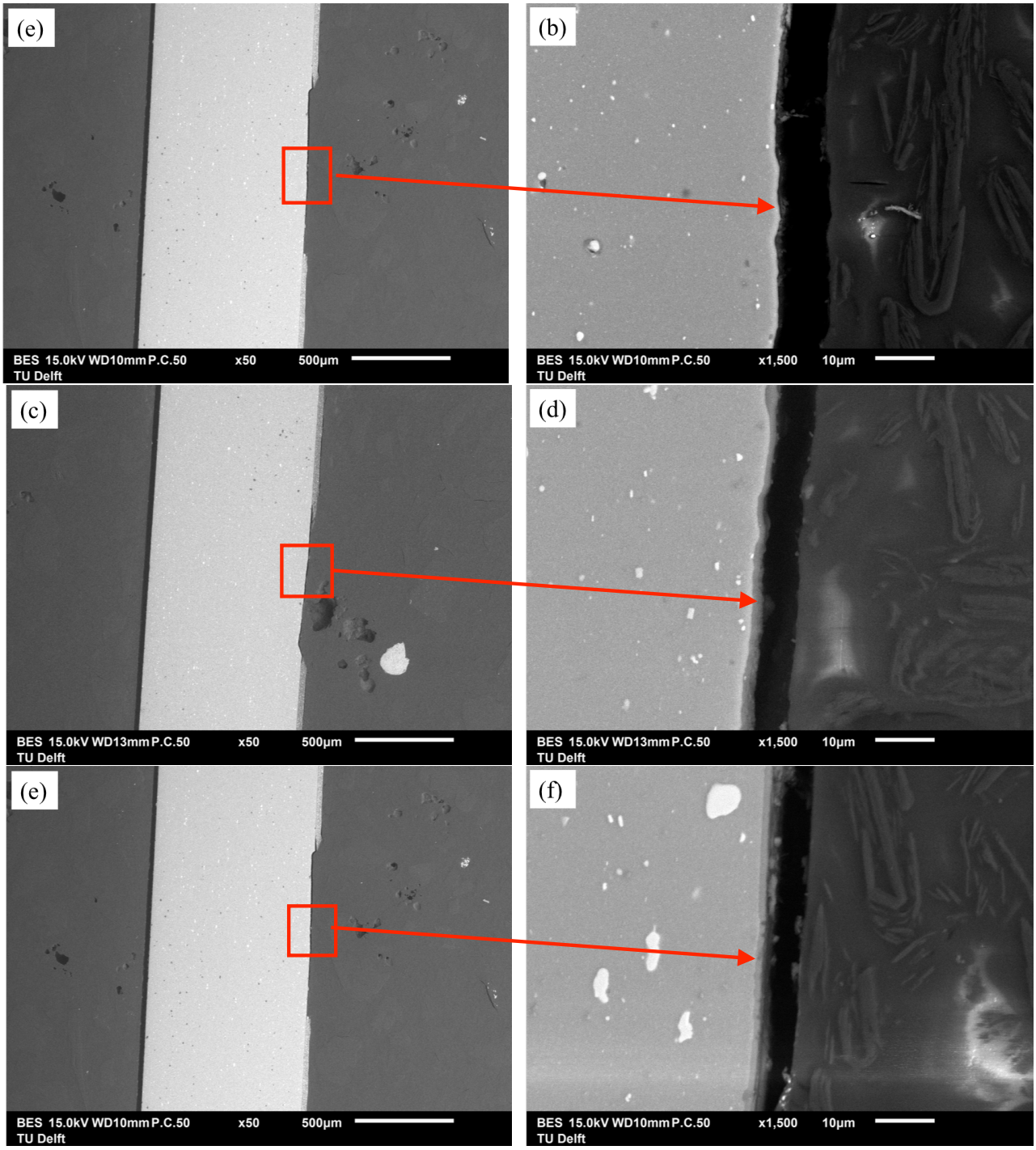


Figure 25: Cross section of the scribed area of AA2024-T3 without 1-week NSS in advance after the immersion in 0.1 M NaCl for 168 hours: Backscattered electron images of (a) Model coating in 50X magnification; (b) Model coating in 1500X magnification; (c) Model coating containing $Li_2CO_3$ in 50X magnification; (d) Model coating containing $Li_2CO_3$ in 1500X magnification ; (e) XP420 in 50X magnification; (f) XP420 in 1500X magnification

### 3.1.3 Stability of protective layer (with NSS)

#### 3.1.3.1 Electrochemical Characterization

**OCP**

In the case scenario of samples of AA2024-T3 immersed in NSS for one week prior to the electrochemical experiment (Figure 26), the potential of all OCP of three types of samples are at the stable level of approximately -0.50V vs Ag/AgCl. The reason for this could be the completed formation of protective layer of $Li_2CO_3$-loaded coatings and the formation of oxide layer for model coating during the NSS. After 90 hours, it can be observed that the OCP of model coating and model coating containing $Li_2CO_3$ starts to decrease at very low rate, but XP420 still remains stable. These phenomenon illustrates the tendency of corrosion of samples applied with model coating and model coating containing $Li_2CO_3$, and the stability of protective layer of XP420.

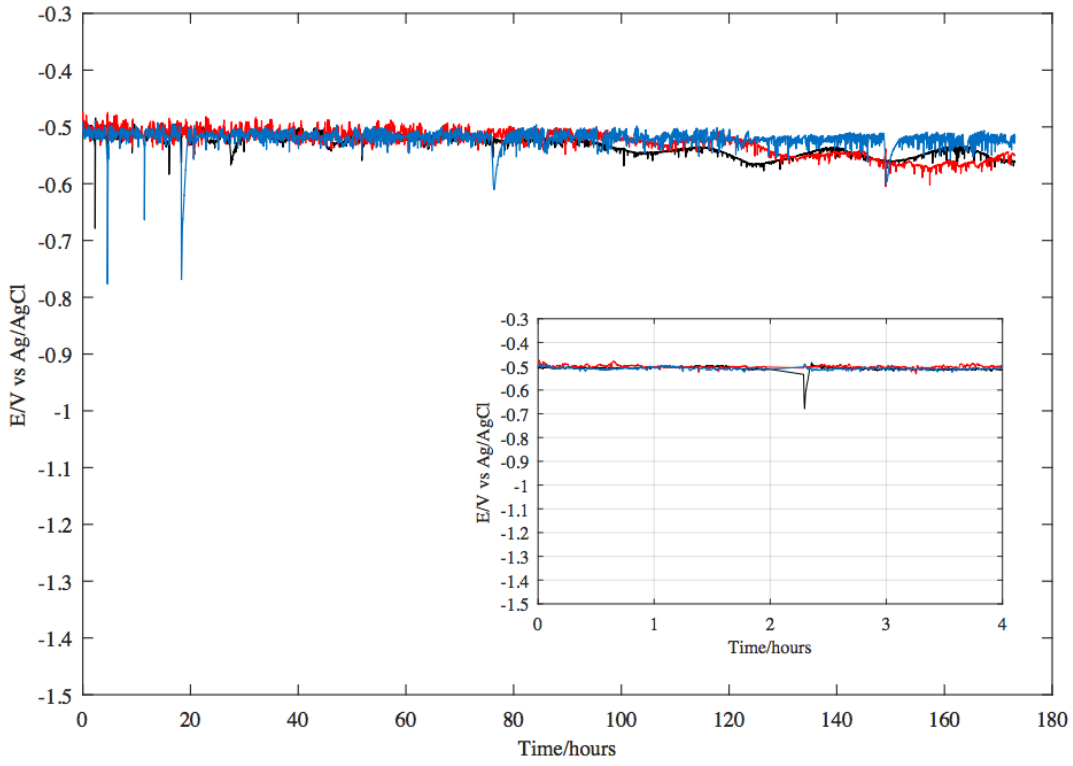


Figure 26: Open circuit potential response over time of AA2024-T3 exposed to 0.1M NaCl solution. The samples have been in 1-week NSS before test. Label key: (black) Model coating, (red) Model coating containing $Li_2CO_3$, (blue) XP420

## LPR

The Figure 27 demonstrates how the coatings behave afterwards which is represented by the resistance polarization evolution as a function of time with 1-week NSS in advance. In this case, certain protective layer was already formed. In Figure 27, the $Li_2CO_3$-loaded coatings have higher initial values than that of model coating. XP420 shows a higher value than that observed in the case without NSS which identifies the formation of protective layer before the experiment. Then the polarization resistance of three types of samples have a relatively linear increase at low rate. The relative linearly increase maintains around 24 hours and keep a relatively lower rate of increase for the model coating and XP420 for the rest of time. For model coating containing $Li_2CO_3$, it experiences a relatively linear increase with low rate and then a significant increase after 100 hours of experiment and finally reaches the stable level around 600 $k\Omega.cm^2$ which is much higher than other two specimens. However, it is important to note that there is a large range of standard error observed for the final two values of polarization resistance in model coating containing $Li_2CO_3$ which may lead to the invalidity of results. Apart from that, at this final stage, it is obvious that model coating containing $Li_2CO_3$ has better corrosion protection, followed by XP420 and then model coating. Because of the continuously increase in polarization resistance of $Li_2CO_3$-loaded coatings, it can be assumed that the protective layer still evolves with time even though the samples were all experienced 1-week NSS already.

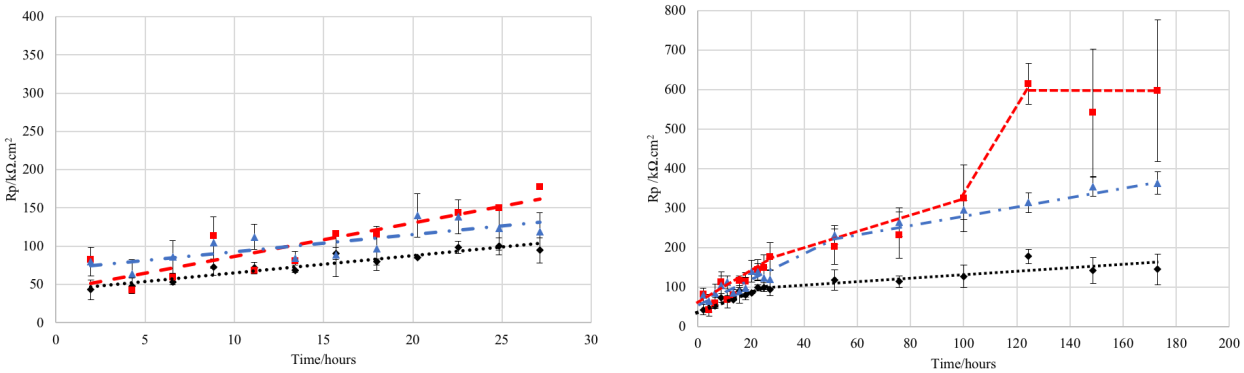


(a) First 24 hours of AA2024-T3 with NSS

(b) 168 hours of AA2024-T3 with NSS

Figure 27: Resistance polarization ($R_p$) evolution as a function of time of AA2024-T3 aluminium alloy immersed in 5ml 0.1M NaCl solution of (a)24 hours with NSS; (b) 168 hours with NSS; Label key: (black) model coating, (red) model coating containing $Li_2CO_3$, (blue) XP420

## EIS

The bode plots of impedance modulus and phase angle in Figure 28 and Figure 29 representing how the lithium-leaching protective layer with 1-week NSS behaves by immersing samples in 0.1 M NaCl solution for 24 hours and 168 hours. In Figure 28, it shows that the

impedance modulus of three specimens have no significant change. The small fluctuations in impedance modulus in the low range of frequency largely caused by the noise during the experiments which can be neglected. The time-constant shift from middle frequency to low frequency which indicates the dissolution of native oxide. From Figure 28a, the specimen without inhibitor shows two time-constants. They are related to the oxide layer from the exposure to NSS at the higher frequency and electrochemical activity at the aluminium interface in the coating defect, which are characteristic for the native oxide on aluminium at the lower frequency [53]. Figure 28b shows one time-constant at the beginning, and then two time-constants after around 12 hours of electrochemical experiments. One is in the range between $10^0$ Hz and $10^{2.5}$ Hz, the other is located in the frequency range around $10^{2.5}$ Hz to $10^5$ Hz. Figure 28c shows the similar behavior with Figure 28b but a hidden time-constant at $10^2$ Hz approximately by observing the shoulder and asymmetry of the shape of phase angle during the relative low frequency range.

From Figure 29, this behavior is becoming more and more obvious for the next 6 days of experiments for XP420 as shown in Figure 29c and happens to the sample of model coating containing $Li_2CO_3$ after first 24 hours as shown in Figure 29b. The phase angle peak of them between $10^-1$ Hz to $10^3$ Hz illustrates an asymmetric shape and a shoulder which means there are two overlapping time-constants hidden in this range. In other words, it implicates a protective layer generated in the defect area. It is further clarified by the increased impedance modulus of model coating containing $Li_2CO_3$ and broadened phase angle.

By comparison of impedance modulus between LPR and EIS results, one contrary point is observed. The values of data at 168 hours in LPR are 597 k$\Omega$.cm$^2$ for model coating containing $Li_2CO_3$ and 363 k$\Omega$.cm$^2$ for XP420. The values of data at 168 hours in EIS are 371 k$\Omega$.cm$^2$ for model coating containing $Li_2CO_3$ and 354 k$\Omega$.cm$^2$ for XP420. As discussed before In LPR section, the standard deviation is largely scattered and the reason behind it may because of artificial error during the operation or the noise from the electrochemical station.

Overall, the XP420 seems to form protective layer quicker than that of model coating containing $Li_2CO_3$ because the three time-constants are firstly found during the first 24 hour for XP420. Both of them present the inhibition effect by increased impedance of modulus and broadened shape of phase angle.

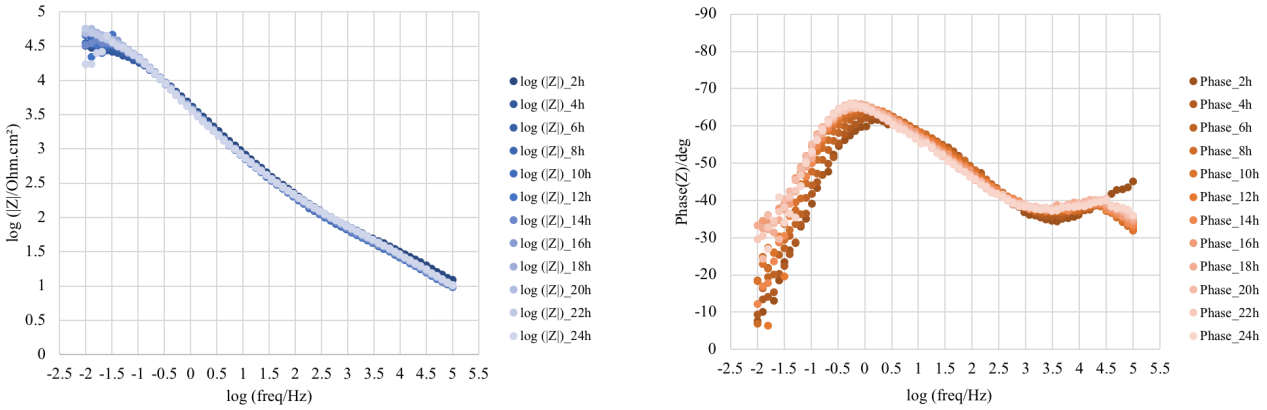


(a) Bode plot of model coating

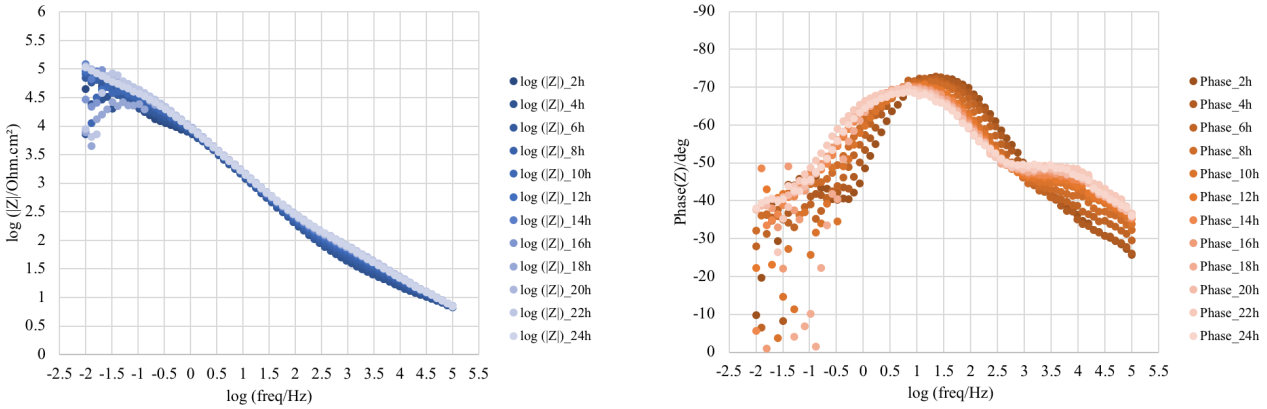


(b) Bode plot of model coating containing $Li_2CO_3$

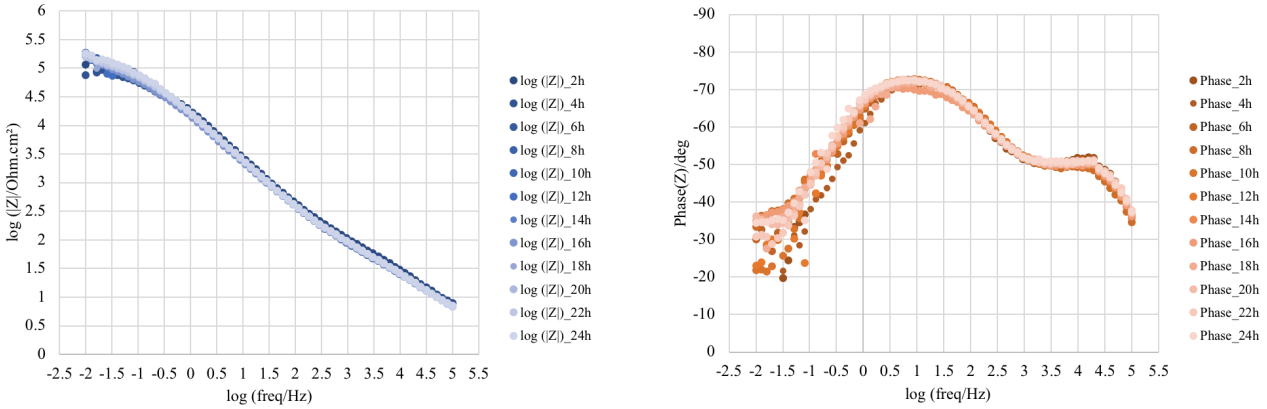


(c) Bode plot of XP420

Figure 28: Electrochemical impedance spectra of AA2024-T3 aluminum alloy of first 24 hours exposure to the 0.1 M NaCl solution with NSS before the electrochemical experiment. Impedance modulus and phase angle plot of (a) Model coating; (b) Model coating containing $Li_2CO_3$; (c) XP420; Label key: as time goes on, the color changes from dark to light

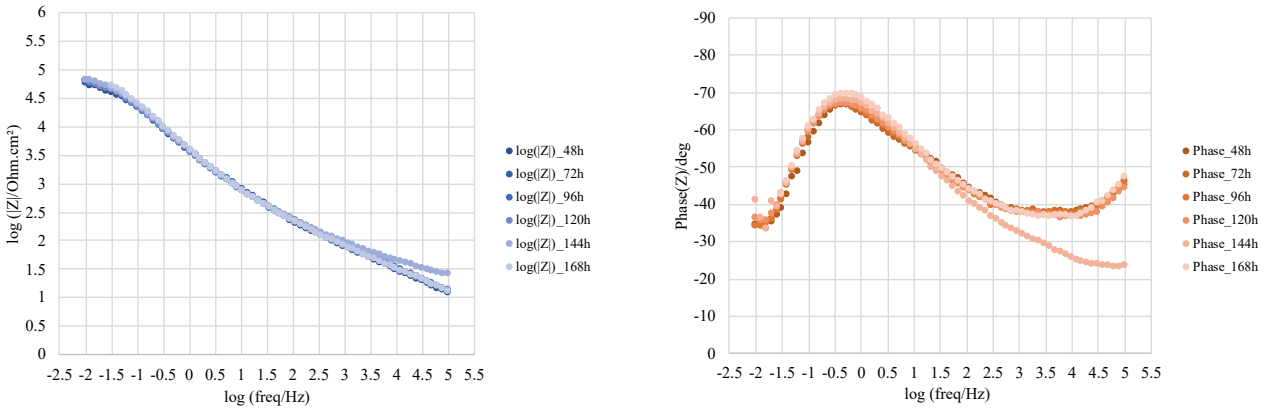


(a) Bode plot of model coating

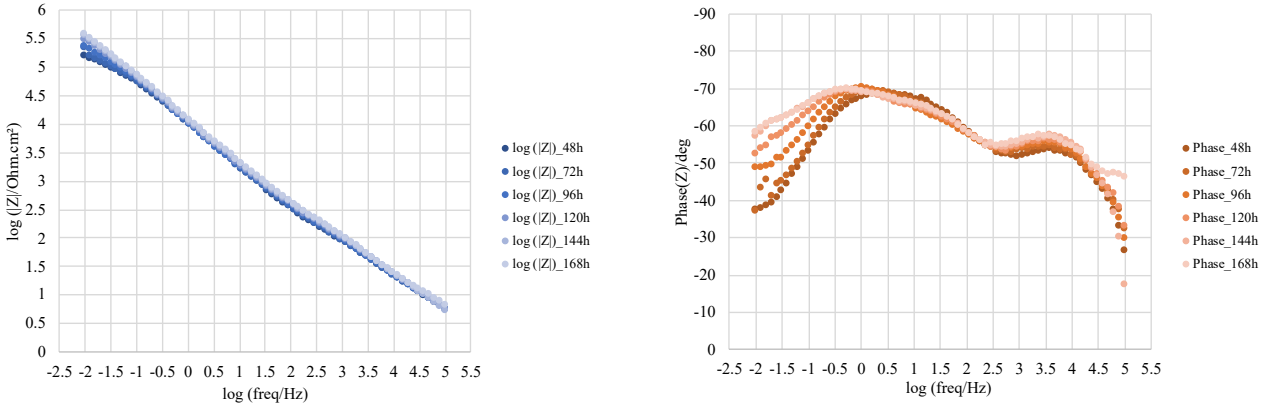


(b) Bode plot of model coating containing $Li_2CO_3$

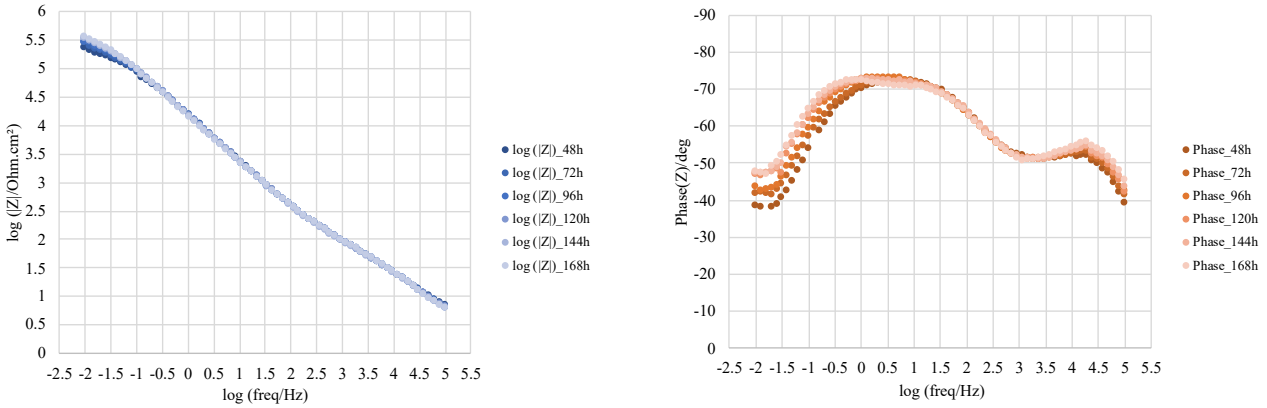


(c) Bode plot of XP420

Figure 29: Electrochemical impedance spectra of AA2024-T3 aluminum alloy of first 168 hours exposure to the 0.1 M NaCl solution without NSS before the electrochemical experiment. Impedance modulus and phase angle plot of (a) Model coating; (b) Model coating containing $Li_2CO_3$; (c) XP420; Label key: as time goes on, the color changes from dark to light

### 3.1.4 Morphology observations

#### 3.1.4.1 Surface morphology

Figure 30 shows the surface morphology of the scribed area for the specimens with and without inhibitor. The specimens experienced 1 week NSS prior the acceleration test in 0.1M NaCl for 168 hours. The corrosion inhibiting effect of the coatings loaded with $Li_2CO_3$ as leaching corrosion inhibitor is clearly visible after 1 week of NSS. Both Figure 30a and e show the porous texture with randomly oriented fine flakes. The protective properties of the Li-based conversion layers originate from the Li-aluminium-hydroxide-carbonate-hydrate layer (layered double hydroxide - LDH) generated on the aluminium alloy [54]. Figure 30c shows that model coating containing $Li_2CO_3$ has texture with different porosity. The model coating containing $Li_2CO_3$ has a denser layer formed than that of model coating and XP420 after 168 hours exposure to NSS. For these three specimens, the scribed lines are clearly visible which suggest that the thickness of layers are relatively small.

In addition, due to the charging effect, BES images were used to illustrate the morphology after the acceleration test. As shown in Figure 30b and d, voluminous flakes gather together to form round shape which represents the formation of aluminum oxide. During the EDS analysis as shown in Table 8 which focus on the points of flakes before the test and round particles after the test, it clearly shows that the both atomic concentrations of oxygen increases significantly and vice versa for aluminum for $Li_2CO_3$-loaded coatings. It indicates the increase content of oxides after the test. XP420 (Figure 30f shows the similar behavior but in detail. It does not exhibit the flakes but the accumulated particles which can be associated to the corrosion products.

| **Type of coating** | **Before/After experiment** | **C** | O | **Al** | Cu |
|---|---|---|---|---|---|
| Model coating | Before | 8.72 | 46.96 | 39.69 | 2.23 |
| | After | 6.28 | 59.69 | 15.86 | 2.49 |
| Model coating containing $Li_2CO_3$ | Before | 8.93 | 23.85 | 61.92 | 2.9 |
| | After | 6.38 | 56.77 | 23.71 | 2.68 |
| XP420 | Before | 6.79 | 27.93 | 72.07 | - |
| | After | 13.45 | 52.14 | 29.52 | - |

Table 8: EDS elemental atomic concentrations of AA2024-T3 before and after the acceleration test

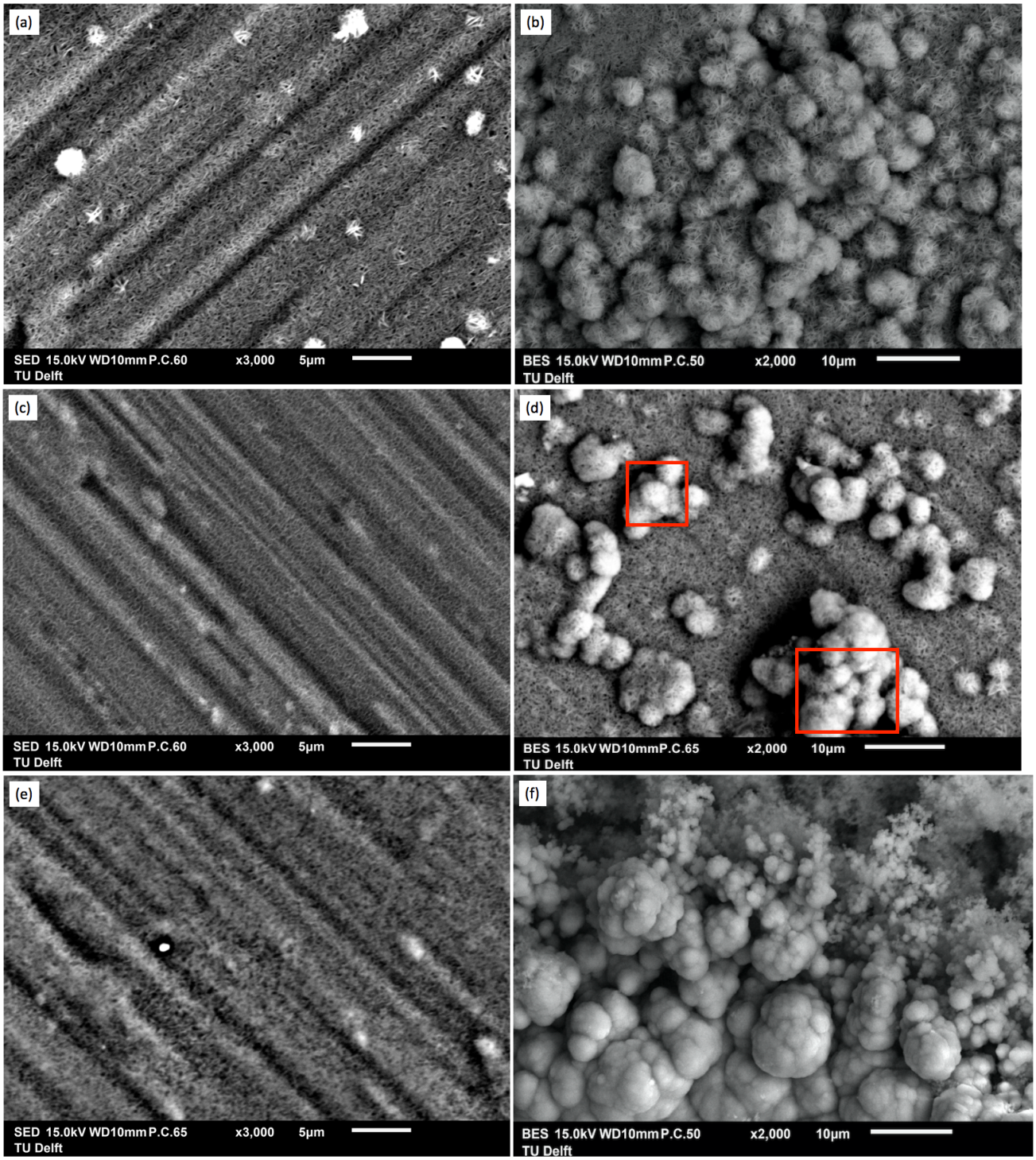


Figure 30: Top-view of the scribed area of AA2024-T3 with 1-week NSS in advance before and after the immersion in 0.1 M NaCl for 168 hours: Scanning electron micrographs of (a) Model coating before experiment; (b) Model coating after experiment; (c) Model coating containing $Li_2CO_3$ before experiment; (d) Model coating containing $Li_2CO_3$ after experiment; (e)XP420 before experiment; (f) XP420 after experiment

#### 3.1.4.2 Morphology of cross section

Figure 31, 32 and 33 show the cross section of the scribe of AA2024-T3 with model coating, model coating containing $Li_2CO_3$ and XP420 experienced 1-week NSS prior to the immersion in 0.1M NaCl for 168 hours. It is obviously that from Figure 31b and 31c, the layer is thinned after 168 hours of experiment which corresponds to the oxide thinning of model coating. As for model coating containing $Li_2CO_3$, it is difficult to identify the reduction in thickness of protective layer, but the fading of grey color and the less uniformity can be observed by the comparison between the Figure 32b and 32c which can be related to the inhibition effect of protective layer against corrosion. This phenomenon is more significant for XP420, the color of grey is becoming more transparent after 168 hours of experiment. According to the Table 9, it can be seen that the percentage decrease in order of model coating containing $Li_2CO_3 \gg$ XP420 > model coating.

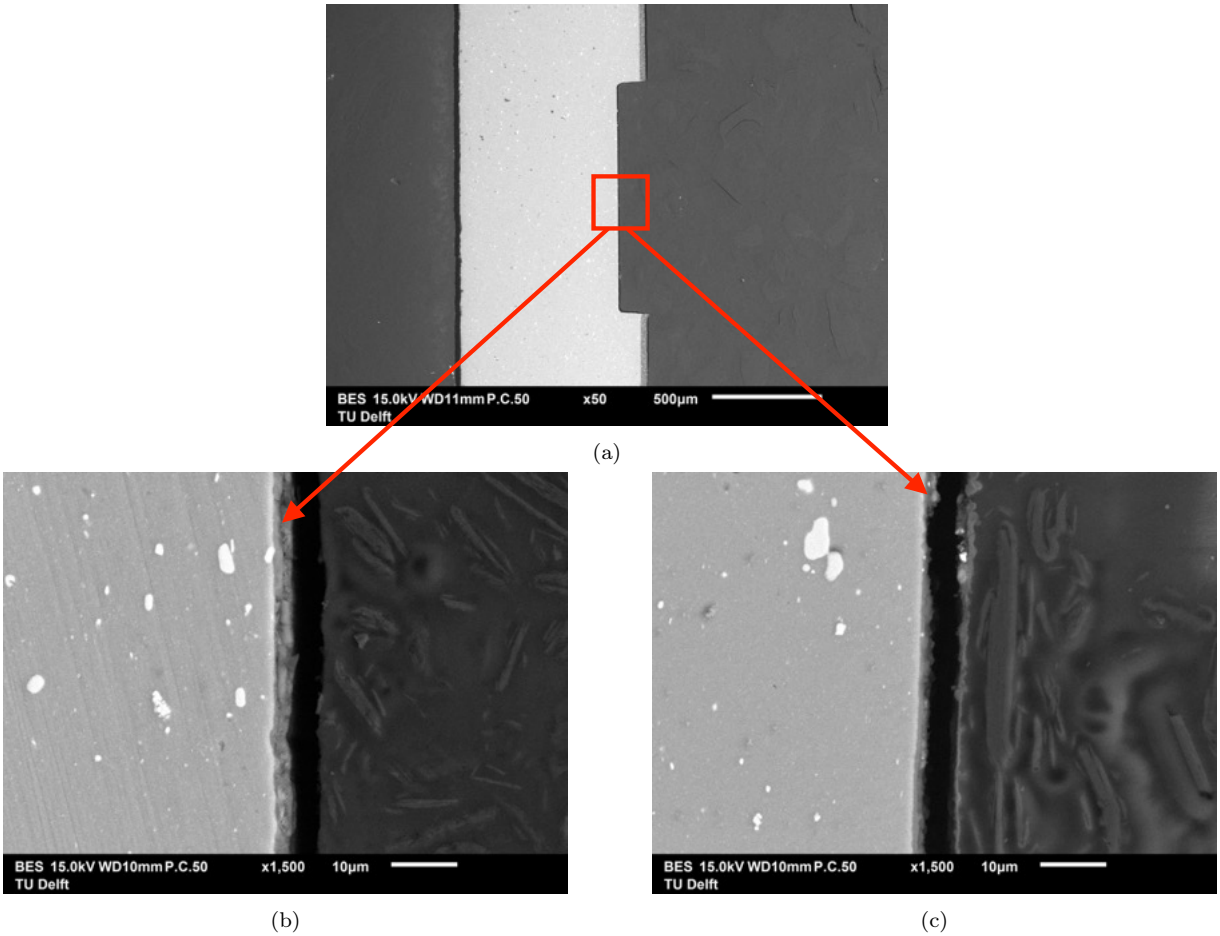


(a) (b) (c)

Figure 31: Cross section of the scribed area of AA2024-T3 with model coating with 1-week NSS in advance before and after the immersion in 0.1 M NaCl for 168 hours: Backscattered electron imaging of (a) Scribed area in 50X magnification; (b) Scribed area in 1500X magnification before the experiment; (c) Scribed area in 1500X magnification After the experiment

| Type of coating | Before/After experiment | Thickness of layer | | Percentage decrease (%) |
|---|---|---|---|---|
| | | Average ($\mu$ m) | Standard deviation | |
| Model coating | Before | 2.70 | 0.21 | 40.74 |
| | After | 1.60 | 0.40 | |
| Model coating containing $Li_2CO_3$ | Before | 1.43 | 0.10 | 12.59 |
| | After | 1.25 | 0.12 | |
| XP420 | Before | 2.12 | 0.33 | 26.42 |
| | After | 1.56 | 0.37 | |

Table 9: The thickness of AA2024-T3 before and after experiment

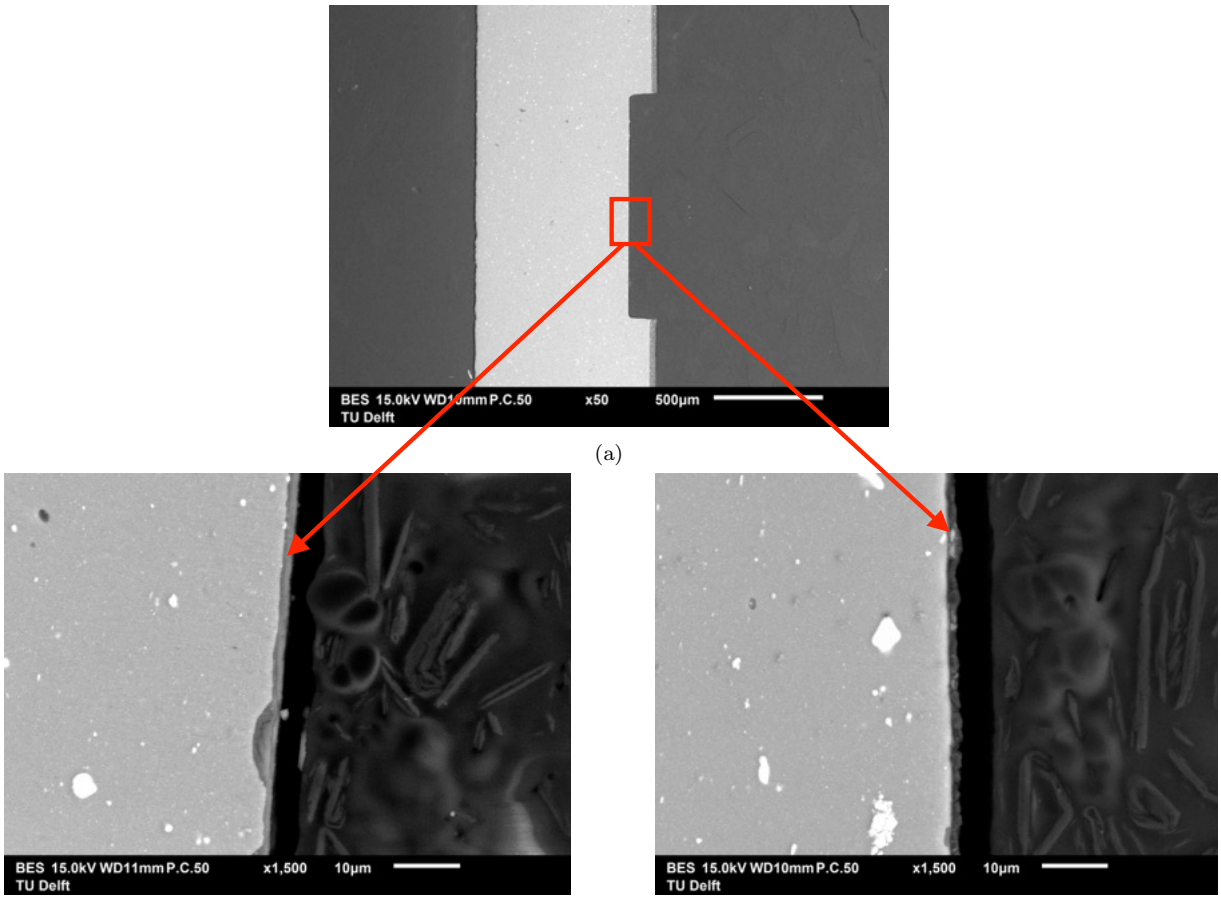


(a)

(b)

(c)

Figure 32: Cross section of the scribed area of AA2024-T3 with model coating containing $Li_2CO_3$ with 1-week NSS in advance before and after the immersion in 0.1 M NaCl for 168 hours: Backscattered electron imaging of (a) Scribed area in 50X magnification; (b) Scribed area in 1500X magnification before the experiment; (c) Scribed area in 1500X magnification after the experiment

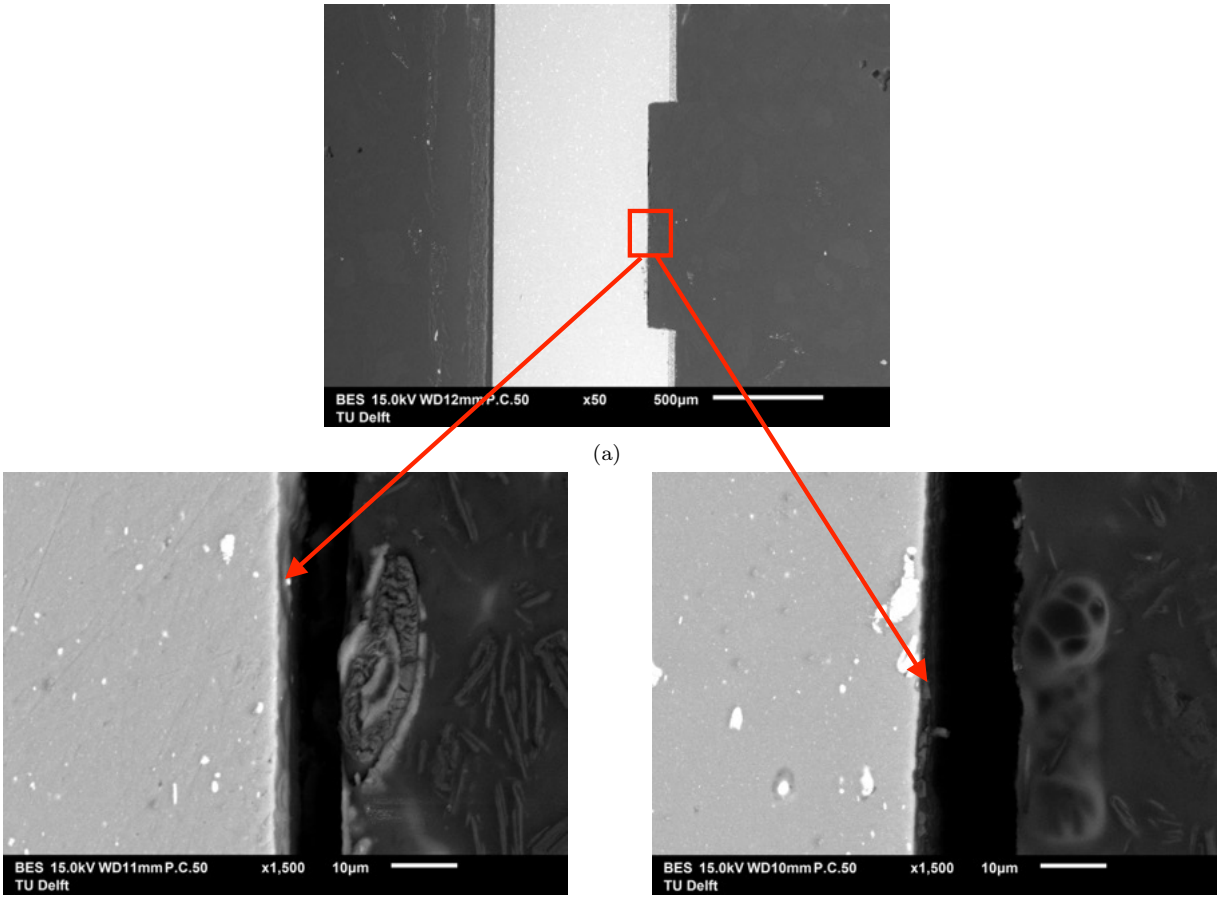


Figure 33: Cross section of the scribed area AA2024-T3 with XP420 with 1-week NSS in advance before and after the immersion in 0.1 M NaCl for 168 hours: Backscattered electron imaging of (a) Scribed area in 50X magnification; (b) Scribed area in 1500X magnification before the experiment; (c) Scribed area in 1500X magnification after the experiment

## 3.2 System AA198-T8

### 3.2.1 Formation of protective layer (No NSS)

#### 3.2.1.1 Electrochemical Characterization

#### OCP

Figure 34 demonstrates the open circuit potential evolution as function of time of different coatings applied on AA2198-T8 aluminum alloy in the presence of 5mL 0.1M NaCl where the effect of different coatings on the formation and corrosion resistivity of the formed layer is investigated.

It can be seen that the model coating containing $Li_2CO_3$ has two plateaus. After the initial rapid reduction to around -1.25V vs Ag/AgCl, it has a first increase in potential to a plateau

at approximately -1.05V vs Ag/AgCl which is related to the layer formation. Then, a second potential increase is observed which is associated with the competitive growth and dissolution of protective layer. A faster evolution over the stages of layer formed is observed in XP420 since it approaches the stable level after approximately 20 minutes exposure to the electrolyte. Overall, XP420 reaches stable level firstly after the initial drop to around -0.95V vs Ag/AgCl, then the model coating containing $Li_2CO_3$, it verifies that corrosion protection is offered by applying the $Li_2CO_3$-loaded coating.

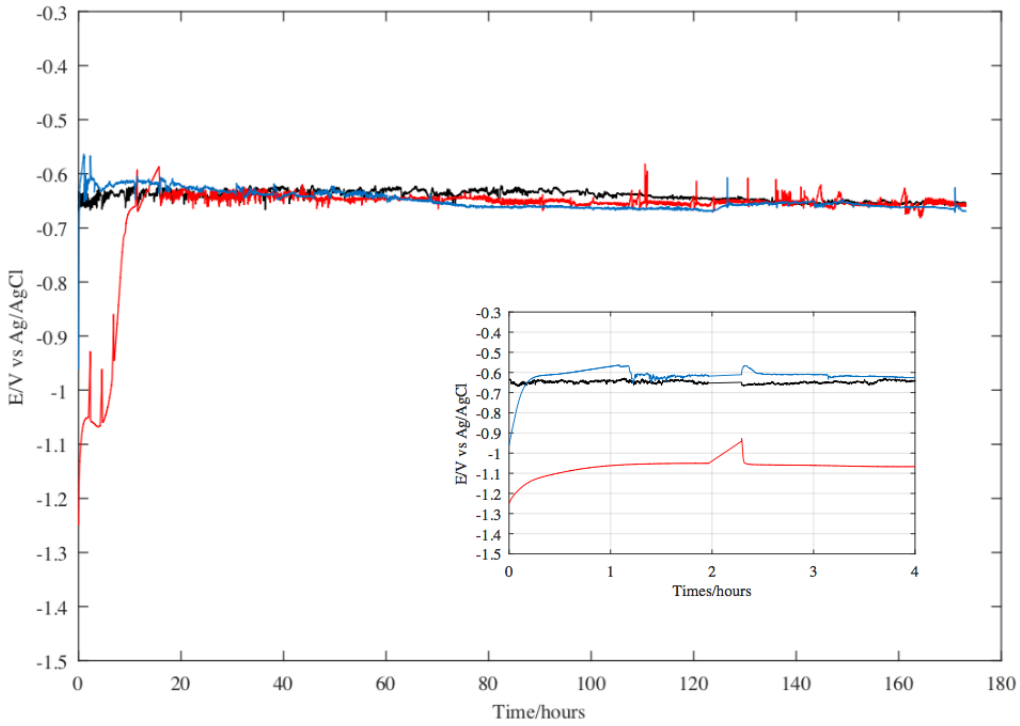


Figure 34: Open circuit potential response over time of AA2198-T8 exposed to 0.1M NaCl solution. Label key: (black) Model coating, (red) Model coating containing $Li_2CO_3$, (blue) XP420

**LPR**

The LPR of AA2198-T8 is studied as shown in Figure 35. Figure 35 describes the resistance polarization evolution as a function of time of AA2198-T8 aluminum alloy immersed in 5ml 0.1M NaCl solution. From Figure 35b It can be seen that the resistance polarization of model coating keep decreasing over 168 hours of experiment. Though model coating shows the higher polarization resistance for the first several hours, the model coating containing $Li_2CO_3$ has larger resistance polarization than that of model coating. As for XP420, it has a relatively stable level of resistance polarization since it is in the range of 5-15 $k\Omega.cm^2$. However, it should be noted that the all values of resistance polarization for samples in this scenario are much lower than expected if we compare them with other results from the same system AA2198-T8 and another system AA2024-T8. The assumption that the scribed area

measured for the calculation of resistance polarization is not the active area. The details and reasons behind this assumption would be further discussed in the following section. It is also noted that the area used in calculation of resistance polarzation for AA2198-T8 in this experiment without NSS is the area of scribe.

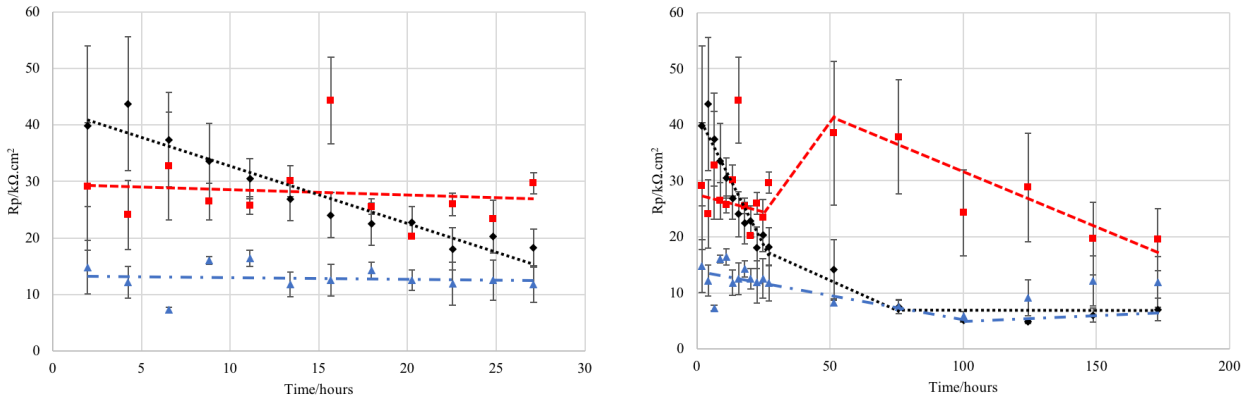


(a) First 24 hours of AA2198-T8 without NSS

(b) 168 hours of AA2198-T8 without NSS

Figure 35: Resistance polarization ($R_p$) evolution as a function of time of AA2198-T8 aluminum alloy immersed in 5ml 0.1M NaCl solution of (a)24 hours without NSS; (b) 168 hours without NSS. Label key: (black) model coating, (red) model coating containing $Li_2CO_3$, (blue) XP420

### EIS

Electrochemical impedance spectra of samples AA2198-T8 without NSS were recorded after LPR as a function of frequency which are presented in Figure 40a and Figure 40b. The graphs of EIS describe changes in impedance modulus and phase angle over time by the fading of color. It has to be noted that the area used in the EIS measurements is the area of the base of the container used during the experiment setup which is 10.18 $cm^2$. Therefore, the resistance polarization obtained from impedance modulus from EIS is not corresponding to the values obtained from LPR.

In figure 40a, only the bode plot of the impedance modulus of model coating containing $Li_2CO_3$ (Figure 36b shows an increase of impedance values in the middle frequency ($10^1$-$10^3$ Hz) and approximately one order in low frequency ($10^-1$-$10^-2$ Hz) ranges compared to the model coating and XP420. This increase of the impedance modulus in the middle frequency range can be associated with the formation of an (oxide) layer in the damaged area. The increase of the impedance modulus at low frequencies can be associated with the increased corrosion resistance of the layers generated from the lithium-leaching coatings. However, after the 24 hours, the bode plot of impedance modulus of model coating containing $Li_2CO_3$ shows the opposite results which can be associated with the break down of the protective layer. The accompanying phase angle plots of these measurements over the first 24 hours

show a broadening of the phase angle around $10^1$ – $10^3$ Hz as a result of the generated layer in the defect area. It can be noted that this phase angle peak has an asymmetric shape and shows a shoulder in the higher frequency area around $10^{1.5}$ to $10^3$ Hz. This asymmetry suggests that there are possibly two overlapping time-constants in this frequency range [53].

It is important to note that after 24 hours, the model coating reaches the highest value of 870 $k\Omega.cm^2$, which is higher than other two samples. It may indicate that the lithium is leaching from the AA2198-T8 aluminum alloy and resulted in the formation of protective layer.

The XP420 shows a totally opposite trend as we saw in model coating containing $Li_2CO_3$. For the first 24 hours, the bode plot of impedance modulus decrease continuously with the narrowed shape of phase angle. However, it shows an increase about one order and broadened shape of phase angle for the following days. The reason behind it may be the extension time for the oxide thinning.

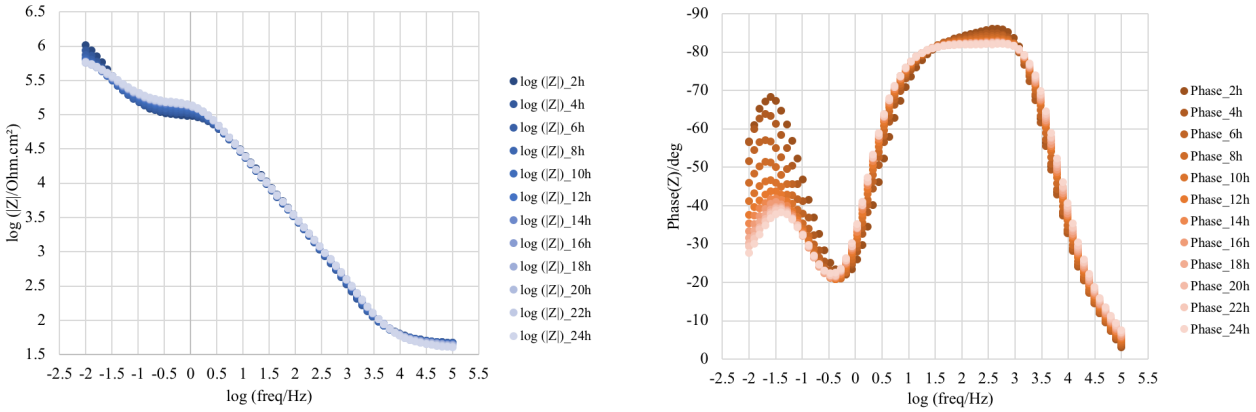


(a) Bode plot of model coating

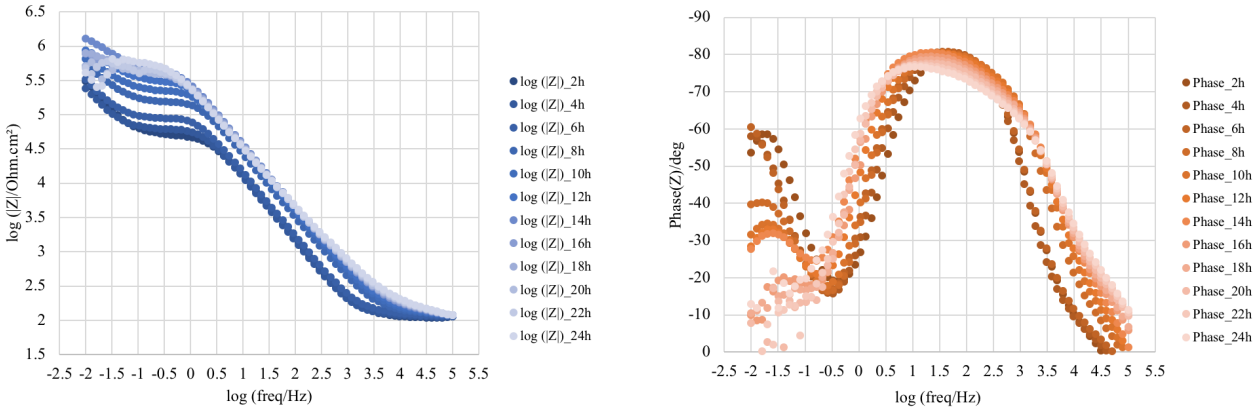


(b) Bode plot of model coating containing $Li_2CO_3$

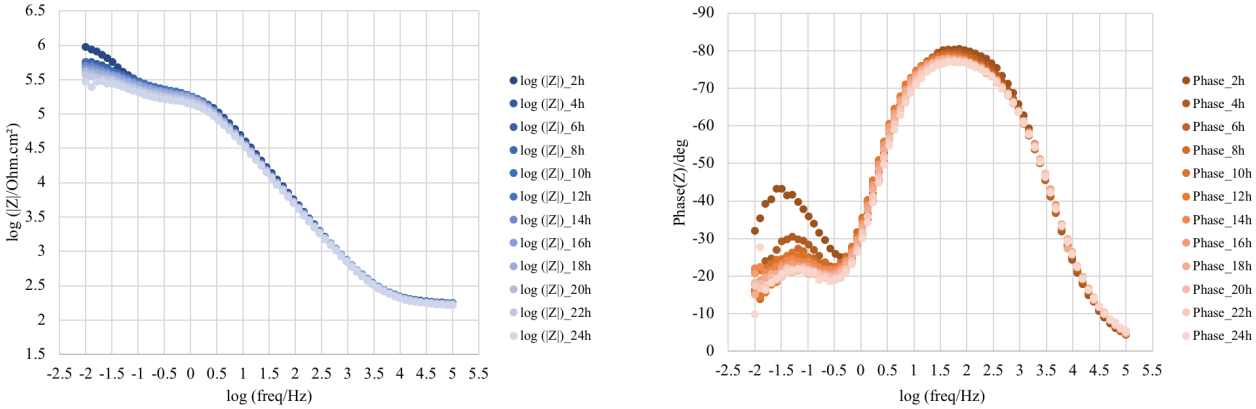


(c) Bode plot of XP420

Figure 36: Electrochemical impedance spectra of AA2198-T8 aluminum alloy of first 24 hours exposure to the 0.1 M NaCl solution without NSS before the electrochemical experiment. Impedance modulus and phase angle plot of (a) Model coating; (b) Model coating containing $Li_2CO_3$; (c) XP420; Label key: as time goes on, the color changes from dark to light

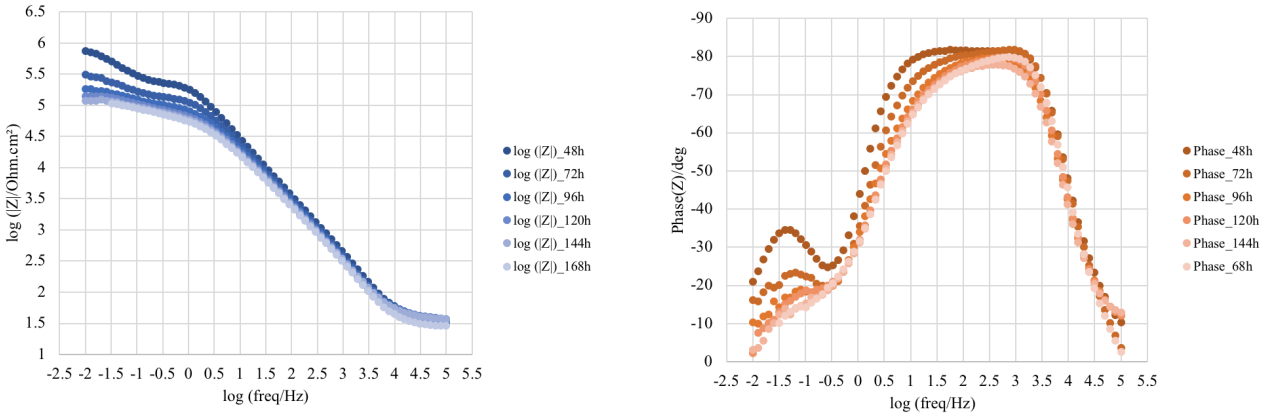


(a) Bode plot of model coating

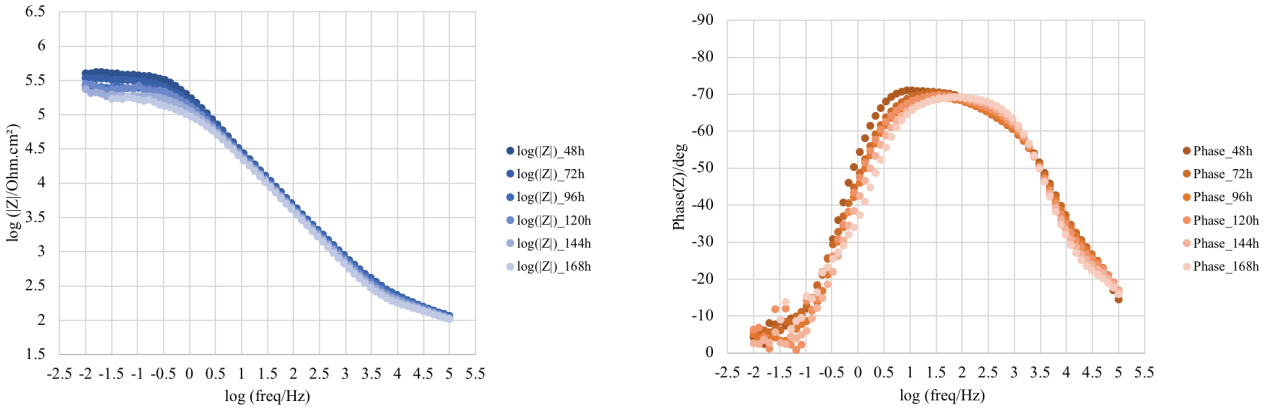


(b) Bode plot of model coating containing $Li_2CO_3$

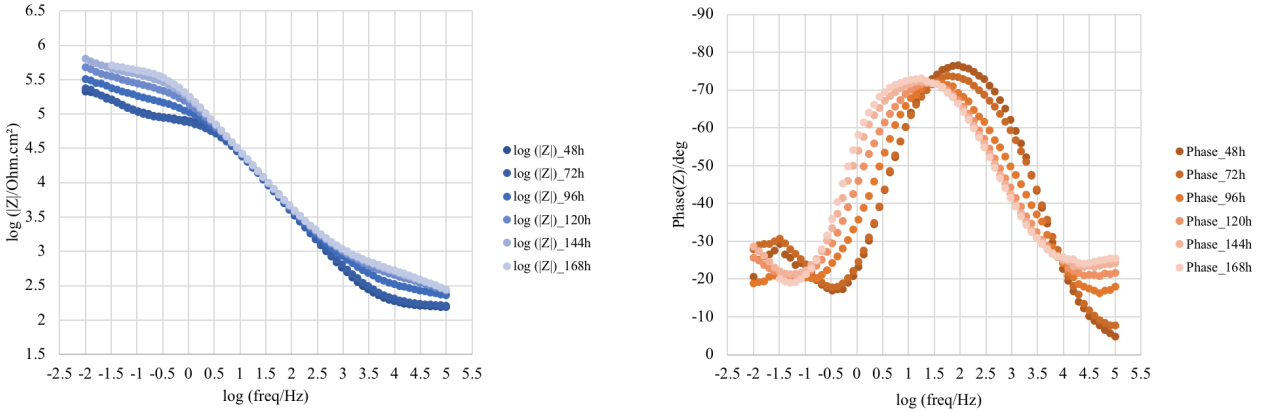


(c) Bode plot of XP420

Figure 37: Electrochemical impedance spectra of AA2198-T8 aluminum alloy of first 24 hours exposure to the 0.1 M NaCl solution without NSS before the electrochemical experiment. Impedance modulus and phase angle plot of (a) Model coating; (b) Model coating containing $Li_2CO_3$; (c) XP420; Label key: as time goes on, the color changes from dark to light

### 3.2.2 Morphology observations

#### 3.2.2.1 Morphology of cross section

In order to investigate the detailed morphology of cross section of three types of coating, SEM was used after the immersion in 0.1M NaCl without NSS for 168 hours of experiments as shown in Figure 38. It can be seen that model coating containing $Li_2CO_3$ has overwhelming thicker protective layer than other two samples. It explains the significant increase about one order of impedance modulus observed from EIS. Other than that, it is difficult to distinguish the discrepancy between model coating and XP420 from Figure 38a and f and there is not much difference in thickness as shown in Table 10. By the observation from the results from EIS (Figure 37a and 37c), it is possible to assume that protective layer of XP420 is still evolving. And at the same time, it is possible that lithium leaching from the aluminum alloys of XP420 and form protective layer.

Also, it is important to note that there is a gap between the coating layer and the base metal as shown in Figure 38a and e. The delamination of coating detached from the base metal may be the main reason behind the overall low values of resistance polarization observed in LPR analysis. Further explanation is discussed in the discussion section.

| **Type of coating** | **Thickness of layer** | |
|---|---|---|
| | **Average ($\mu$m)** | **Standard deviation** |
| Model coating | 2.40 | 0.80 |
| Model coating containing $Li_2CO_3$ | 5.83 | 0.50 |
| XP420 | 2.03 | 0.78 |

Table 10: The thickness of layer of AA2198-T8 without NSS after experiment

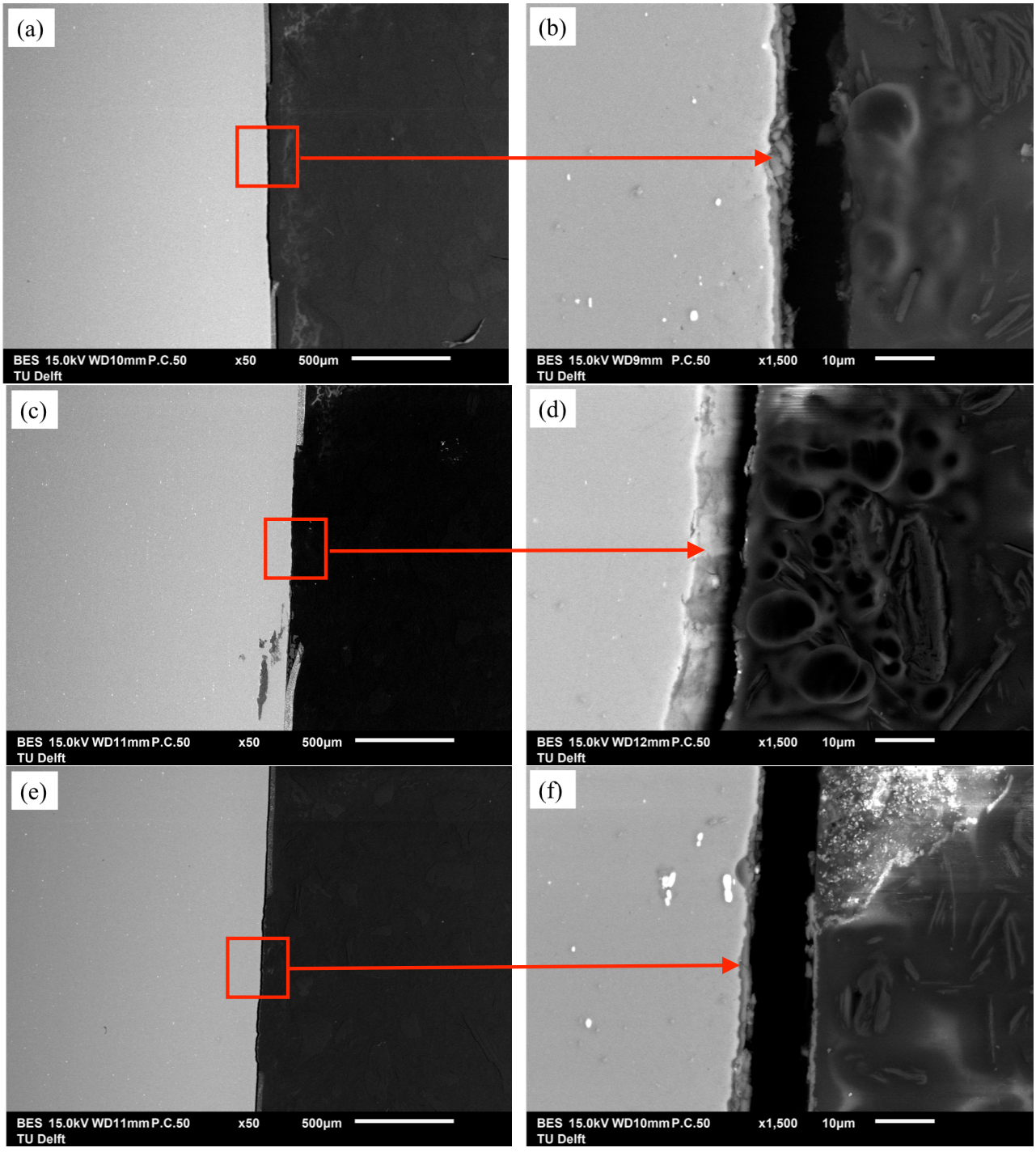


Figure 38: Cross section of the scribed area of AA2198-T8 without 1-week NSS in advance after the immersion in 0.1 M NaCl for 168 hours: Backscattered electron images of (a) Model coating in 50X magnification; (b) Model coating in 1500X magnification; (c) Model coating containing $Li_2CO_3$ in 50X magnification; (d) Model coating containing $Li_2CO_3$ in 1500X magnification ; (e) XP420 in 50X magnification; (f) XP420 in 1500X magnification

### 3.2.3 Stability of protective layer (with NSS)

#### 3.2.3.1 Electrochemical Characterization

**OCP**

In the scenario of the AA2198-T8 which has been immersed in NSS for one week before the electrochemical experiment (Figure 39), model coating and XP420 are at the stable level at approximately -0.65V vs Ag/AgCl due to the protective layer formed during NSS. Model coating containing $Li_2CO_3$ shows a decrease in potential at the beginning which demonstrates that the layer is still in the progress of formation. After around 1.3 hours, OCP of model coating containing $Li_2CO_3$ reaches a stable state after around 1.3 hours which can be associated to the complete formation of protective layer.

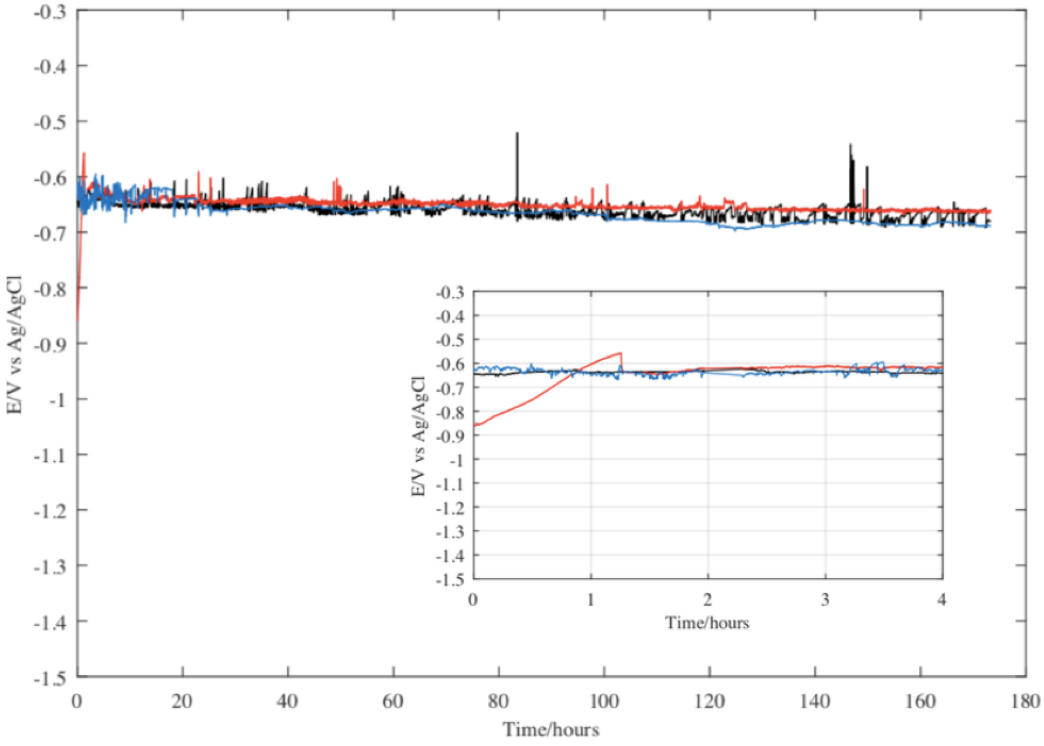


Figure 39: Open circuit potential response over time of AA2198-T8 exposed to 0.1M NaCl solution. The samples have been in 1-week NSS before test. Label key: (black) Model coating, (red) Model coating containing $Li_2CO_3$, (blue) XP420

**LPR**

Resistance polarization recordings of AA2198-T8 with 1-week in advance were made at 2-hour time interval for the first 24 hours and 24-hour time interval for the rest of time and are

presented as a function of time in Figure 40a and Figure 40b immersed in 0.1M NaCl. It can be seen taht the initial resistance polarization of $Li_2CO_3$-loaded coating is larger than that of model coating. Apart from that, the most important point of this two figures is that the resistance polarization of XP420 behave totally different from other two kinds of samples. Firstly, the values of resistance polarization are much larger than other two specimens. Secondly, through the different phases over time, after an slightly initial decrease in resistance polarization which contributes to the local corrosion points, the values starts to increase until a plateau is reached. Then, it has a decrease trend and finally another plateau is reached. As for other two specimens, the trend is relatively stable compared with the model coating containing $Li_2CO_3$.

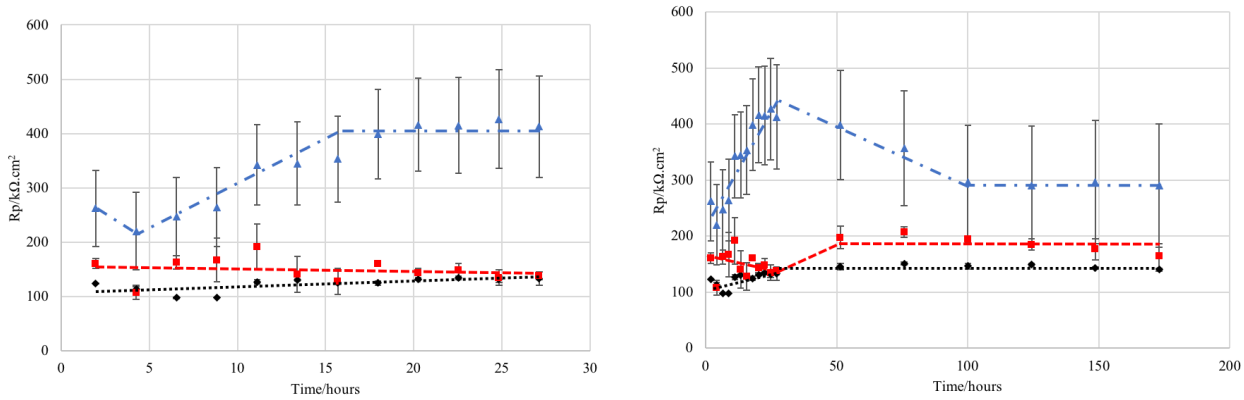


(a) First 24 hours of AA2198-T8 with NSS

(b) 168 hours of AA2198-T8 with NSS

Figure 40: Resistance polarization ($R_p$) evolution as a function of time of AA2198-T8 aluminum alloy immersed in 5ml 0.1M NaCl solution of (a) 24 hours with NSS; (b) 168 hours with NSS Label key: (black) model coating, (red) model coating containing $Li_2CO_3$, (blue) XP420

**EIS**

The EIS measurements during samples of AA2198-T8 with 1-week NSS in advance are able to demonstrate the coating's behaviour through tracking changes in impedance modulus and phase angles as shown in Figure 40a and 42. The bode plots of impedance modulus for all specimens at low frequency range are stable and do not have significant changes in values for the first 24 hours. When considering the bode plots of phase angles for 24 hours, model coating shows the typical two time-constants, one is at the relatively lower frequency range with the increase in values of phase angle which can be associated with the thin oxide layer, the other one shows a decrease in phase angles at relatively higher frequency can be related to the electrochemical activity at the aluminium substrate, this behavior can be explained due to the formation of corrosion products in the defect area. After 24 hours, the Bode phase angle diagram of the model coating shows still two time-constants, and it still exhibit the same phenomenon for the result over time.

As for model coating containing $Li_2CO_3$, after reaching the impedance modulus of approximately $10^{6.5}$ Ohm.cm$^2$, it maintain at this values for the rest of time. When considering the accompanying bode plot of phase angle, three time-constants were found at the beginning of experiment. Figure 36b shows an asymmetric shape and shows a shoulder in the higher frequency area around $10^{-1}$ to $10^{1}$ Hz. This asymmetry suggests that there are possibly two overlapping time-constants in this frequency range [53]. Later, especially after the first 24 hours, it can be seen that the hidden shoulder which can be related to the protective layer starts to disappears gradually with time. This can be associated with the decrease in corrosion protection [34].

The bode plot of impedance modulus as shown in Figure 36c does not show a obvious change. The accompanying phase angle shows three time-constants, one in higher frequency and two overlapping time-constant in the range between $10^{-0.5}$ to $10^{3}$ Hz. For the rest of experiment as shown in Figure 42c, the impedance modulus at the low frequency between $10^{-2}$ to $10^{1}$ Hz shows a significant decrease which can be related to the break down of protective layer.

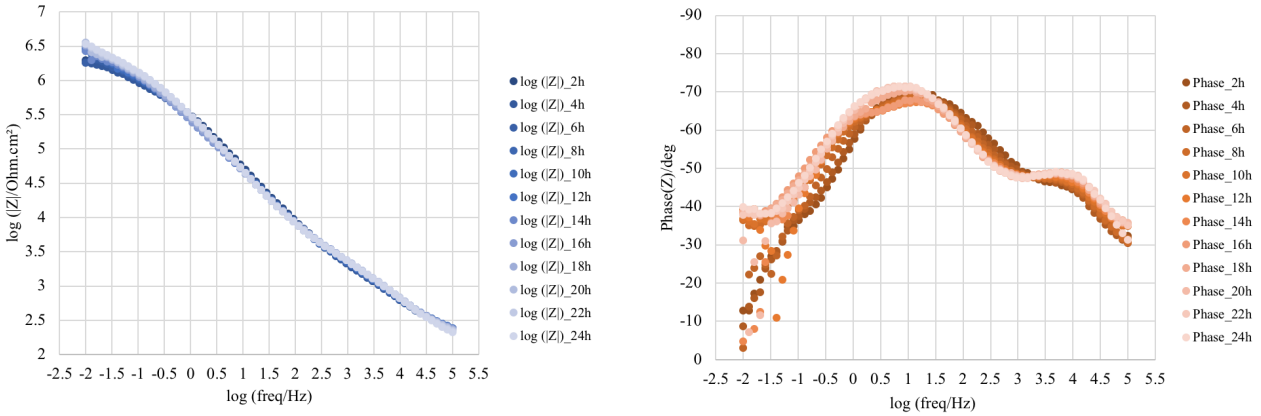


(a) Bode plot of model coating

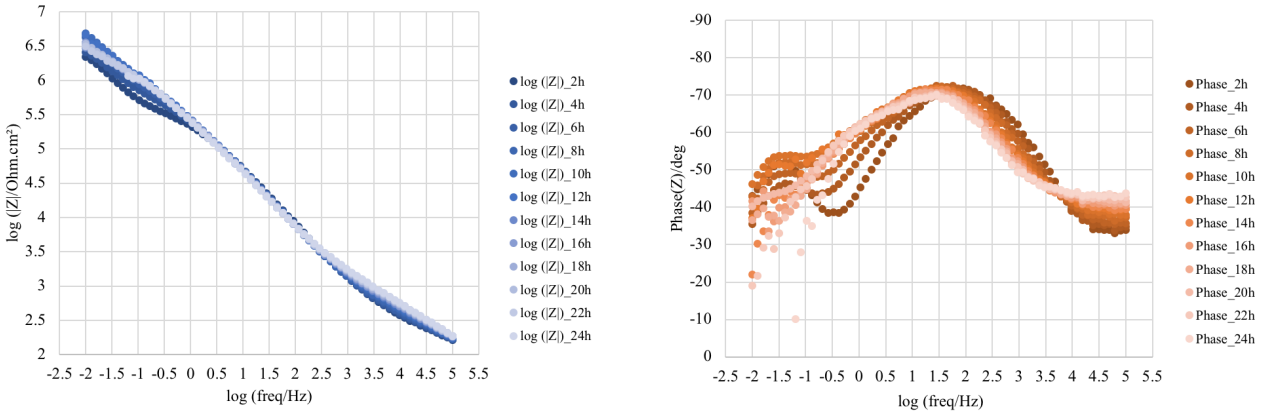


(b) Bode plot of model coating containing $Li_2CO_3$

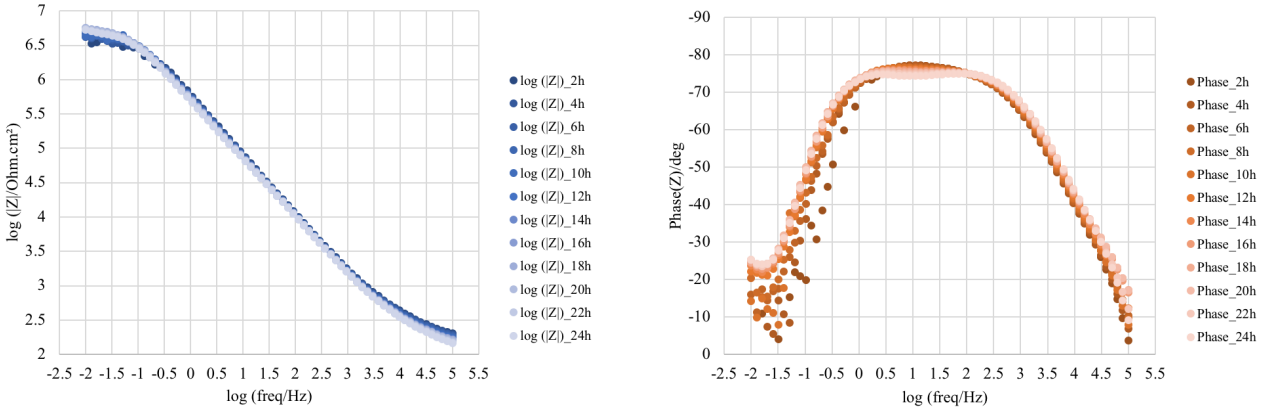


(c) Bode plot of XP420

Figure 41: Electrochemical impedance spectra of AA2198-T8 aluminum alloy of first 24 hours exposure to the 0.1 M NaCl solution without NSS before the electrochemical experiment. Impedance modulus and phase angle plot of (a) Model coating; (b) Model coating containing $Li_2CO_3$; (c) XP420; Label key: as time goes on, the color changes from dark to light

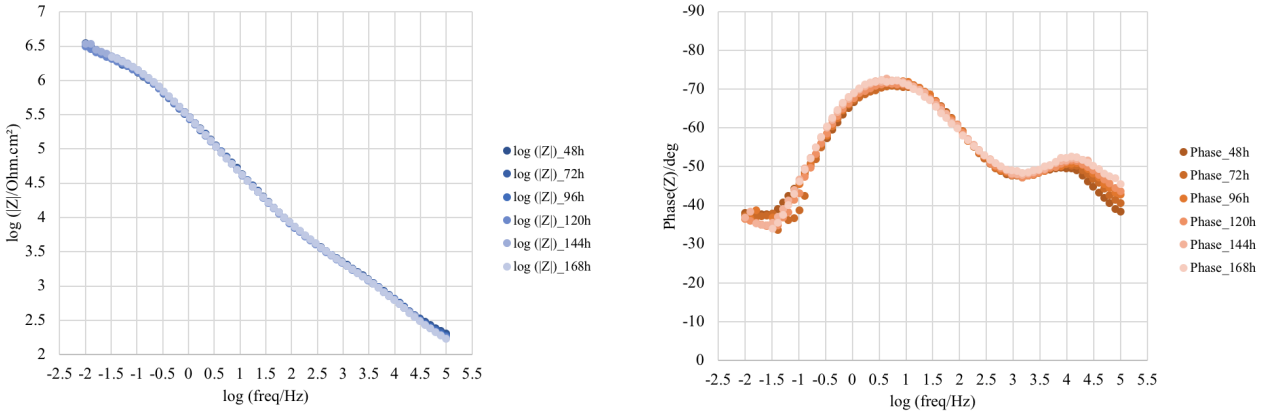


(a) Bode plot of model coating

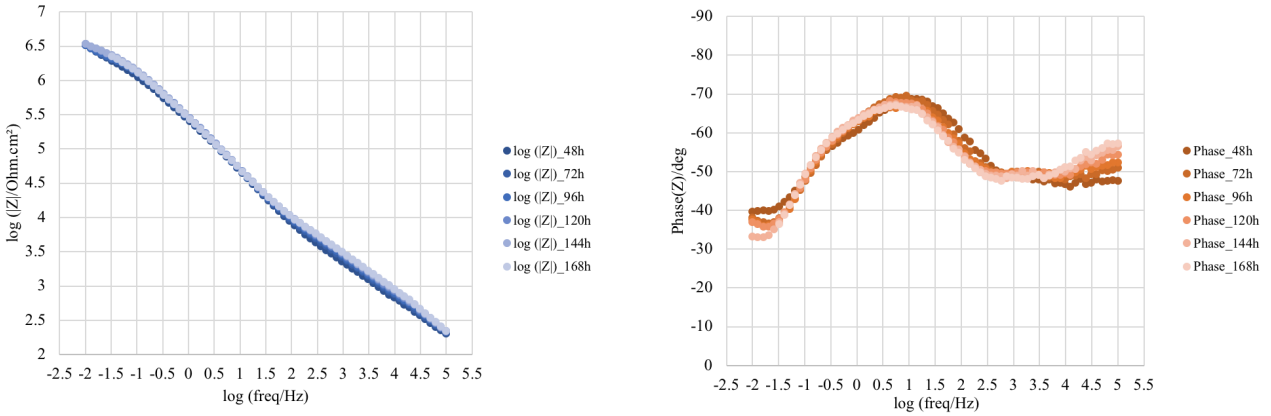


(b) Bode plot of model coating containing $Li_2CO_3$

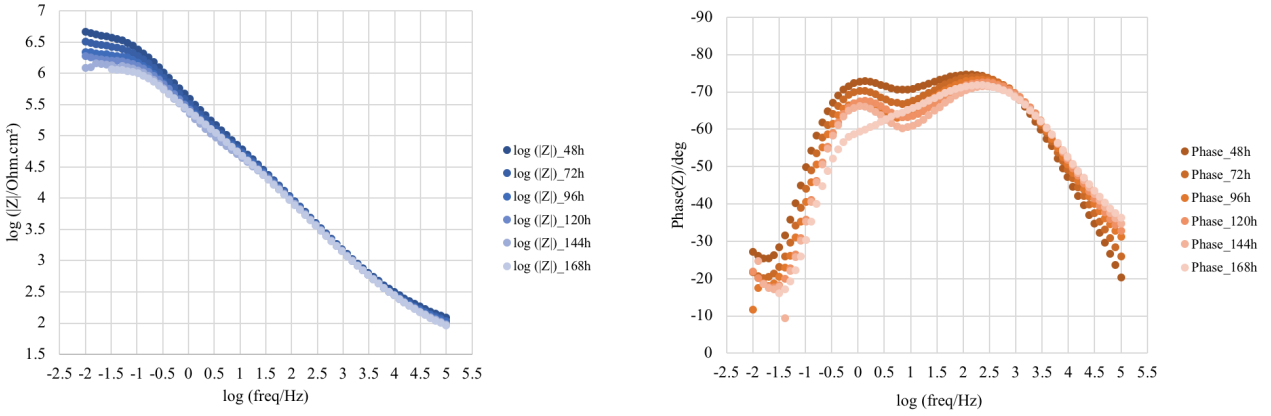


(c) Bode plot of XP420

Figure 42: Electrochemical impedance spectra of AA2198-T8 aluminum alloy of first 24 hours exposure to the 0.1 M NaCl solution without NSS before the electrochemical experiment. Impedance modulus and phase angle plot of (a) Model coating; (b) Model coating containing $Li_2CO_3$; (c) XP420; Label key: as time goes on, the color changes from dark to light

### 3.2.4 Morphology observations

#### 3.2.4.1 Surface morphology

The surface morphology for the protective layer on AA2198-T8 specimens with/without inhibitor formed before and after 168 hours of electrochemical experiment in 0.1M 5ml NaCl electrolyte was investigated and the typical morphology of the Al-Li LDH on AA2198-T8 in Figure 43 was found all specimens before the experiment. Both modal coating (Figure 43a) and model coating containing $Li_2CO_3$ (Figure 43c) shows the porous texture with randomly oriented fine flakes, which demonstrate the formation of hydrated aluminum oxide. Figure 43e shows that XP420 has texture with lower porosity since the more flakes are gathering at the defect area. Thus, the XP420 has a denser layer formed than that of model coating and model coating containing $Li_2CO_3$ before the experiment. After the experiment, as shown in Figure 43b and d, voluminous flakes gather together to form round shape which represents the formation of aluminum oxide.

Figure 43f shows that XP420 has higher porosity which can be associated with the break down of protective layer. The table 11 shows that model coating containing $Li_2CO_3$ has an increase for oxygen and decrease in aluminum in the atomic concentrations which also demonstrates the increase of aluminum oxide.

| | Before/After experiment | C | O | Al | Cu |
|---|---|---|---|---|---|
| Model coating | Before | 4.88 | 51.19 | 28.96 | 1.22 |
| | After | 10.14 | 46.88 | 53.12 | - |
| Model coating containing $Li_2CO_3$ | Before | 12.13 | 22.77 | 61.07 | 1.14 |
| | After | 2.92 | 61.27 | 33.77 | 1.37 |
| XP420 | Before | 5.56 | 46.46 | 44.54 | 2.09 |
| | After | 25.97 | 41.22 | 14.14 | - |

Table 11: EDS elemental atomic concentrations of AA2198-T8 before and after the acceleration test

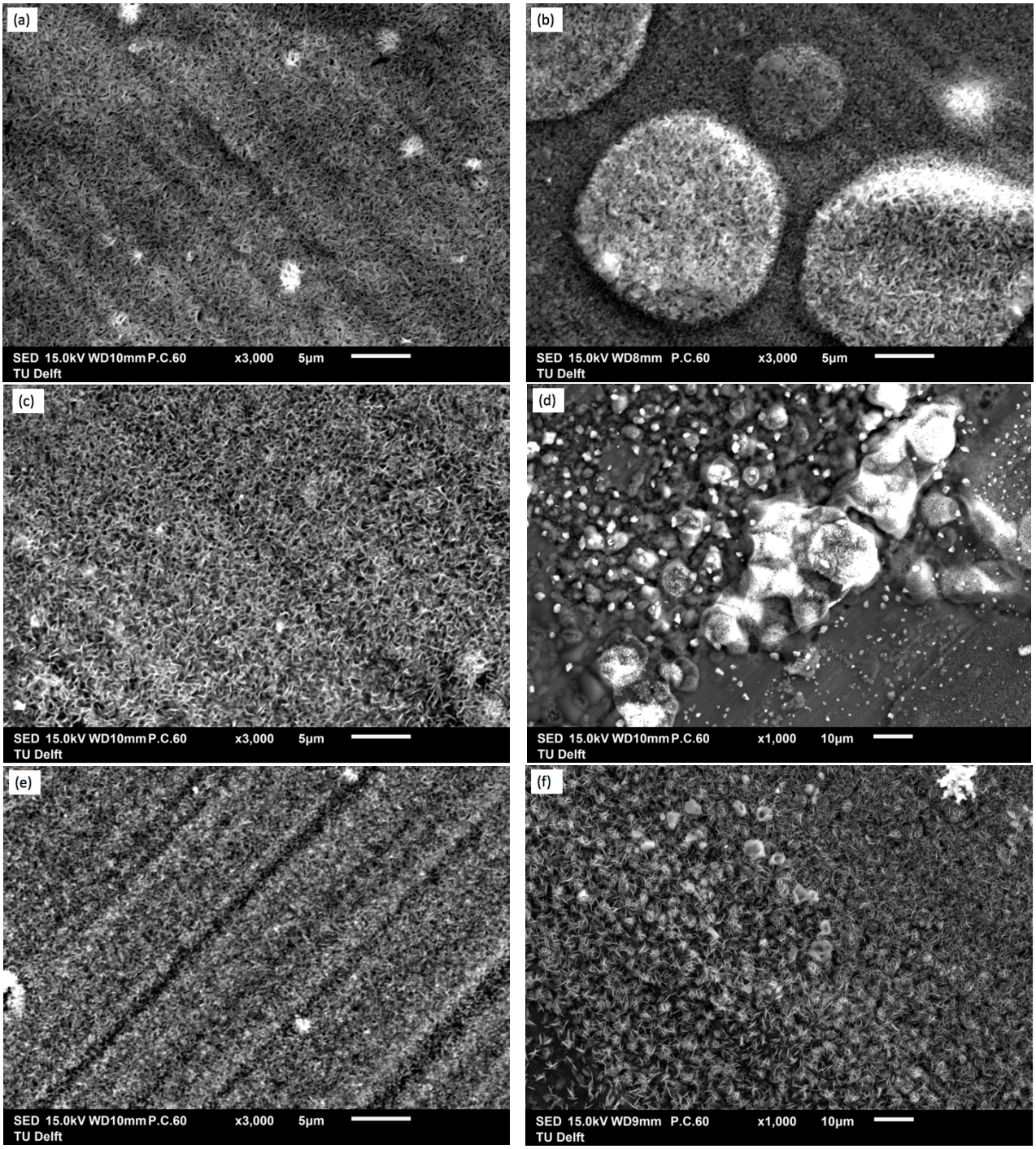


Figure 43: Top-view of the scribed area of AA2198-T8 with 1-week NSS in advance before and after the immersion in 0.1 M NaCl for 168 hours: Scanning electron micrographs of (a) Model coating before experiment; (b) Model coating after experiment; (c) Model coating containing $Li_2CO_3$ before experiment; (d) Model coating containing $Li_2CO_3$ after experiment; (e)XP420 before experiment; (f) XP420 after experiment

#### 3.2.4.2 Morphology of cross section

Figure 44, 45 and 46 show the cross section of the scribe of AA2198-T8 with model coating, model coating containing $Li_2CO_3$ and XP420 experienced 1-week NSS prior to the immersion in 0.1M NaCl for 168 hours. All specimens shows a significant decrease in thickness and the fading of grey color after 168 hours of experiment which corresponds to the oxide thinning of model coating and protective lyaer thinning of model coating containing $Li_2CO_3$ and XP420. According to the Table 12, it can be seen that the percentage decrease in order of XP420 > model coating > model coating containing $Li_2CO_3$. It should be noted from the Figure 45a and 46a that there is delamination between the coating and metal substrate. This observation lead to the possible reason to explain the extremely low values obtained for LPR and it would be discussed in the following section.

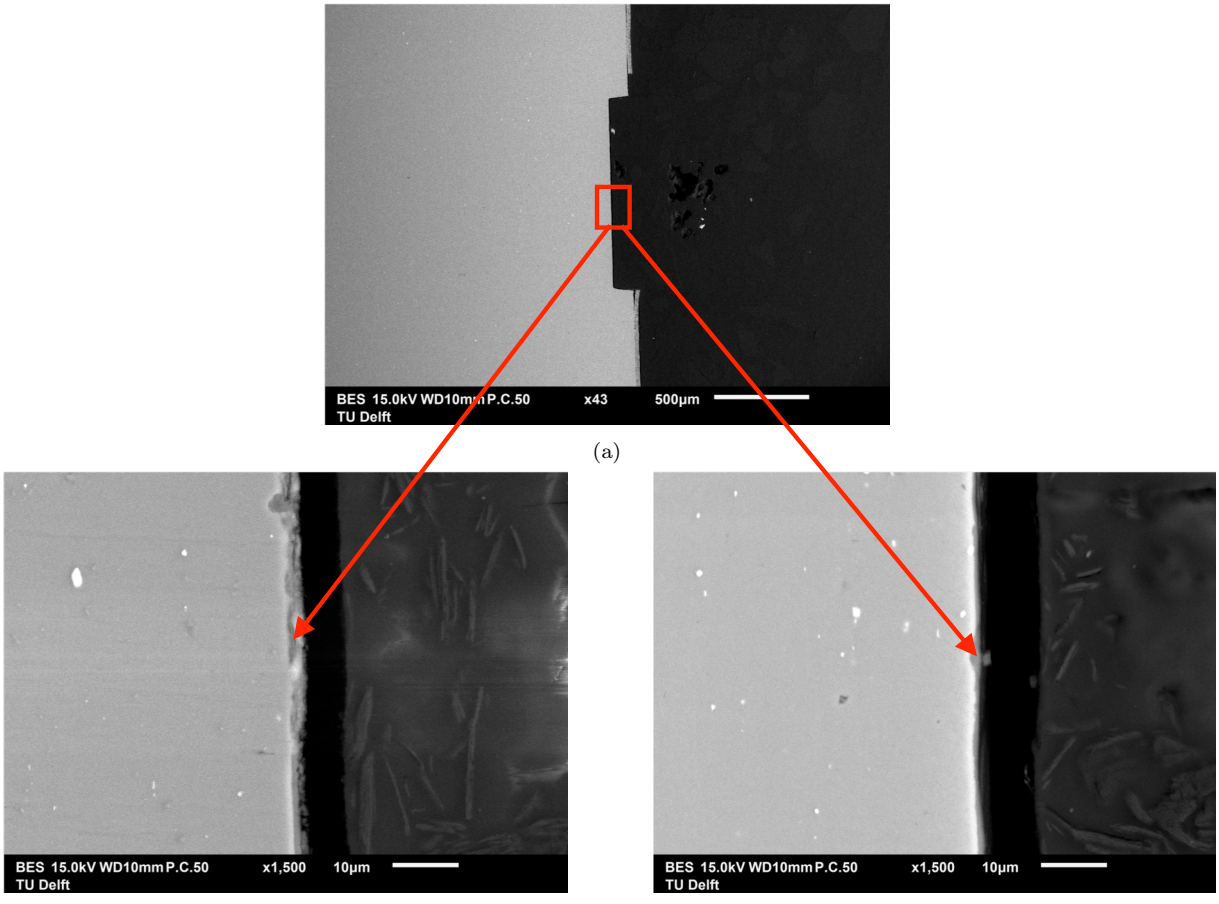


(a)

(b)

(c)

Figure 44: Cross section of the scribed area of AA2198-T8 with model coating with 1-week NSS in advance before and after the immersion in 0.1 M NaCl for 168 hours: Backscattered electron imaging of (a) Scribed area in 50X magnification; (b) Scribed area in 1500X magnification before the experiment; (c) Scribed area in 1500X magnification After the experiment

| Type of coating | Before/After experiment | Thickness of layer | | Percentage decrease (%) |
|---|---|---|---|---|
| | | Average ($\mu$m) | Standard deviation | |
| Model coating | Before | 2.23 | 0.38 | 56.95 |
| | After | 0.96 | 0.25 | |
| Model coating containing $Li_2CO_3$ | Before | 1.59 | 0.28 | 3.77 |
| | After | 1.53 | 0.36 | |
| XP420 | Before | 2.80 | 0.40 | 75.71 |
| | After | 0.68 | 0.19 | |

Table 12: The thickness of AA2198-T8 with NSS before and after experiment

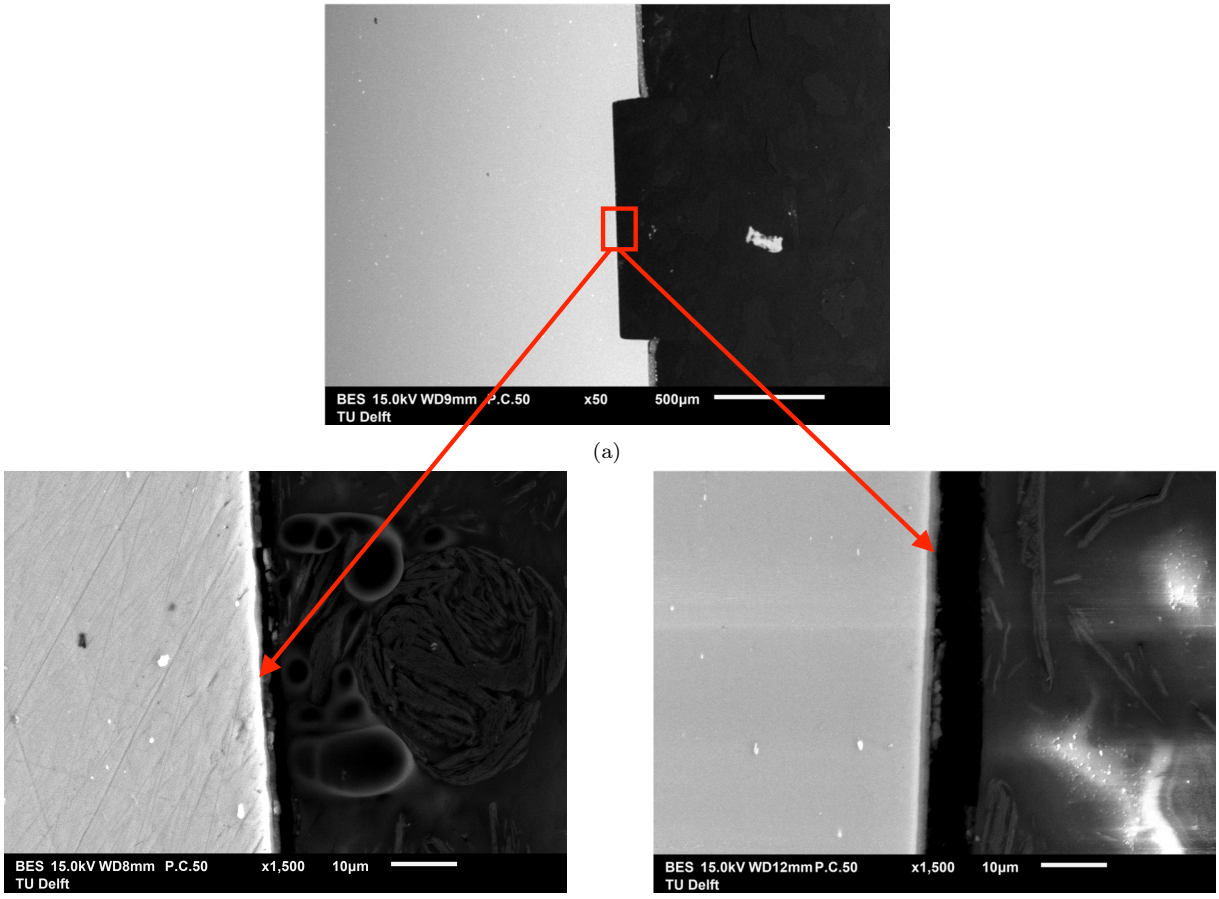


(a)

(b)

(c)

Figure 45: Cross section of the scribed area of AA2198-T8 with model coating containing $Li_2CO_3$ with 1-week NSS in advance before and after the immersion in 0.1 M NaCl for 168 hours: Backscattered electron imaging of (a) Scribed area in 50X magnification; (b) Scribed area in 1500X magnification before the experiment; (c) Scribed area in 1500X magnification after the experiment

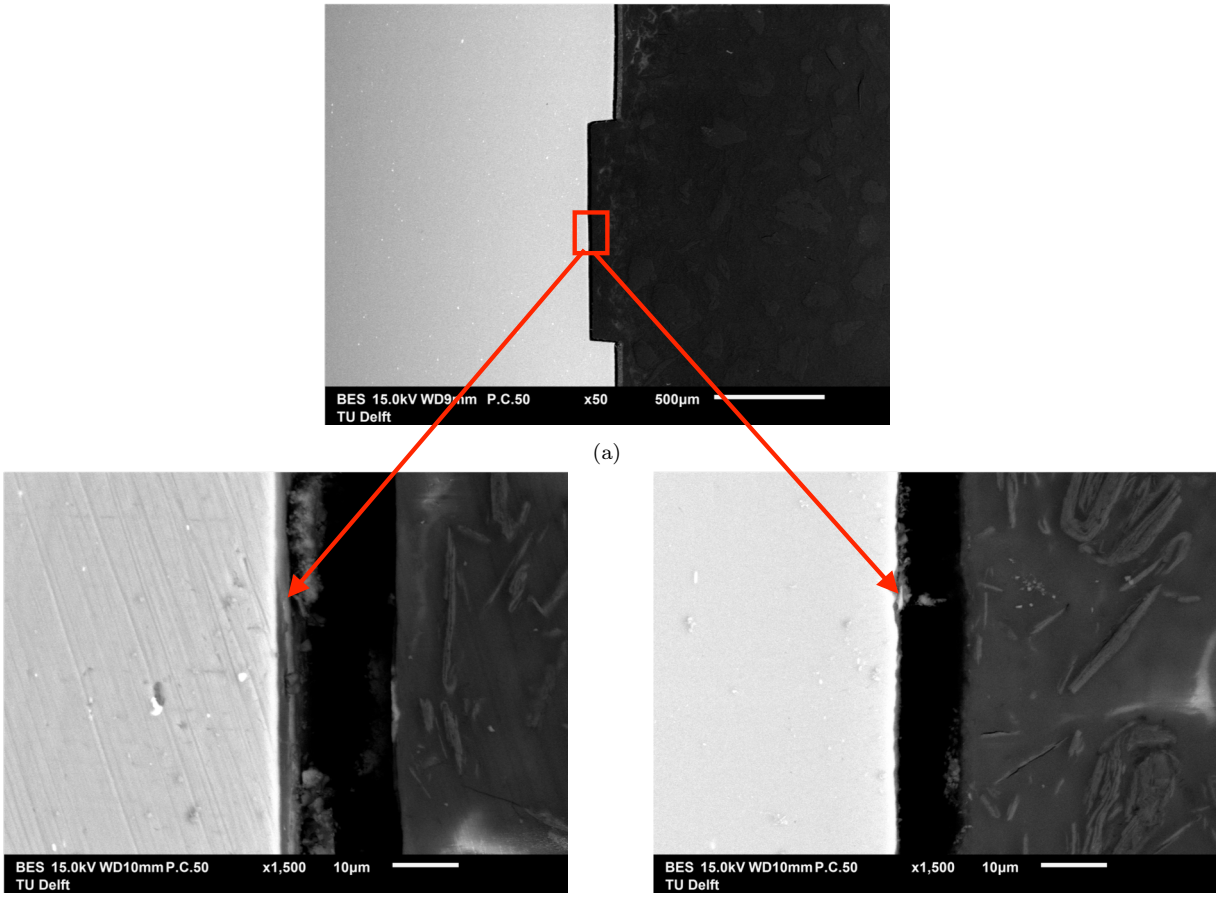


(a)

(b)

(c)

Figure 46: Cross section of the scribed area AA2198-T8 with XP420 with 1-week NSS in advance before and after the immersion in 0.1 M NaCl for 168 hours: Backscattered electron imaging of (a) Scribed area in 50X magnification; (b) Scribed area in 1500X magnification before the experiment; (c) Scribed area in 1500X magnification after the experiment

## 3.3 Discussion

In previous sections, results of three types of coatings applied on AA2024-T3 and AA2198-T8 obtained from the electrochemical experiments were displayed and analyzed, and their morphology of surface and cross section were represented to help with the further understanding. In this section, further discussion and comparison on these results is included in order to achieve the aim of objective for this project.

As shown in LPR results, the initial resistance polarization after 2 hours immersion in 0.1M NaCl of samples with $Li_2CO_3$-loaded coatings are all higher than that of samples with non-inhibiting coating which demonstrates the formation of protective layer caused by the lithium leaching from the coating loaded with $Li_2CO_3$ [52]. The XP420, to some extent, shows the better stability and corrosion protection in the long-term than model coating containing $Li_2CO_3$. This can be verified by higher values of resistance polarization and less standard deviation obtained from LPR results.

Besides, samples with 1-week NSS in advance presents higher initial resistance polarization than samples without 1-week NSS which can be further verified by EIS. This behavior indicates that the 1-week NSS performed on samples with defect enables the formation of protective layer before the electrochemical experiments. Apart from that, it was found that the resistance polarization shown in LPR and impedance modulus shown in EIS of samples with 1-week NSS keep increasing with time after further immersion which implies that the protective layer is still evolving.

When considering the EIS results without NSS, the samples of AA2024-T3 present good correlation with LPR results. The impedance modulus of AA2198-T8 is higher than that of AA2024-T3 for the first 24 hours, which implied the better inhibition performance when apply coating on the aluminium containing lithium. After the experiment, the impedance modulus of model coating containing $Li_2CO_3$ are similar for AA2024-T3 and AA2198-T8 which means the protective layer is probably locally break down. The reason to cause the higher values of impedance modulus obtained on the AA2198-T8 may due to the existence of lithium inside the AA2198-T8, thus, the lithium is possible to release from the surface of aluminum alloys so to improve the leaching process. Also, three time-constants and broadened shape of phase angle plot are observed especially in model coating containing $Li_2CO_3$ which represent the formation of three-layered protective layer. As for AA2198-T8 aluminum alloys with $Li_2CO_3$-loaded coating, the asymmetry and broadened shape of phase angle imply the formation of three-layered protective layer [53]. It is interesting to note that from the phase angle plot of model coating applied on AA2198-T8 aluminum lithium alloy, the hidden shoulder and asymmetry are also observed in the middle range of frequency.

The possible reason to explain this phenomenon is that the lithium leaching protective layer is formed after the dissolution of oxide layer.

When turn to the samples with NSS, the initial impedance modulus of AA2198-T8 are higher than that of AA2024-T3, it further proves that the AA2198-T8 has the ability to enhance the formation of protective layer. The changes in impedance modulus is not much but slightly increase in most of samples which may relate to the continuously growth in protective layer on scribed area of AA2198-T8. The same behavior in phase angle plot of AA2024-T8 is also observed in AA2198-T8 such as the hidden time-constant on the shoulder on the middle range of frequency.

As regards to the morphology observations, the surface morphology of initial layer of samples with NSS shows the typical morphology of the hydrated aluminium oxide generated on the aluminum alloy [54]. It can be characterized as the porous texture consisted randomly oriented fine flakes for both AA2024-T3 and AA2198-T8. After the further immersion in 0.1M NaCl for 168 hours, corrosion products were extensively produced which can be characterized by the clusters consisting countless round particles. In order to investigate the protective layer formed on the aluminum alloys, the morphology of cross section was obtained. Due to the resolution limitation, it is not possible to identify the three-layered feature for all samples. However, XP420 without NSS of AA2024-T3 demonstrate the clear two regions in protective layer. Besides, by comparison of thickness of samples without NSS, samples of model coating and model coating containing $Li_2CO_3$ applied on AA2198-T8 is much thicker than that of AA2024-T3 which proves the use of aluminum lithium alloys improve the formation of lithium protective layer since it may increase the concentration of lithium ion in the solution. The protective layer of XP420 for AA2024-T3 is thicker than that of AA2198-T8. Also, for samples with NSS, the changes in thickness of XP420 of AA2024-T3 displays that the thickness decreases after the experiments which is contradictory with the results obtained from LPR and EIS. The possible explanation would be the densification of protective layer. However, there is another factor which may lead to this problem. It was found that there is delamination between aluminum alloys and coating in some of samples of AA2198-T8, for examples, the sample shown in Figure 47. It can be seen that he coating is detached from the substrate which resulted in a gap. It has been demonstrated that transport pathways for leaching of Li, Ba and Mg are probably include paths that result from delamination in lithium carbonate-primer [55]. Therefore, it is possible to assume that the electrolyte may enter the delamination, resulting in the enlargement of area exposed to the electrolyte and lithium leaching in the coating inside. It is possible to cause the error in the measurement of LPR.

In order to figure out whether this assumption, equivalent circuit as shown in Figure 48

was used to fit the results from electrochemical experiments of samples of AA2198-T8 with NSS. As shown in Table 13, in this model, the values of $LPR_{measurement}$ and $LPR_{fitting}$ are measured and calculated based on the bottom area of container. $R_1$ is the solution resistance, and the first time-constant represents the resistance of the native aluminium oxide ($R_2$) and its capacitance properties ($CPE_1$). The second time-constant describes the electrochemical processes (corrosion) at the aluminium substrate in terms of the polarization resistance ($R_3$) and the double layer capacitance ($CPE_2$). It can be seen that the values of $LPR_{measurement}$ and $LPR_{fitting}$ for model coating and model coating containing $Li_2CO_3$ are not far apart. Therefore, it is possible that the area used to measure the LPR in former subsection is not the active area during the experiment, and lead to the low values of resistance polarization for samples without NSS. However, further development and research is needed to clarify this assumption by repeating the procedures using the samples with no delamination.

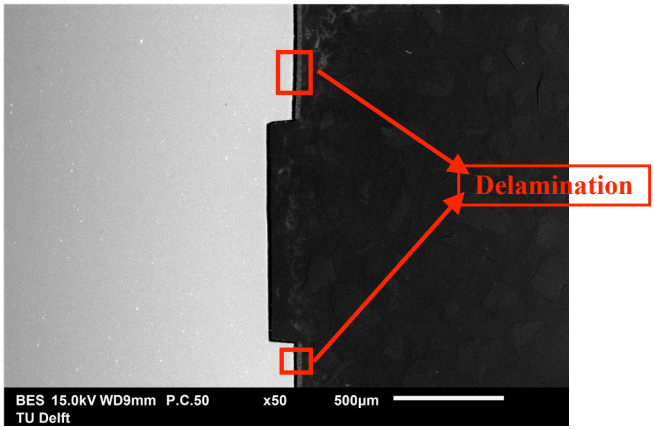


Figure 47: Delamination from Morphology of cross section of AA2198-T8 coated with XP420 with 1-week NSS

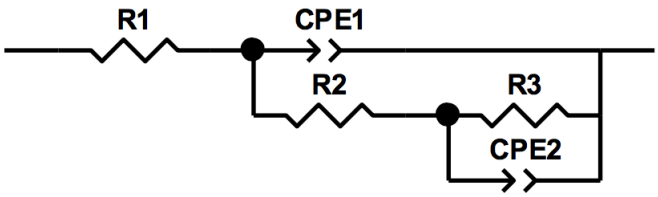


Figure 48: Equivalent electric circuits used to fit the EIS spectra

| | $LPR_{measurement}$ (Ohm.cm$^2$) | $LPR_{fitting}$ (Ohm.cm$^2$) |
|---|---|---|
| Model coating (12h) | 796,364 | 824,910 |
| Model coating containing $Li_2CO_3$ (12h) | 853,147 | 736,980 |
| XP420 (12h) | 603,947 | 461.010 |

Table 13: Comparison of LPR results from the calculation of measurements and fitting

# 4 Conclusion

Corrosion inhibition properties of lithium leaching coating applied on AA2024-T3 and AA2198-T8 aluminum alloys (contain Li in the composition) are investigated in this thesis. The lithium leaching coating samples are divided into two types which are the model coating containing $Li_2CO_3$ and Proprietary $Li_2CO_3$-loaded coating of XP420. The model coating which is the non-inhibiting coating is also applied on the aluminum alloys as a reference. Electrochemical measurements including Open circuit potential (OCP), linear polarization resistance (LPR) and electrochemical impedance spectroscopy (EIS) were utilized to study the corrosion inhibition performance and mechanism of formation of protective layer. Two groups of samples are used during the experiment. One only has the normal cross scribe without any pre-treatment so the formation of protective layer can be expected after the test, the other group is applied with NSS for one week which can be regarded as the accelaration test. The groups with NSS in advance would help with the investigation of corrosion inhibition inhibition performance of the protective layer. Scanning electron spectroscopy (SEM) was used to study the morphology of surface and cross section in order to further discuss the details of the protective layer formed.

The results show that, although different aluminum alloys have different physical metallurgical and electrochemical activities, the protective layer can be formed by lithium leaching coating in the defect area under 0.1M 5ml NaCl, and shows the ability to prevent corrosion more effectively than non-inhibiting coating. Besides, through surface morphology, the typical porous texture consisted of flake-like features randomly distributed along the aluminum surface was observed.

It is difficult to compare the corrosion inhibition performance between model coating containing $Li_3CO_3$ and XP420 on AA2024-T3 aluminum alloys, but XP420 shows better stability and corrosion protection on AA2198-T8 aluminum alloys than model coating containing $Li_3CO_3$. Also, by comparison the results from electrochemical experiment, it is clear to see the hidden time-constant by observing asymmetric shape and a shoulder between the middle frequency on the bode plots of phase angle. What is more, the calculation of thickness for the protective layer through the scanning electron images of cross section for samples with $Li_3CO_3$-loaded coatings illustrate that the formation of protective layer on the AA2198-T8 is thicker than that of AA2024-T3 which means that the Al-Li alloys further contributes to the formation of protective layer.

# 5 Future work

Based on the results of this thesis, further development could be conducted from the following several aspects.

1. The cross section of protective layer formed on AA2198-T8 is needed to investigated whether the morphology of protective layer is the same as observed on AA2024-T8.
2. In this these, 0.1M 5ml NaCl was used as electrolyte during the electrochemical experiment. In the further research, it is possible to increase the concentration of the electrolyte to monitor the performance of inhibitor under the extreme environment.
3. The delamination was observed during the experiment, therefore, it would be better to repeat the same procedure to check results obtained and see whether the delamination would affect the results significantly.
4. With aspect to the macro level lithium leaching coating, it is expected to use modelling to simulate the leaching mechanism of lithium coating and the service life under different environment conditions.

# 6 Acknowledgement

I would like to express my gratitude to all those who helped me during the period of this graduation project.

Firstly, many thanks to my supervisor Dr. Yaiza Gonzalez-Garcia and daily supervisor Dr. Emina Michailidou, who gave me the precious opportunity to take this project and walked me through all the stages of the project. Without their consistent and illuminating instruction, I cannot finish my thesis so well.

Secondly, I would like to express my heartfelt gratitude to the members of corrosion group who gave me a lot useful advice and inspiring chat during the time in the lab. Many thanks to the technician Agnieszka who helps me all the time when I had difficulties during the experiment.

Then, my thanks would go to my beloved family, my grandmother Mei Chen, my father Xiaobing Chen, my mother Aiyan Wu, my brothers Qian Chen and Yun Chen for their loving considerations and great confidence in me all through whole thesis. Special thanks to my grandfather Tinggui Chen who always gave me unconditional support to do whatever I wanted to do, I miss you a lot. May you rest in peace. I also owe my sincere gratitude to my friends Dan Chen, Yizhou Chen, Jiani Tian, Chenxue Dong, Mengya Wei, Zhen Sun, Menxin Yu, Jingchun Xiang, Shiyu Feng, Xiang Li, Fangyi Qin and my fellow classmates who gave me their help and time in listening to me and helping me work out my problems.

Last, I would like to mention that now China is going through an invisible disaster - the outbreak of novel coronavirus, my family, friends and the Chinese all over the world are all working together to help our country to survive from it. I am really grateful for the front-line medical staff and workers from every industry who are fighting this battle. May you return safely. Sincere thanks to all you once again.

# References


[1] Tolga Dursun and Costas Soutis. Recent developments in advanced aircraft aluminium alloys. *Materials  Design (1980-2015)*, 56:862–871, 2014.

[2] Nick Birbilis and Bruce RW Hinton. *Crystalline Alloys: Aluminum*, pages 85–694. CRC pressr, 2013.

[3] Norio Sato. An overview on the passivity of metals. *Corrosion science*, 31:1–19, 1990.

[4] Edward McCafferty. *Passivity*, pages 209–262. Springer, New York, NY,, 2010.

[5] Szklarska-Smialowska Z. Mechanism of pit nucleation by electrical breakdown of the passive film. *Corrosion Science*, 44(5):1143–1149, 2002.

[6] Marcel Pourbaix. Atlas of electrochemical equilibria in aqueous solution. *NACE*, 307, 1974.

[7] C. S. Jawalkar and Suman Kant. A review on use of aluminium alloys in aircraft components. *i-Manager's Journal on Material Science*, 3(3):33–38, 2015.

[8] ed. Benavides, Samuel. Corrosion in the aerospace industry. *Corrosion control in the aerospace industry*, pages 1–14, 2009.

[9] Daniel Raymer. *Aircraft design: a conceptual approach*. American Institute of Aeronautics and Astronautics, Inc., 2018.

[10] Rishi Kant. Corrosion monitoring and control in aircraft: A review. *Sensors for Automotive and Aerospace Applications*, pages 39–53, 2019.

[11] Mol J.M.C. Visser P., Terryn H. Aerospace coatings. *Active Protective Coatings*, 233, 2016.

[12] Sviatlana V. Lamaka Snihirova, Darya and M. Fatima Montemor. Smart composite coatings for corrosion protection of aluminium alloys in aerospace applications. *Smart Composite Coatings and Membranes*, pages 85–121, 2016.

[13] R. L. Twite and Gordon P. Bierwagen. Review of alternatives to chromate for corrosion protection of aluminum aerospace alloys. *Progress in organic coatings*, 33(2):91–100, 2014.

[14] Per Aggerholm Sørensen. Anticorrosive coatings: a review. *Journal of Coatings Technology and Research*, 6(2):135–176, 2009.

[15] Kevin Douglas Ralston. Corrosion inhibition of aluminum alloy 2024-t3 by aqueous vanadium species. *Journal of The Electrochemical Society*, 155(7):350–359, 2008.

[16] Kevin Douglas Ralston. Corrosion protection of aluminum alloy 2024-t3 by vanadate conversion coatings. *Corrosion*, 60(3):284–296, 2008.

[17] Mariano Iannuzzi and Gerald S. Frankel. Mechanisms of corrosion inhibition of aa2024-t3 by vanadates. *Corrosion Science*, 49(5):2371–2391, 2007.

[18] Gerald S. Frankel and Richard L. Inhibition of al alloy corrosion by chromates. *Interface-Electrochemical Society*, 10(4):34–39, 2001.

[19] I. M. Zin. The mode of action of chromate inhibitor in epoxy primer on galvanized steel. *Progress in Organic Coatings*, 33(3-4):203–210, 1998.

[20] Gerald Frankel Zhao, Jun and Richard L. Corrosion protection of untreated aaptm[U+2010]2024ptm[U+2010]t3 in chloride solution by a chromate conversion coating monitored with raman spectroscopy. *Journal of the Electrochemical Society*, 145(7):2258–2264, 1998.

[21] Belinda L. Hurley and Richard L. McCreery. Raman spectroscopy of monolayers formed from chromate corrosion inhibitor on copper surfaces. *Journal of The Electrochemical Society*, 49(5):B367–B373, 2003.

[22] H. Luo. Electrochemical behavior of 2205 duplex stainless steel in nacl solution with different chromate contents. *Journal of materials engineering and performance*, 21(7):34–39, 2012.

[23] S. B. Lyon Baghni, I. M. and Baofeng Ding. The effect of strontium and chromate ions on the inhibition of zinc. *Surface and Coatings Technology*, 185(2-3):194–198, 2004.

[24] S. J. Ketchum and S. R. Brown. Chromate conversion coatings of aluminum alloys. 74:37–41, 1975.

[25] F. H. Scholes. Chromate leaching from inhibited primers: Part i. characterisation of leaching. *Progress in Organic Coatings*, 56(1):23–32, 2006.

[26] F. H. Scholes. Chromate leaching from inhibited primers: Part i. characterisation of leaching. *Progress in organic coatings*, 56(1):23–32, 2006.

[27] Oumaïma Gharbi. Chromate replacement: what does the future hold? *npj Materials Degradation*, 2(1):1–8, 2018.

[28] Regulation (ec) no 1907/2006 of the european parliament and of the council of 18 december 2006 concerning the registration, evaluation, authorisation and restriction of chemicals (reach), establishing a european chemicals agency, amending directive 199, 2006.

[29] Amol Gokhale Prasad, N. Eswara and eds R. J. H. Wanhill. *Aluminum-lithium alloys: processing, properties, and applications*, pages 503–505. Butterworth-Heinemann, 2013.

[30] R. G. Buchheit. Anodic dissolution-based mechanism for the rapid cracking, pre-exposure phenomenon demonstrated by aluminum-lithium-copper alloys. *Corrosion*, 51:417–428, 1995.

[31] M. W. Kendig and R. G. Buchheit. Corrosion inhibition of aluminum and aluminum alloys by soluble chromates, chromate coatings, and chromate-free coatings. *Corrosion*, 59(5):379–400, 2003.

[32] Peter Visser. Lithium salts as leachable corrosion inhibitors and potential replacement for hexavalent chromium in organic coatings for the protection of aluminum alloys. *Journal of Coatings Technology and Research*, 13(4):557–566, 2016.

[33] Peter Visser. The corrosion protection of aa2024-t3 aluminium alloy by leaching of lithium-containing salts from organic coatings. *Faraday discussions*, 180:511–526, 2015.

[34] Peter Visser. Study of the formation of a protective layer in a defect from lithium-leaching organic coatings. *Progress in Organic Coatings*, 99:80–90, 2016.

[35] R. T. Foley and T. H. Nguyen. The chemical nature of aluminum corrosion v. energy transfer in aluminum dissolution. *Journal of the Electrochemical Society*, 129(3):464–467, 1982.

[36] C. Luo. Observations of intergranular corrosion in aa2024-t351: The influence of grain stored energy. *Corrosion Science*, 61:35–44, 2012.

[37] X. Zhou. Grainptm[U+2010]stored energy and the propagation of intergranular corrosion in aa2xxx aluminium alloys. *Surface and Interface analysis*, 45(10):1543–1547, 2013.

[38] L. B. Khokhlatova Kolobnev, N. I. and I. N. Fridlyander. Aging of al-li alloys having composite particles of hardening phases. *Materials Forum*, 28, 2004.

[39] Roberto J. Rioja and John Liu. The evolution of al-li base products for aerospace and space applications. *Metallurgical and Materials Transactions A*, 43(9):3325–3337, 2012.

[40] Anand. Durairajan. Development of a new electrodeposition process for plating of znptm[U+2010]niptm[U+2010]x (x= cd, p) alloys: I. corrosion characteristics of znptm[U+2010]niptm[U+2010]cd ternary alloys. *Journal of The Electrochemical Society*, 147(5):1781–1786, 2000.

[41] Branko N. Popov. *Chapter 5 - Basics of Corrosion Measurements, Corrosion Engineering*, pages 181–237. Elsevier, 2015.

[42] Allen J Bard, Larry R Faulkner, Johna Leddy, and Cynthia G Zoski. *Electrochemical methods: fundamentals and applications*, volume 2. wiley New York, 1980.

[43] D Needham. Reverse engineering of the low temperature-sensitive liposome (ltsl) for treating cancer. In *Biomaterials for Cancer Therapeutics*, pages 270–353e. Elsevier, 2013.

[44] Milton Stern and Al L Geary. Electrochemical polarization i. a theoretical analysis of the shape of polarization curves. *Journal of the electrochemical society*, 104(1):56–63, 1957.

[45] Nestor Perez. *Electrochemistry and corrosion science*, volume 412, pages 101–148. Boston: Kluwer Academic Publishers, 2004.

[46] I. Epelboin. The dissolution and passivation of fe and fecr alloys in acidified sulphate medium: Influences of ph and cr content. *Corrosion Science*, 19(5):1105–1112, 1979.

[47] Florian Mansfeld. Recording and analysis of ac impedance data for corrosion studies. *Corrosion*, 37(5):301–307, 1981.

[48] Optieis: A multisine implementation application note rev. 1.0. 1990-2011.

[49] Vadim F Lvovich. *Impedance spectroscopy: applications to electrochemical and dielectric phenomena*, page 4. John Wiley & Sons, 2012.

[50] David Brandon and Wayne D. Kaplan. *Microstructural characterization of materials*. John Wiley Sons, 2013.

[51] G Love Potts, P. J. "VD Scott and SJB Reed. *Quantitative Electron-Probe Microanalysis*, volume 59.397. London and New York (Ellis Horwood), 1995.

[52] Peter Visser. Mechanism of passive layer formation on aa2024-t3 from alkaline lithium carbonate solutions in the presence of sodium chloride. *Journal of The Electrochemical Society*, 165(2):60–70, 2018.

[53] Peter Visser. Electrochemical evaluation of corrosion inhibiting layers formed in a defect from lithium-leaching organic coatings. *Journal of The Electrochemical Society*, 164(7):C396–C406, 2017.

[54] Abraham Glasner Frenkel, Moshe and Sara Sarig. Crystal modification of freshly precipitated aluminum hydroxide by lithium ion intercalation. *The Journal of Physical Chemistry*, 84(5):507–510, 1980.

[55] Jamie S. Laird. Li leaching from lithium carbonate-primer: An emerging perspective of transport pathway development. *Progress in Organic Coatings*, 134:103–118, 2019.